UNIVERSITEIT VAN PRETORIA
UNIVERSITY OF PRETORIA
YUNIBESITHI YA PRETORIA

SCHOOL OF ENGINEERING

DEPARTMENT OF MECHANICAL AND AERONAUTICAL ENGINEERING

Development of an improved design correlation for local heat transfer coefficients at the inlet regions of annular flow passages

by

Berno W Kohlmeyer

Submitted in partial fulfilment of the requirements for the degree of

Master of Engineering

In the Department of Mechanical and Aeronautical Engineering in the Faculty of Engineering, Built Environment and Information Technology

UNIVERSITY OF PRETORIA

February 2017

Supervisors: Prof J Dirker and Prof JP Meyer

Abstract

Author:	Berno Werner Kohlmeyer
Student number:	11057107
Supervisors:	Prof J Dirker and Prof JP Meyer
Department:	Mechanical and Aeronautical Engineering
Degree:	Master of Engineering (Mechanical Engineering)

Several applications, including those in the energy sector that require high thermal efficiency, such as those in the solar energy industry, require a careful thermal analysis of heat exchange components. In this regard, thermal resistance is a major cause of exergy destruction and must be minimised as much as possible, but also adequately designed.

In the past, a number of correlations have been developed to predict heat transfer coefficients in compact heat exchangers. The designers of such heat exchangers often exploit the development of thermal boundary layers to achieve higher overall efficiency due to increases in local heat transfer coefficients. However, most of the correlations that have been developed for heat exchangers neglect the specific effect of the thermal boundary layer development in the inlet region, and instead only offer effective average heat transfer coefficients, which most users assume to be constant throughout the heat exchanger. This is often an over-simplification and leads to over-designed heat exchangers.

In this study, focus is placed on annular flow passages with uniform heating on the inner wall. This geometry has many applications. This study aims to collect experimental heat transfer data for water at various flow rates and inlet geometries, to process the data and determine local and overall heat transfer coefficients, and to develop an improved local heat transfer coefficient correlation.

Experimental tests were performed on a horizontal concentric tube-in-tube heat exchanger with a length of 1.05 m and a diameter ratio of 0.648. The surface of the inner tube was treated with thermochromic liquid crystals (TLCs), which allowed for high-resolution temperature mapping of the heated surface when combined with an automated camera position system in order to determine local heat transfer coefficients. Conventional in-line and out-of-line annular inlet configurations were evaluated for Reynolds numbers from 2 000 to 7 500, as well as the transition from laminar to turbulent flow for a single in-line inlet configuration.

It was found that the local heat transfer coefficients were significantly higher at the inlets, and decreased as the boundary layers developed. With the high resolution of the results, the local heat transfer coefficients were investigated in detail. Local maximum and minimum heat transfer coefficients were identified where the thermal boundary layers merged for high turbulent flow cases.

The annular inlet geometries only influenced the heat transfer for Reynolds numbers larger than 4 000, for which larger inlets are favoured. Out-of-line inlet geometries are not favoured for heat transfer. A new heat transfer correlation was developed from the experimental data, based on an existing heat transfer correlation for turbulent flow in an annular flow passage, considering the boundary layer development. The new correlation estimated the area-weighted heat transfer coefficients within 10% of the experimental data and closely followed trends for local heat transfer coefficients.

Keywords: Liquid crystal thermography, thermodynamically and hydrodynamically developing flow, local wall temperatures, local heat transfer coefficients, annulus, heat exchanger, turbulent flow, transitional flow regime

Publications resulting from this investigation:

A journal article manuscript based on the study has been submitted to International Journal of Heat and Mass Transfer (Submission number: HMT_2017_433)

BW Kohlmeyer, J Dirker, JP Meyer. *“Local heat transfer coefficients at the inlet of an annular flow passage”*

Acknowledgements

I want to thank God for giving me the opportunity to carry out a lifelong dream in implementing and developing my talents. Thank you to all the people around me who helped me to complete this project.

I also want to thank my parents for supporting me daily and remaining interested in my project. I am grateful for my mother's continually asking how things are going and offering support during test times. I would like to thank my father for all his help in building the experimental facility. I thank him for his patience, advice and knowledge to complete this research project.

Thank you to Prof J Dirker for all the motivation, advice, support and knowledge he has given me to complete this project. I am truly fortunate to have had such an accomplished supervisor for my master's degree project. Thank you for all the time you spent motivating me.

I also want to acknowledge my fellow master's degree students for always offering support and encouragement. Thank you, Martin, for your kind assistance in building and testing. I would like to thank Louis for his positive encouragement and Francois for his positive attitude in all situations.

I am grateful for the funding I received from the National Research Foundation (NRF) Renewable and Sustainable Energy Scholarships and the University of Pretoria.

Thank you, Japie van der Westhuizen, for developing a methodology from which the local heat transfer coefficients could be determined for an annular flow passage by means of liquid crystal thermography.

To the members of House4Hack, especially Quentin Harley, thank you for offering support and advice in implementing electronic controllers.

I would like to thank Peet Kruger for all his advice and help in machining all the complex components for my master's degree project.

I am also grateful for Prof Schalk Els's words of encouragement during the difficult times and his vast knowledge in machining and problem-solving.

Contents

List of figures

List of tables

Nomenclature

Symbol	Property	Units
a	Diameter ratio	-
B	Intensity of colour blue	-
c	Constant	-
C_p	Heat capacity (specific heat)	J/kgK
D	Diameter	m
F	Annular ration constant	
f	Friction factor	-
G	Intensity of colour green	-
Gr^*	Modified Grashof number	-
h	Heat transfer coefficient	W/m^2K
H	Hue value	-
I	Current	A
k	Thermal conductivity	W/mk
L	Length	m
m	Gradient	-
$\dot{m}$	Mass flux	kg/s
Nu	Nusselt number	-
Pr	Prandtl number	-
Pw^*	Modified tube wall parameter	-
Q	Heat transferred	J
$\dot{Q}$	Heat transfer rate	W
$\dot{q}$	Heat flux	W/m^2
q''	Circumferential average heat flux	W/m
p	Perimeter	m
R	Intensity of colour red	-
R	Thermal resistance	K/W
r	Radius	m
Re	Reynolds number	-
Re^*	Modified Reynolds number	-
T	Temperature	℃
t	Tube wall thickness	m
U	Velocity	m/s
V	Voltage	V

x	Axial displacement	m

Subscripts

Symbol	Property
1	Outer diameter of inner tube
2	Inner diameter of outer tube
3	Inner diameter of inlet/outlet tube
a	Annular
amb	Ambient property
adh	Protective adhesive layer
avg	Area-weighted average
b	Bulk fluid property
bin	Inlet bulk fluid property
$bout$	Outlet bulk fluid property
c	Cross-sectional
cal	Calibrated
$cond$	Conduction
$conv$	Convection
cyl	Cylinder property
$elec$	Electrical
f	Fully developed
h	Hydraulic
hy	Hydrodynamic property
i	Inner tube
l	Dependence of local axial (length) position
o	Annulus
ins	Insulation
pg	Plexiglass
pg, ins	Plexiglass and insulation
s	Surface property
TLC	Thermochromic liquid crystals
tot	Total
t	Thermal property
$uncal$	Uncalibrated
w	Wall property
ws	Wetted surface
y, z	Constants

Greek symbols

Symbol	Property	Units
α	Thermal diffusivity	m^2/s
β	Volumetric expansion coefficient	$1/K$
γ	Correlation constant	-
δ	Uncertainty	-
μ	Dynamic viscosity	kg/ms
ρ	Density	kg/m^3
υ	Kinematic viscosity	m^2/s

1. Introduction

1.1 Background

Heat transfer is an important energy transfer mechanism that is found in a wide spectrum of applications, ranging from biological systems to human-engineered power conversion systems. In power conversion systems specifically, efficient thermal energy transfer is desired in a wide range of components, such as heat exchangers, energy collectors and energy radiators. These components act as thermal interfaces within a system between different substances or between a system and its surroundings, where it might receive or expel energy.

Technological advances in power generation systems that make use of renewable or clean energy sources are critically important for the long-term sustainable development of industrialised societies. Such advances depend on improvements in several subsystems, including those in thermal systems that rely on, among other things, heat transfer equipment such as heat exchangers.

For instance, in solar-driven thermodynamic systems, which form an important part of the clean energy sector, heat transfer is required during solar energy collection via radiation, during internal energy transfer to, from or between working fluids, during the charging and discharging of thermal storage elements, and during heat rejection to the environment. One of the causes of inefficiencies encountered during such processes is that of thermal resistance, which reduces the rate of heat transfer. This leads to exergy destruction. For that reason, thermal design engineers are constantly searching for methods to reduce thermal resistance, so that heat transfer components may become more compact and operate at lower thermal temperature difference potentials.

Convection heat transfer, which is the dominant heat transfer mode in heat exchangers, comprises heat transfer by either random molecular motion or bulk fluid motion. Such heat transfer is often expressed with a heat transfer coefficient, which relates the surface area and the temperature difference between the surface and the fluid in motion with the heat transfer rate. The ability to transfer heat via convection is normally characterised in terms of the Nusselt number, which is a dimensionless, convective heat transfer coefficient that describes the ability to transfer heat between a working fluid and a heated or cooled surface. These heat transfer coefficients are of interest to thermal designers and are continually being examined by researchers.

The thermal resistance (inverse to the heat transfer coefficient) in heat transfer equipment is increased by the development of the thermal and velocity boundary layers. Boundary layer development is graphically depicted in Figure 1-1-1 for a fluid flowing through a tube. Convective boundary layers form when the fluid with properties T_∞, u_∞ flows over a surface and is halted through direct contact with the surface. This reduces the velocity of the fluid particles close to the surface and forms a velocity boundary layer that extends away from the surface, resulting in a new velocity profile.

This reduction in fluid velocity reduces the heat transferred by convection, resulting in heat transfer that is dominated by conduction. Conduction is a heat transfer mode in which thermal energy is transferred by the interaction between particles. The rate of heat transfer by conduction is less than that of convection for a system that comprises a fluid and a surface. Thus, a subsequent thermal boundary layer and a temperature profile form in which the wall temperature T_s is higher than T_∞ (see Figure 1-1-1).

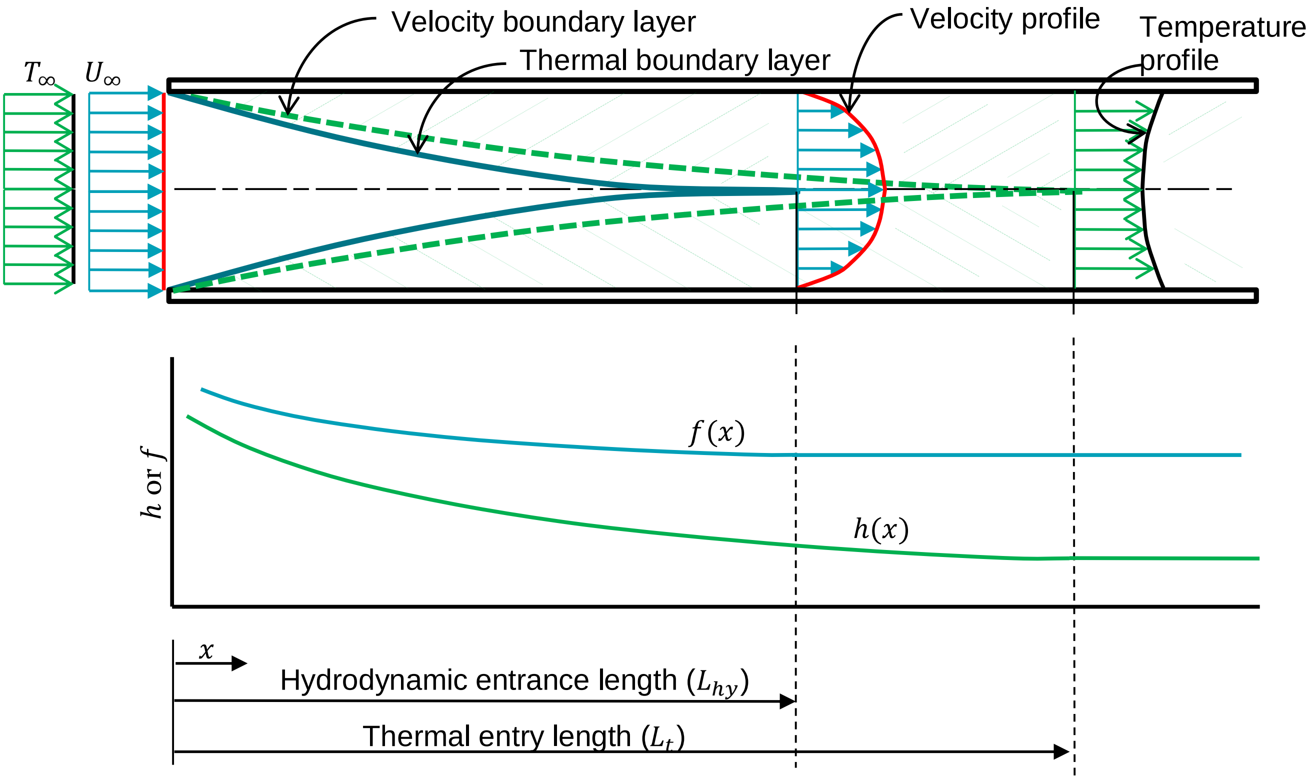

Figure 1-1-1: Boundary layer development inside a tube as seen from side-section view

If not disturbed, the velocity and thermal boundary layers become thicker as the fluid passes through a flow passage. Once the boundary layers of the opposite flow passage walls merge, a fully developed flow profile is achieved. The hydrodynamic entry length L_{hy} and thermal entry lengths L_t are the distances from the tube inlet to where the respective velocity boundary layers and thermal boundary layers merge. Once the flow is fully developed hydrodynamically and thermally, the flow is fully developed.

Designers of compact heat exchangers make use of this phenomenon by selecting flow passage geometries and lengths so that the majority of the heat transfer surfaces are associated with developing boundary layers. As depicted in Figure 1-1-1, this is where the heat transfer and friction factors decrease from a maximum to a constant value during boundary layer development for improved heat transfer coefficients and efficiencies.

Due to the simplicity of their design and ability to withstand high pressures, concentric tube heat exchangers are found in many heat transfer applications. These heat exchangers consist of two tubes of different diameters placed inside one another to form an annulus. Often, hot and cold fluids flow in the inner tube and annular flow passages in either a concurrent or counter-current configuration. Due to its wide use, several researchers have studied the heat transfer and pressure drop characteristics of annular flow passages.

Based on such research, several heat transfer coefficient and friction factor correlations have been developed. These offer the designer the ability to estimate the effective average heat transfer coefficient and friction factor along the entire length of the heat exchanger. These correlations differ in estimating the magnitude of heat transfer for different flow conditions, which may be attributed to the accuracy of the experimental setup and the spectrum of applicability. Thermal designers utilise these correlations to size the heat transfer equipment for any given application. These correlations were formulated to incorporate all major physical and thermodynamic factors that were found to influence the heat transfer. Previous research reveals that the dominating factor in heat transfer is the flow state of the fluid, which is expressed by the Reynolds number. The flow state may be categorised as being laminar, transitional or turbulent, where turbulent flow yields the highest heat transfer ability. For this reason, many correlations are devoted specifically for turbulent flow regime conditions. However, due to design and operational limitations, heat exchangers are also operated in the laminar flow regime and even in the transitional flow regime.

Only a limited number of correlations (whether for turbulent or laminar flow regimes) has been published that describes the heat transfer ability in the entrance region of a concentric tube heat exchanger. In such conditions, the flow is not fully developed thermally or hydrodynamically. The small number of correlations could be due to designers' assumption that the conservative nature of conventional correlations is suitable to account for heat transfer in inlet regions or due to the difficulties arising when attempting to accurately measure the heat transfer ability in the developing region of fluid flow without influencing heat transfer and fluid flow.

Irrespective of the difficulty of an experimental setup, wall and bulk fluid temperature measurements are needed to measure the heat transfer coefficients. These temperature measurements are often conventionally captured by thermocouples. However, thermocouples are notorious for influencing heat transfer behaviour and altering fluid flow, especially since it is an intrusive measuring method. Hence, other techniques for measuring temperature that have a smaller influence on the flow characteristics have been developed and implemented. Alternative temperature measurement options include thermistors, pyrometers and thermographic or thermal cameras. The majority of these options allow for accurate measurements, but may be unsuitable for a given application.

Liquid crystal thermography is a thermographic technique for measuring temperature that uses thermochromic liquid crystals (TLCs). These are optically active crystals that react to changes in temperature by changing their colour. These crystals can be applied to a surface or added to the fluid and do not interfere with the fluid flow field. Van der Westhuizen et al. (2014) have shown that liquid crystal thermography is a viable method for capturing high-resolution temperature fields on internal wetted heat transfer surfaces to obtain local heat transfer coefficients. Even though this method has been shown to be suitable for wetted systems, it has not yet been applied to a wide range of heat transfer and fluid flow cases and there is an opportunity to utilise this method in addressing some of the shortcomings of the current state of annular flow literature.

1.2 Problem statement

Even though some correlations exist for heat transfer in annular flow passages, the heat transfer in the inlet region of a concentric tube heat exchanger has not been investigated adequately and little evidence (experimental data) has been found to specifically validate such correlations when the flow is developing thermally and hydrodynamically. There is a specific gap in knowledge in the Reynolds number range of 2 000 to 10 000 and little is known of the local heat transfer coefficient in the transitional flow regime. The influence of on-line and off-line inlet geometries of different sizes has not been reported in current literature.

1.3 Objective

The following objectives formed part of this study:

- Develop an experimental test section from which the local heat flux, local (axial) bulk fluid temperatures and local wall temperatures could be determined for an annular flow passage with different inlet geometries using liquid crystal thermography.
- Conduct steady-state experiments and capture the local heat flux, local (axial) bulk fluid temperatures and local wall temperatures.
- Analyse the data to determine the local and overall heat transfer coefficients.
- Compare the experimentally obtained heat transfer coefficients with existing correlations.

- Develop an improved empirical correlation for the low turbulent flow regime with a Reynolds number range from 2 000 to 7 500 with water as the working fluid.
- Investigate the influence of on-axis and off-axis inlet geometries of different sizes.
- Investigate the local heat transfer coefficients for the transition from laminar to turbulent flow.

1.4 Delineation and limitations

- Water will be considered as the working fluid due to its abundant use in industry and the limitations of the experimental laboratory and facilities used in this investigation.
- Tests will be conducted in the low turbulent flow state with Reynolds numbers between 2 000 to 7 500 to address the shortcoming in literature. However, the transitional flow regime will also be considered.

1.5 Significance of the study

The significance of this study lies in gathering experimental data to describe the local heat transfer coefficients in the inlet region of a concentric tube heat exchanger in the low turbulent flow regime and, to some extent, in the transitional flow regime. This still lacks in the literature to some extent. The experimentally determined local heat transfer coefficients produced by this study enable the improvement of existing heat transfer correlations and tailor them to low turbulent flow regimes. This new correlation may be used to optimise the design of short heat exchangers for many applications, including solar-driven power cycles. One of the major funders of this research is the solar industry. This research and development will aid solar thermal technologies in becoming a more viable energy source by supporting the drive of human development towards utilising sustainable energy.

1.6 Chapter overview

Chapter 2 gives a brief literature overview of topics relevant to this investigation. This includes a short overview of the fundamentals of relevant heat transfer theory of concentric annuli, existing correlations and fundamentals of TLC and past studies that implemented TLC.

Chapter 3 contains descriptions of the experimental facility, test section and the experimental methodology that was followed. This includes the custom-built, automated image recognisance system that is used to obtain the high-resolution temperature maps of the heat transfer surface.

Chapter 4 supplies details on the analysis and data reduction method used. This includes, among others, the extraction of temperatures from the TLC surfaces. The calculation of the heat transfer rate, energy balance, and the local and overall heat transfer coefficients are discussed.

Chapter 5 presents the experimental results and contains discussions of the test cases, local and overall heat transfer coefficients, compassion with existing correlations, and the development of a new correlation for the low turbulent flow state. The transitional flow regime range is also presented here.

Chapter 6 offers the summary, recommendations and conclusion of this investigation.

Several appendices are found at the end of this dissertation. These contain topic-specific details relating to sections of this investigation that might offer the reader additional insight and/or information if needed.

2. Literature study

2.1 Introduction

This chapter gives an overview of relevant topics that are important to this investigation. It is structured to incorporate the following main aspects:

- Definitions related to concentric annular flow passages
- Definitions related to the heat transfer in flow passages
- Overall and local heat transfer for circular tubes
- Local and overall heat transfer investigations for concentric flow passages
- Effect of different inlet configurations for the flow passage
- Liquid crystal thermography as an experimental method

2.2 Definitions related to annular flow passages

Heat exchangers are used to exchange energy between two fluids of different temperatures without mixing the fluids and are implemented in a wide range of applications. There are a vast number of heat exchanger types, such as the shell-in-tube, concentric tube and plate heat exchangers. The concentric tube heat exchanger is the simplest type of heat exchanger. It consists of two approximately concentric tubes (the inner tube and annulus) of different diameters placed inside one another (see Figure 2-1). Here, D_1 represents the outer diameter of the inner tube, D_2 represents the inner diameter of the outer tube and L the length of the flow passage. Normally, fluids flow in a counter-current direction (as shown).

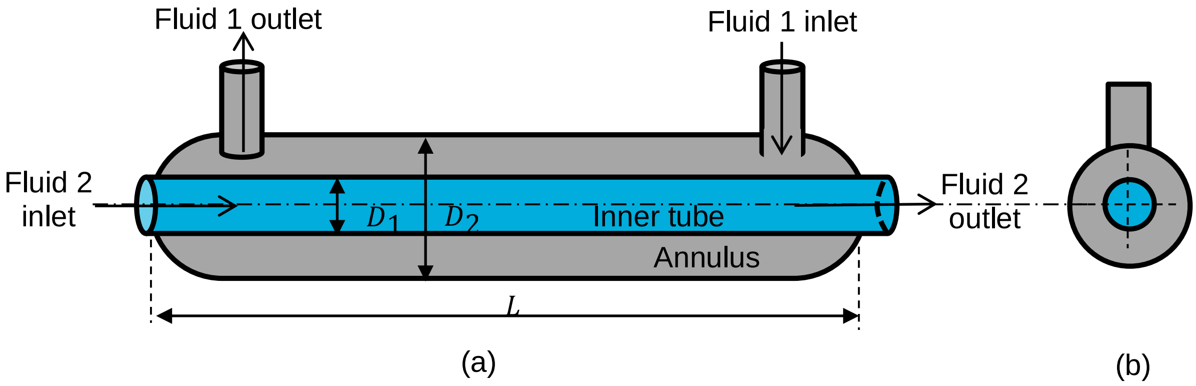

Figure 2-1: (a) Principle section view; and (b) section view of the concentric annular flow passage of a tube-in-tube heat exchanger

A heat transfer surface or, in this case, an annular heat exchanger can have different thermal boundary conditions, namely uniform wall temperature cases, non-uniform wall temperature and/or non-uniform heat flux, co-current or counter-current flow cases, and uniform heat flux cases. For uniform wall temperature cases, the fluid in the inner tube or annulus is heated or cooled when, for instance, the other fluid is subjected to isothermal condensation or boiling, or when the other fluid has a very high mass flow rate so that there is only a small temperature difference between its inlet and outlet states. In the non-uniform wall temperature and/or heat flux co-current and counter-current cases, fluids of different temperatures flow in the annular passage and inner tube in co-current or counter-current directions (see Figure 2-1). For uniform heat flux cases (often used for experimentation purposes), the heat transfer rate per unit length is well controlled, in which either the inner tube or the outer tube is uniformly heated by, for instance, an electric heating element. The uniform heat flux case may approximately also exist when there is a constant temperature difference (locally) between the inner and annular fluids for fully developed flow in a counter-flow configuration and when the value of the mass flux multiplied by the specific heat of the two flow streams is equal.

Figure 2-2 depicts generic temperature profile types of the fluids along the length of a heat exchanger for some of the abovementioned cases in which the arrows indicate the direction of fluid flow. Figure 2-2 (a) represents possible cases (heated and cooled) with a uniform wall temperature. Figure 2-2 (b and c) represent possible non-uniform wall temperature and/or non-uniform heat flux cases (co-current and counter-current respectively) and Figure 2-2 (d) represents a uniform heat flux case with active surface heating, which results in a linear increase in the bulk fluid temperature.

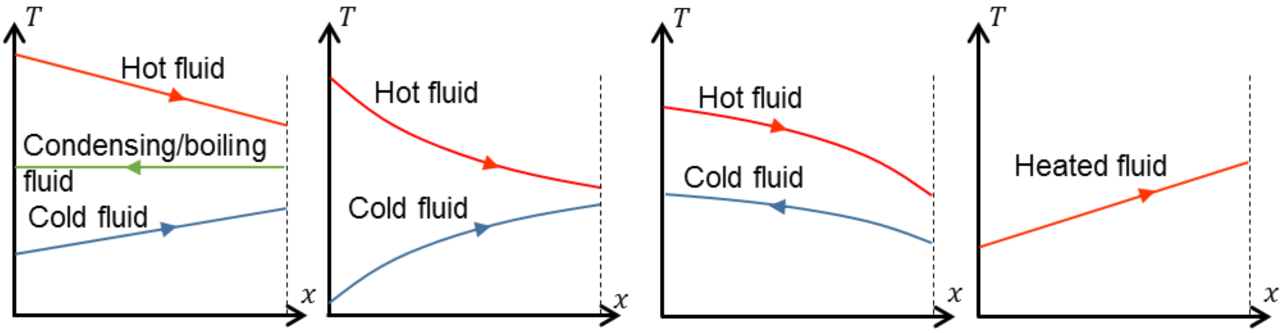

Figure 2-2: Temperature changes of fluids along the lengths of a heat exchanger for different thermal boundary conditions: (a) for the uniform wall temperature case; (b) for co-current flow cases; (c) for the counter-current flow cases; and (d) for the uniform heat flux case

The annular diameter ratio and hydraulic diameter are influential geometric factors on the heat transfer coefficient’s magnitude. The annular diameter ratio is defined in this dissertation as the ratio of the outer diameter of the inner wall (D_1) to the inner diameter of the annulus (D_2). It is expressed mathematically in Equation 1.

$$a = \frac{D_1}{D_2}, (a \leq 1) \tag{1}$$

The annular hydraulic diameter for the annulus is expressed in Equation 2, where A_c is the annulus cross-sectional area for the flow and p the wetted perimeter of the cross-section.

$$D_h = \frac{4A_c}{p} = \frac{4\pi(D_2^2 - D_1^2)/4}{\pi(D_2 + D_1)} = D_2 - D_1 \tag{2}$$

In this context, it should be noted that concentric and eccentric tube-in-tube heat exchangers have been studied by researchers for over a century and an effort has been made to relate the heat transfer coefficient to the diameter ratio and/or the hydraulic diameter for specific flow conditions.

2.3 Definitions of heat transfer

This section covers some of the elementary definitions for heat transfer in annular flow passages and will feature often in the sections and chapters that follow in this dissertation. This section should be read against the backdrop of thermally and hydrodynamic developing flow, as was briefly covered in Chapter 1. Reference will be made to important concepts of boundary layer development.

As mentioned in Chapter 1, boundary layer development impacts on the rate at which heat can be transferred by convection (which relies on fluid motion) versus the rate at which heat can be transferred by conduction in the hydrodynamic boundary layer. Conduction relates to the transfer of thermal energy from particles with a higher to a lower energy content by the interaction between particles. The conduction heat transfer rate can be expressed mathematically using Fourier's law in Equation 3, where k refers to the thermal conductivity of the medium, A_c refers to the cross-sectional area (normal to the temperature gradient) and dT/dx refers to the temperature gradient.

$$\dot{Q}_{cond} = -kA_c\frac{dT}{dx} \tag{3}$$

Convection heat transfer relates to the transfer of energy between a solid surface and the adjacent fluid particles in motion. The rate of heat transfer by convection is expressed by Newton's law of cooling in Equation 4, where h is the convective heat transfer coefficient, A_s is the applicable surface area, and ΔT is the temperature difference between the surface and the fluid.

$$\dot{Q}_{conv} = hA_s\Delta T \tag{4}$$

The Reynolds number (Re) is a commonly used dimensionless number to define the flow regime of a fluid, which is expressed as the ratio of the inertia forces of the fluid to its viscous forces. The Reynolds number may be expressed mathematically, as in Equation 5, where ρ is the fluid density,

U is the fluid velocity, D_h is the hydraulic diameter, μ is the dynamic viscosity and v is the kinematic viscosity.

$$\mathrm{Re} = \frac{Inertia\ forces}{Viscous\ fores} = \frac{\rho U D_h}{\mu} = \frac{U D_h}{v} \tag{5}$$

Laminar flow (fluid characterised by molecules following parallel flow lines) generally occurs at low Reynolds numbers. As the Reynolds number increases, the flow tends to become more chaotic and turbulent in nature. Once the critical Reynolds number is reached, the transition from laminar to turbulent flow is initiated. This transitional flow regime region exists over a Reynolds number range and depends on upstream flow conditions, prevailing secondary flow and the local fluid passage geometry. For circular tubes, fully turbulent flow is expected at Reynolds numbers that exceed 10 000. However, in some applications, fully turbulent flow may be attained at Reynolds numbers as low as 4 000 (Çengel and Ghajar, 2011). As mentioned, turbulent flow is often favoured in heat transfer applications due to higher heat transfer rates. However, many operating conditions exist when the flow is classified as being either laminar or in transition (Meyer, 2014).

The Nusselt number (Nu) is a popular dimensionless heat transfer coefficient that is used to represent the enhancement in heat transfer by convection to conduction across the same boundary layer. The Nusselt number is defined in Equation 6, where h is the heat transfer coefficient and L is the characteristic dimension of the exposed surface. For flow passages, this is often selected to be D_h and k is the thermal conductivity of the fluid.

$$\mathrm{Nu} = \frac{hL}{k} = \frac{\dot{q}_{conv}}{\dot{q}_{cond}} \tag{6}$$

2.4 Convective heat transfer for circular tubes

Even though this investigation focuses on annular flow passages, it is important to take note of the convection heat transfer phenomenon in circular tubes. Since a circular tube has a simpler geometry and because it was investigated before significant attention was paid to annular flow passages, there is a wealth of relevant information that is common to convective heat transfer in other flow passage geometries, including annular flow passages.

Due to its importance, now as well as in the preceding century, numerous attempts have been made to develop accurate correlations with which to estimate heat transfer for circular tubes. Accurate correlations would eliminate the need for designers to make use of experimental and numerical results to size heat exchangers.

Circular tubes are favoured for heat transfer applications, as they allow for higher heat transfer rates and smaller pressure drops compared to the flow passages of other cross-sections. The tubes used for heat transfer applications are generally several times the length of the hydrodynamic and thermal entry lengths. Hence, the assumption is often made that the flow is fully developed for the entire length of the tube to simplify the correlation.

The theory of fluid flow in tubes for fully developed laminar flow is reasonably well understood. However, for complex flow situations, such as for turbulent, transitional or developing flow, researchers rely on experimental data and empirical relations to develop correlations. Experimental setups are, however, not perfectly accurate, and the experimental method is not fully repeatable, even in well-controlled laboratory conditions.

Popular correlations for the Nusselt number in the turbulent flow regime for fully developed flow in circular tubes are tabulated in Table 2-1.

Table 2-1: Popular correlations for the overall Nusselt numbers in smooth tubes

Author	**Equation number**	**Correlation**	**Reynolds number range (Re)**	**Prandtl number range (Pr)**
Dittus and Boelter (1930)	7	$\mathrm{Nu} = 0.023\mathrm{Re}^{0.8}\mathrm{Pr}^{n}$ • $n = 0.3$ for cooling • $n = 0.4$ for heating	Not specified	$0.6 - 160$
Colburn (1933)	8	$\mathrm{Nu} = 0.023\mathrm{Re}^{0.8}\mathrm{Pr}^{1/3}$	$\geq 10\,000$	$0.7 - 160$
Sieder and Tate (1936)	9	$\mathrm{Nu} = 0.027\mathrm{Re}^{0.8}\mathrm{Pr}^{\frac{1}{3}}\left(\frac{\mu_b}{\mu_w}\right)^{1/4}$	$\geq 10\,000$	$0.7 - 17\,600$
Prandtl (1942)	10	$\mathrm{Nu} = \frac{(f/8)\mathrm{RePr}}{1+8.7\sqrt{\frac{f}{8}}\left(\mathrm{Pr}^{\frac{2}{3}}-1\right)}$	$\geq 10\,000$	Not specified
McAdams (1954)	11	$\mathrm{Nu} = 0.023\mathrm{Re}^{0.8}\mathrm{Pr}^{\frac{1}{3}}\left(\frac{\mu_b}{\mu_w}\right)^{0.14}$	Not specified	$0.7 - 16\,700$
Gnielinski (1976)	12	$\mathrm{Nu} = \frac{\left(\frac{f}{8}\right)(\mathrm{Re}-1\,000)\mathrm{Pr}}{1+12.7\left(\frac{f}{8}\right)^{0.5}\left(\mathrm{Pr}^{\frac{2}{3}}-1\right)}$	$3\,000 - 500\,000$	$0.5 - 2000$

In this table, f refers to the friction factor, Pr refers to the Prandtl number of the fluid and μ refers to the relevant viscosity at the wall or the bulk fluid temperature. The friction factor may, for instance, be determined by relations proposed by Petukhov (1970) or Colebrook (1939). It can be seen that, in each of the correlations, the Reynolds number has an important impact on the Nusselt number and so does the Prandtl number. Three of the listed correlations consider the direction of heat flux. These are the Dittus and Boelter (1930) correlation, which makes use of different values of exponent n, and the Sieder and Tate (1936) and McAdams (1954) correlations, which make use of a viscosity ratio (μ_b/μ_w). It must be noted that the correlations in Table 2-1 have been developed to estimate the overall Nusselt numbers of a tube, overshadowing the heat transfer enhancement in the entrance region.

2.5 Local heat transfer coefficients for circular tubes

As mentioned, higher heat transfer rates are encountered in the thermally developing length of a flow passage. This is of practical importance for short tubes, whether operated in the laminar, transitional or turbulent flow regimes. Over the years, a number of analytical, numerical and experimental studies have been performed to determine the local Nusselt numbers ($\mathrm{Nu_l}$) in the thermal developing regions of a tube, as are summarised in Table 2-2, where subscript l refers to the dependence of the Nusselt number on the axial position along the tube length.

Nusselt (1931) was one of the first researchers to set up a correlation from experimental results, which is tabulated as Equation 13 in Table 2-2. The presence of a length-to-diameter ratio (L/D) is important, where L refers to the length of the tube.

Hausen (1943) developed a heat transfer correlation for the local Nusselt numbers by incorporating a term accounting for the length of the flow passage (see Equation 14 in Table 2-2). The term $\left(1+\left(\frac{L}{D}\right)^{2/3}\right)$ has been used by authors such as Gnielinski (2009) for their heat transfer correlations.

Another example of an experimental study to determine the local heat transfer coefficients is the one by Badus'haq (1993), who conducted tests with turbulent air flow through electrically heated tubes of different lengths. The local Nusselt numbers were calculated from temperature measurements made by thermocouples along the length of the tube. An increase in heat transfer was evident in the thermal developing region. Badus'haq proposed a correlation to estimate the local Nusselt number for a given Re, Pr and L/D ratio. This is contained in Table 2-2 as Equation 15.

Ghajar and Tam (1994) also experimentally measured the heat transfer coefficients in the inlet region. They considered a constant heat flux boundary condition and proposed a correlation for Nu in terms of $\mathrm{Re}, \mathrm{Pr}, L/D, \mu_b/\mu_w$ as Equation 17 in Table 2-2. It could be noted that they included a viscosity ratio to account for the direction of the heat transfer.

Gasljevic and Matthys (1997) experimentally studied the increase in friction factor and heat transfer in the entry region of a tube with a surfactant. They also developed a correlation relating the local Nusselt number to the overall Nusselt number to account for boundary layer development. This correlation is tabulated in Table 2-2 as Equation 18.

Table 2-2: Correlations for the local Nusselt numbers for turbulent flow in smooth tubes

Author	Equation number	Correlation	Range of Pr	Range of L/D
Nusselt (1931)	13	$\mathrm{Nu}_l = 0.036\mathrm{Re}^{0.8}\mathrm{Pr}^{0.333}\left(\frac{L}{D}\right)^{-0.055}$	Not specified	$10 - 400$
Hausen (1943)	14	$\mathrm{Nu}_l = 0.037(\mathrm{Re}^{0.75} - 180)\mathrm{Pr}^{0.42}\left[1 + \left(\frac{L}{D}\right)^{\frac{2}{3}}\right]$	Not specified	Not specified
Badus'haq (1993)	15	$\mathrm{Nu}_l = 1.92 * 10^{10}\mathrm{Re}_l^{0.81}\mathrm{Pr}_l^{0.4}\left[\frac{L}{D} + 1\,000\right]^{-3.978}$	$0.73 - 0.74$	$0 - 68.7$
Geankoplis (1993)	16	$\frac{\mathrm{Nu}_l}{\mathrm{Nu}_f} = 1 + \left(\frac{D}{L}\right)^{0.7}$	Not specified	$2 - 20$
Ghajar and Tam (1994)	17	$\mathrm{Nu}_l = 0.023\mathrm{Re}^{0.8}\mathrm{Pr}^{0.385}\left(\frac{L}{D}\right)^{-0.054}\left(\frac{\mu_b}{\mu_w}\right)^{0.14}$	$1 - 10$	Not specified
Gasljevic and Matthys (1997)	18	$\frac{\mathrm{Nu}_l}{\mathrm{Nu}_f} = 1.56e^{-0.0035\left(\frac{L}{D}\right)} + 5.3e^{-0.133\left(\frac{L}{D}\right)}$	$1 - 20$	Not specified

The correlations listed in Table 2-2 consider boundary layer development as a factor that is included in the correlations in which the length and diameter are typically noted and expressed to the power of a constant, as determined by the findings of the studies mentioned in the table. Correlations by Geankoplis (1993) and Gasljevic and Matthys (1997) are all expressed in terms of the Nusselt numbers for fully developed flow (Nu_f). The importance of the terms Re, Pr and L/D for heat transfer in a tube can be seen as all noted correlations are formed with these terms in Table 2-2.

A study by Peyghambarzadeh (2011) also deals with local Nusselt numbers. The study conducted sets of experiments on a 5 mm diameter horizontal tube that was exposed to constant heat fluxes of 1 300 W/m^2 and 3 000 W/m^2, and Reynolds numbers between 6 500 to 11 000. Some 11 thermocouple stations were located along the length of the tube for local wall temperature measurements, in which air was the working medium. Findings from the study indicate enhanced heat transfer in the entry region of the tube, as seen in Figure 2-3 (a). It was also confirmed that higher Reynolds numbers result in higher heat transfer rates, as depicted in Figure 2-3 (b).

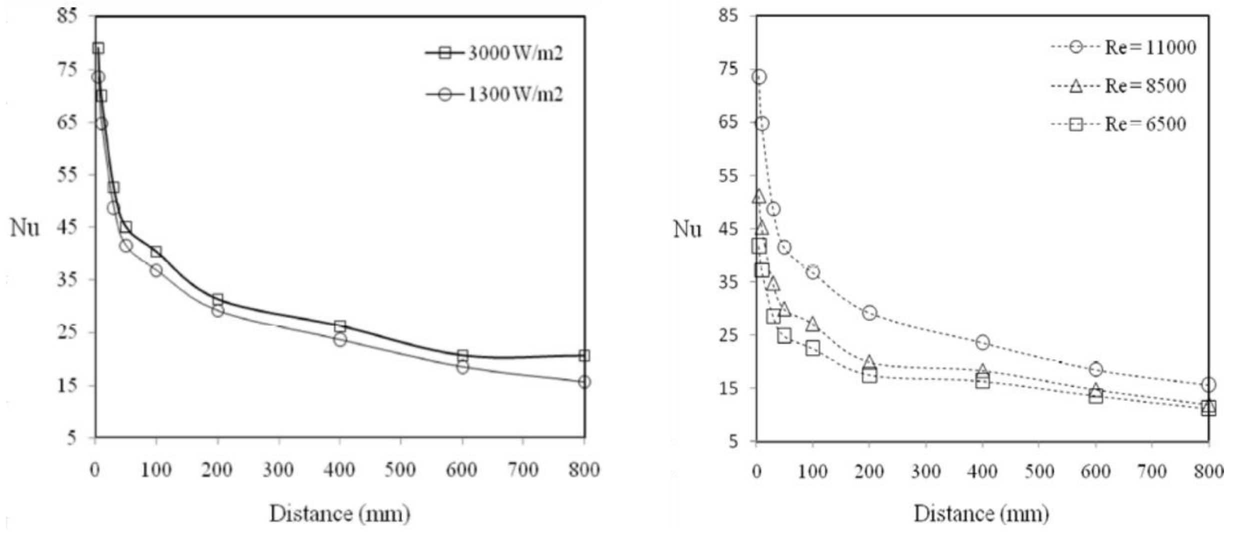

(a) (b)

Figure 2-3: Local Nusselt numbers along the axial length of a pipe for different conditions: (a) Re = 11 000 and varying heat fluxes; and (b) heat flux of 1 300 W/m^2 and varying Re numbers (Peyghambarzadeh, 2011)

In a recent study by Everts (2015), heat transfer and pressure drop measurements were performed for developing flow on a tube in the transitional flow regime. The test section consisted of an electrically heated tube, with an inner diameter of 11.52 mm and a length of 2.03 m. Flow rates were controlled from Reynolds numbers of 500 to 10 000 to cover laminar, transitional and turbulent flow.

Figure 2-4 shows a plot of the local Nusselt numbers along the length ratio of the tube x/D. Everts (2015) noted that the local Nusselt numbers decrease from the inlet. The local Nusselt numbers also tended to increase from x/D = 25 to x/D = 175 for the laminar and transitional flow regimes. For turbulent flow, Everts (2015) noted that the flow was fully developed in the region from x/D = 17, as the local Nusselt numbers remained relatively constant.

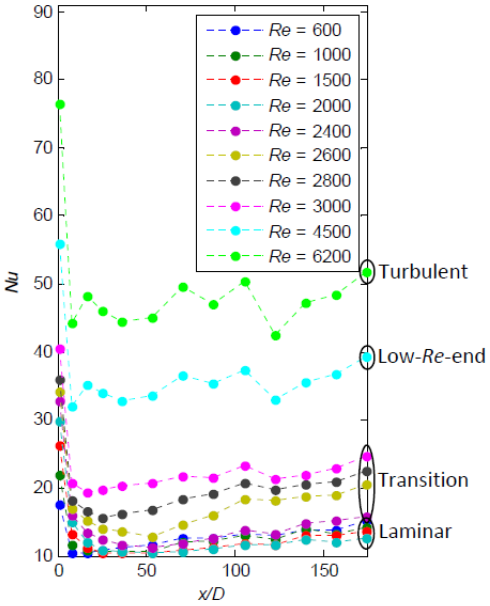

Figure 2-4: Local Nusselt numbers for a range of flow rates with a heat flux of 6.5 kW/m^2 (Everts, 2015)

2.6 Previous heat transfer investigations in annular flow passages

The correlations documented up to now were developed for circular tubes and are not necessarily valid for concentric annuli, even though researchers have found that the correlations of heat transfer in other flow passage geometries are similar in nature. In this section, specific attention is given to concentric flow passages, and the work of some researchers is summarised.

A comprehensive list of correlations has been set up to estimate heat transfer in a concentric annular flow passage. However, as highlighted by Dirker et al. (2004), these correlations are not all in good agreement, which could be due to the different quality levels of the experimental setups and the limitations for which they are valid, such as geometric parameters $(D_h, a, L/D_h)$. Gnielinski (2009) expressed the need for accurate experimental setups to study heat transfer in an annular flow passage, especially for turbulent flow.

2.6.1 Quarmby (1967)

Quarmby (1967) experimentally examined the local Nusselt numbers of concentric annuli with uniformly heated cores. Air was used as the working fluid for thermally developing flow in which the hydrodynamic boundary layer was fully developed. Four different diameter ratios between 2.88 and 9.14, and Reynolds numbers between 5 000 and 270 000 were investigated.

Quarmby (1967) set up a logarithmic correlation that expressed local Nusselt numbers as functions of Re and a. However, this correlation did not fully agree with his experimental results, as the correlation did not account for the change in air properties with temperature.

2.6.2 Lee (1968)

Lee (1968) investigated thermal boundary layer growth for the turbulent flow regime by considering the heat transfer of a concentric annulus by means of the momentum and heat transfer integral equations. The flow was hydrodynamically fully developed and exposed to a uniform heat flux from the inner tube. Diameter ratios ranging from 0.2 to 0.99, Reynolds numbers between 10 000 to 200 000 and Prandtl numbers from 0.01 to 30 were investigated.

The enhancement in heat transfer in the entrance region was plotted in Figure 2-5 for different flow scenarios along the annular flow passage. Lee (1968) found that the heat transfer is at its maximum at the inlet and decreases exponentially during boundary layer growth.

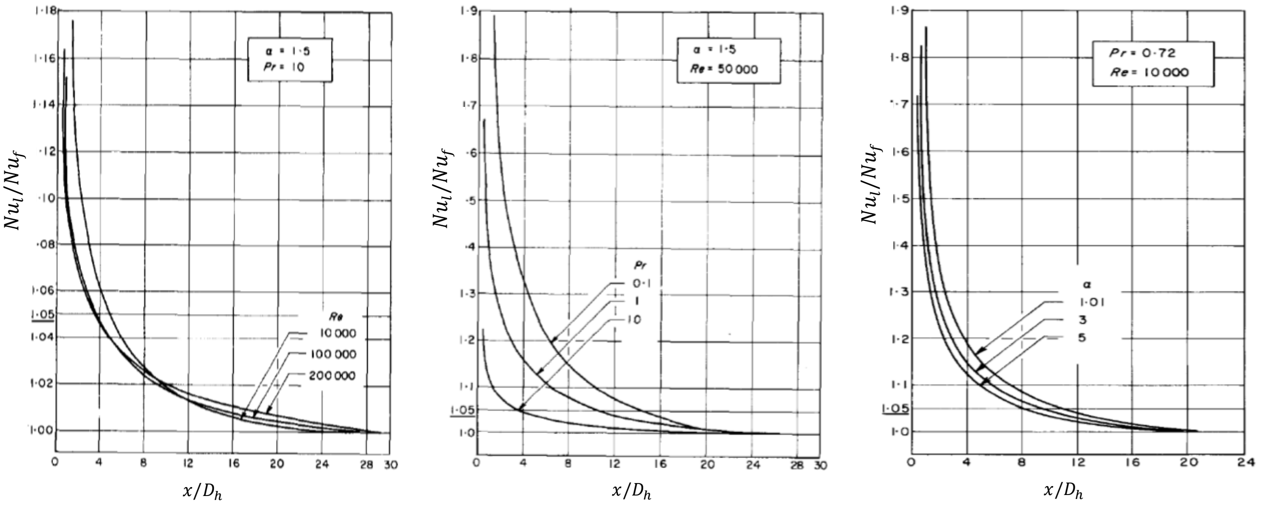

(a) (b) (c)

Figure 2-5: Enhancement in heat transfer during boundary layer growth for: (a) various Reynolds numbers; (b) various Prandtl numbers; and (c) various diameter ratios (notations adapted from Lee (1968))

From Figure 2-5 (a), it was deduced that, for a given Prandtl number and diameter ratio, the Reynolds number has a minor influence on the Nusselt number ratio, where higher Reynolds numbers result in smaller Nusselt number ratios in the proximity of the inlet region. From Figure 2-5 (b), it could be noted that the Prandtl number had a major influence on the Nusselt number ratio at the inlet region, with a higher Prandtl number resulting in a higher heat transfer rate. In addition, it was noted that, as the Prandtl number increases, the thermally developing length decreases. Smaller radii ratios result in slightly higher heat transfer rates. However, the difference in heat transfer for diameter ratios is small, as seen in Figure 2-5 (c).

Even though the results give insight into the heat transfer characteristics at the inlet of an annulus, only the flow at the inlet is considered to be hydrodynamically fully developed. This is very difficult to achieve practically, since almost all applications have a 90° elbow inlet (see Figure 2-1). This reduced the significance of their work and there is still a need to investigate cases that resemble practical layouts of tube-in-tube heat exchangers.

2.6.3 Dirker and Meyer (2005)

In an study undertaken by Dirker and Meyer (2005), Nusselt numbers of concentric annuli were experimentally determined for six horizontal concentric counter-flow tube-in-tube annular flow passages. Diameter ratios varied from 0.3125 to 0.589 and Reynolds numbers from 4 000 to 30 000.

From the experimental results, Dirker and Meyer (2005) published a correlation to estimate the Nusselt number for both the inner and outer tubes of a concentric annulus. These are tabulated in Table 2-3 as equations 21 and 22. The published correlations predicted their experimental results within 3% when making use of the Wilson plot method.

2.6.4 Gnielinski (2009)

Gnielinski (2009) also developed a correlation to estimate the Nusselt numbers of concentric annuli of a particular length in turbulent flow by making use of an existing experimental data and correlations. He made use of a semi-empirical type of equation and expanded the correlation published by Prandtl (1942), as seen in Table 2-1 (Equation 10), to account for boundary layer development by including an entrance region factor as derived by Hausen (1943) (Equation 14). Additional factors were included in the correlations, such as to account for the heat transfer direction, change in fluid properties and a friction factor, to name a few. The correlation developed by Gnielinski (2009) for the Nusselt number and its relative terms can be seen in Equations 24 to 30 in Table 2-3.

Gnielinski (2009) examined the accuracy of his correlation by comparing it to existing experimental data and found that his correlation anticipated experimentally measured local Nusselt numbers with good accuracy. Gnielinski (2009) found that his correlation under predicted the Nusselt numbers measured by Dirker and Meyer (2005) by 15%.

2.6.5 Van Zyl et al*.* (2013)

Van Zyl et al. (2013) experimentally studied the effect that the diameter ratio has on the heat transfer and pressure drop for both cooled and heated annuli for different turbulent flow rates. The experimental setup consisted of four 5.5 m-long concentric annuli with different diameter ratios. Temperatures of the tubes were measured by means of thermocouple stations to study local heat transfer. Shown in Figure 2-6 are the local Nusselt numbers along the length of the flow passage for different flow rates.

Van Zyl et al. (2013) found that the local Nusselt numbers were significantly influenced by Reynolds numbers. The local Nusselt numbers were highest at the inlet and decreased along the flow passage due to boundary layer development.

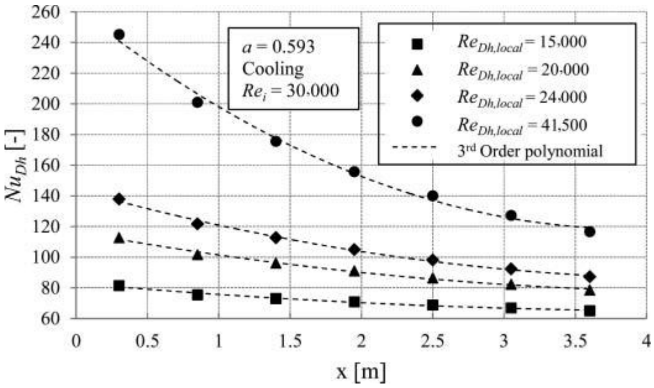

Figure 2-6: Local Nusselt numbers for a cooled annulus for varying Reynolds numbers (Van Zyl et al., 2013)

2.6.6 Prinsloo et al. (2014)

Heat transfer and pressure drop measurements were made by Prinsloo et al. (2014) in a counter-flow concentric annuli of 5.5 m in length. Their test was performed with different Reynolds numbers ranging from 10 000 to 50 000, different annular ratios of 0.327, 0.409 and 0.483, and different inlet temperatures.

The test section was divided into eight sections, each with a length of 0.79 m. Thermocouples were used to measure the surface temperature of the inner tube. The authors noted a decrease in the Nusselt numbers from the inlet to further down the flow passage (see Figure 2-7).

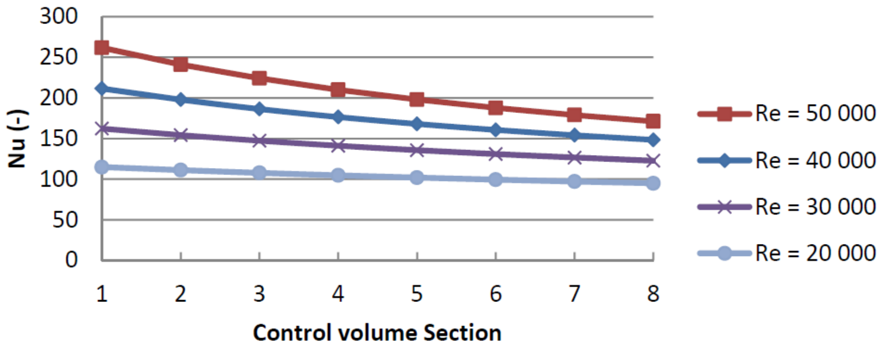

Figure 2-7: Local Nusselt numbers along the length of the annular flow passage of counter-flow concentric annuli for a range of Nusselt numbers (Prinsloo et al., 2014)

2.6.7 Van der Westhuizen et al. (2014)

Van der Westhuizen et al. (2014) also conducted heat transfer studies in concentric annuli using TLCs for surface temperature measurements. TLCs were used instead of thermocouples to extract full temperature fields of the annular flow passage.

The authors noted larger heat transfer coefficients at the inlet region of the flow passage to those found further along the flow passage as shown in Figure 2-8 (a). Heated and cooled annuli experiments were conducted, with the results shown for the heated annuli case. Higher flow rates result in higher heat transfer rates.

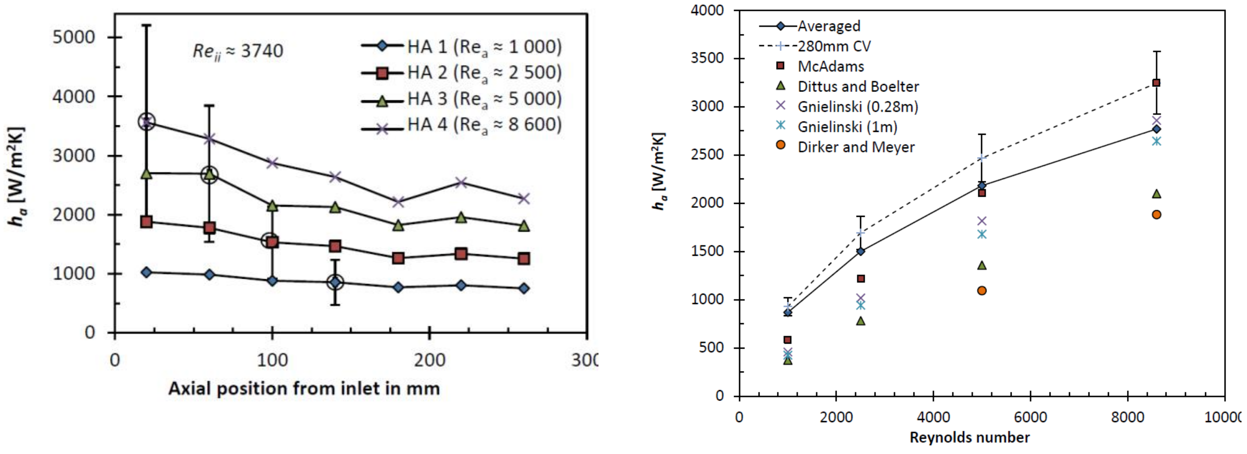

(a) (b)

Figure 2-8: The experimental results of: (a) heat transfer coefficients in the annuli (h_a) at different axial location for varying Re; and (b) heat transfer coefficient in the annuli (h_a) for existing correlations for increasing Re (image from Van der Westhuizen et al. (2014))

Figure 2-8 (b) shows the overall heat transfer coefficients compared to developed correlations. The study's findings suggested a 46% increase in heat transfer, compared to existing correlations, which may be due to some correlations neglecting the increase in heat transfer at the inlet region. The authors noted large uncertainties in their results, which were attributed to bulk fluid temperature measurements made inside the inner tube of the concentric annular flow passage.

As this study will implement a similar technique of measuring surface temperature, the work done by Van der Westhuizen et al. (2014) will be considered further in Section 2.8.5.

2.6.8 Some heat transfer correlations for concentric annuli

Correlations for concentric annuli have been set up since the 1950s and more are being added as more research is carried out with more accurate experimental setups. Some of these correlations are tabulated in Table 2-3. A relatively large number of additional correlations are omitted from this table and only the most familiar ones are tabulated.

Table 2-3: Correlations for the Nusselt numbers in a smooth concentric annulus for turbulent flow

Author	**Equation number**	**Correlation**	**Diameter ratio (a)**	**Re_{Dh} range**	**Medium/ Pr range**
McAdams (1954)	19	$\mathrm{Nu}_{Dh} = 0.03105a^{0.15}(a^{-1}-1)^{0.2}\mathrm{Re}_{D_h}^{0.8}\mathrm{Pr}^{\frac{1}{3}}\left(\frac{\mu_b}{\mu_w}\right)^{0.14}$	$1.5E-4-0.85$	Not specified	All
Dirker and Meyer (2005)	20 21 22	$\mathrm{Nu}_{D_h} = C_o\mathrm{Re}_{D_h}^{P}\,\mathrm{Pr}^{\frac{1}{3}}\left(\frac{\mu_b}{\mu_w}\right)^{0.14}$ $P = 1.013e^{0.067a}$ where P andC_o are influenced by geometry $C_o = \frac{0.003a^{1.86}}{0.063a^{-3}-0.674a^{-2}+2.225a^{-1}-1.157}$	$0.31-0.59$	$4\,000-30\,000$	Water
Swamee et al. (2008)	23	$\mathrm{Nu}_{D_h} = \frac{0.027}{\left(1+\frac{1}{a}\right)^{0.2}}\mathrm{Re}_{D_h}^{0.8}\mathrm{Pr}_o^{\frac{1}{3}}\left(\frac{\mu_o}{\mu_{iw}}\right)^{0.14}$	Not specified	Not specified	Not specified
Gnielinski (2009)	24 25 26 27 28 29 30	$\mathrm{Nu}_{D_h} = \frac{\left(\frac{f}{8}\right)\mathrm{Re}_{D_h}\mathrm{Pr_a}}{\varphi+12.7\sqrt{\left(\frac{f}{8}\right)}\left(\mathrm{Pr}_a^{\frac{2}{3}}-1\right)}\left(1+\left(\frac{D_h}{L}\right)^{2/3}\right)F_{ann}K$ $\varphi = 1.07+\frac{900}{\mathrm{Re}_{D_h}}-\frac{0.63}{1+10\mathrm{Pr}_a}$ $K = \left(\frac{\mathrm{Pr}_a}{\mathrm{Pr}_{iw}}\right)^{0.11}$ for liquids $K = \left(\frac{T_b}{T_{iw}}\right)^{n}$ for gases and $n = 0$ for cooling $n = 0.45$ with $0.5 < \frac{T_b}{T_{iw}} < 1.0$ $F_a = 0.75a^{-0.17}$ $f = (1.8\log_{10}\mathrm{Re}^{*}-1.5)^{-2}$ $\mathrm{Re}^{*} = \mathrm{Re}_{D_h}\frac{(1+a^2)lna+(1-a^2)}{(1-a)^2\ln a}$	Not specified	$> 10\,000$	All

The correlations noted in Table 2-3 all depend on Re, Pr, a, and a ratio, considering the temperature of the bulk fluid and wetted wall temperature expressed as μ_b/μ_w, Pr_b/Pr_w or T_b/T_w. The only correlation, which was found during the time of compiling this investigation that considers boundary layer development for turbulent flow is the one developed by Gnielinski (2009). This correlation is shown as Equation 24. The majority of heat transfer studies used thermocouples to measure the wall and bulk fluid temperatures. Thermocouples provide limited possibility in accurately measuring a temperature field in the entry region of an annulus without influencing the flow. Thus, an alternative technique for measuring temperature is required.

2.7 The effect of different inlet configurations

The inlet configurations for flow to a flow passage have been found to significantly influence heat transfer and the transition from laminar to turbulent flow (expressed by the critical Reynolds numbers). Past studies on annular flow passages only investigated the different inlet configurations. No previous studies that dealt specifically with the influence on heat transfer for inlets of different sizes to the annular flow passages could be found, as only the inlet flow geometry was considered. For this reason, a short overview of inlet effects with other types of flow channels is considered here.

Some inlet geometries for circular flow channels include bell-mouth, re-entrant and square-edged inlet types. The inlets have different shapes that affect fluid flow. For instance, the square-edged inlet is prone to increase the level of turbulence, while the bell-mouth inlet initiates the formation of eddies. A number of authors have found the inlet configuration to have a profound effect on the transitional Reynolds number (Meyer and Olivier, 2011), (Tam and Ghajar, 1997).

Mohammed (2009) experimentally investigated the inlet geometry's influence on a horizontal tube under constant heat flux in the laminar flow regime. The inlet configurations tested were the bell-mouth and sharp-edged entrances. Results from his findings suggest that the local Nusselt numbers were largest for the bell-mouth inlet geometry in the laminar flow regime.

In a study by Dirker et al*.* (2014), the heat transfer and pressure drop for the inlet geometries of sudden contraction, bell-mouth and an induced swirl effect were investigated for rectangular micro channels. Experiments were run with uniform heating and Reynolds numbers from 300 to 2 800 to cover both laminar and transitional flow. Water was used as the working fluid. Hydraulic diameters ranged from 0.57 mm, 0.85 mm and 1.05 mm and L/D ratios from 190, 235 and 350.

Swirl was created in the flow with an inlet that had two off-centre holes at the top and bottom of the channel inlet. The results of the investigation suggest that the swirl inlet type exhibited the highest friction factors and Nusselt numbers for the different tested inlets and the flow rate range. Increases in overall Nusselt numbers from 31% to 149% were noted for the swirl type compared to the sudden contraction inlet due to the altered flow pattern that improved the mixing in the flow passage. The results from the investigation of Dirker et al. (2014) only covered the range from laminar to transitional flow and not turbulent flow. The different inlet geometries were located in-line with the flow passage, as this was only found with certain flow passage heat exchangers.

2.8 Fundamentals and previous studies that implemented liquid crystal thermography

For the majority of heat transfer studies, as discussed in sections 2.5 to 2.7, thermocouples were used for local temperature measurements from which local heat transfer coefficients were derived. However, these have some drawbacks, as they interfere with the heat transfer and fluid flow, and are impractical for generating a thermal map of a body. Other techniques for measuring temperature have their own drawbacks and limitations.

Optical methods for measuring temperature, such as infrared imaging, eliminate the need for the vast number of thermocouples. Infrared imaging provides high-resolution temperature maps. However, they are inherent to experimental noise and require the body under investigation to be made of materials that are transparent to radiation.

As mentioned, liquid crystal thermography (LCT) is another optical technique for measuring temperature that makes use of TLCs to provide a thermal map of a body. The orientation of the TLCs' lattice is a function of its temperature, meaning that TLCs selectively reflect light at different temperatures (Camci). TLCs do not interfere with fluid flow or local heat fluxes. LCT has gained market interest due to its affordability, convenience and broad application spectrum (Hallcrest, 2014a). TLCs' have previously been employed in heat transfer research to determine convective heat transfer coefficients.

TLCs have been implemented in a number of heat transfer studies since the 1960s, with particular emphasis on engine and turbine components with air as the working fluid. Only a limited number of heat transfer studies have been carried out with water as the working fluid due to the difficulty in protecting the TLCs from being washed away. Past heat transfer studies in which TLCs were used as a technique to measure temperature is discussed in the following sections.

2.8.1 Ogden and Hendricks (1984)

In a study presented by Ogden and Hendricks (1984), TLCs were used to identify the temperature field of an ellipsoid placed in a heated water tunnel. In this study, emphasis was placed on how TLCs were shielded from chemical contamination and the shear stress of the water flowing over the surface. The TLC layer was shielded by a thin acrylic layer.

2.8.2 Stasiek and Kowalewski (2002)

Stasiek and Kowalewski (2002) implemented TLCs as a non-evasive method to investigate temperature fields and fluid flow over complex heat exchanger parts.

Their work covered a large range of studies, including steady- and transient-state studies. The heat exchanger elements studied included square and rib-roughened channel elements, cross-corrugated, undulated elements (used in rotary heat exchangers) and flat-plate heat exchanger elements. Tests were run for Reynolds numbers ranging from 500 to 50 000 and temperatures ranging from 25 ˚C to 65 ˚C.

The work by Stasiek and Kowalewski (2002) highlighted the potential of implementing TLCs as a technique to measure temperature from which heat transfer coefficients can be determined.

2.8.3 Muwanga and Hassan (2006)

Muwanga and Hassan (2006) implemented uncapsulated TLCs to study local heat transfer in micro channels. Water was heated uniformly in a channel with a diameter of 0.254 mm.

Localised TLC calibrations were performed to account for any non-uniformities in the coating and variations in viewing and lighting angles. The calibration was carried out by circulating water of a known temperature through the tube and capturing the hue response. This was carried out before and after each experiment to confirm the integrity of the TLCs.

The results of the experiments for turbulent flow were in good agreement with the heat transfer correlation proposed by Gnielinski (1976). For laminar flow, however, the anticipated heat transfer was less than predicted by the correlation of Dittus and Boelter (1930). This investigation developed a method in which TLCs could be implemented in local heat transfer studies.

2.8.4 Lam et al*.* (2013)

Lam et al. (2013) devised an experiment to evaluate the surface temperature field of horizontal macro and micro tubes. Water was used as the working medium in the tubes, which varied in diameters from 1 mm to 2 mm. The tubes were heated by a uniform heat flux, and the temperature response was analysed by the TLCs applied to the surface. TLCs were used instead of thermocouples to eliminate the shunt effect caused by the thermocouples.

The temperature response of the TLCs was recorded with a camera and mirrors to capture the entire surface of the tube. The TLCs were calibrated by two cubic polynomials, one for the direct view and the other for the reflected view.

The focus of the study was to establish an experimental procedure by which the micro tube heat transfer could be determined. The derived heat transfer agreed with published correlations.

2.8.5 Van der Westhuizen et al. (2014)

Van der Westhuizen et al. (2014) developed a methodology to extract the temperature field and local heat transfer coefficients of the inner tube of an annular flow passage by means of TLCs.

The flow passage consisted of three concentric tubes, as seen in Figure 2-9 (a). Tube 1 served as the outer tube of the annulus and tube 2 as the inner tube of the flow passage. Tube 3 comprised 11 axial temperature-measuring stations to determine the local water temperature of the inner tube. The outer surface of tube 2 was treated with TLCs and was protected by means of a resin layer. Tube 3 was manufactured from plexiglass so that the TLCs were visible from the outside. The experimental setup was designed so that any of the flow passages could be connected to cold or warm water flow loops.

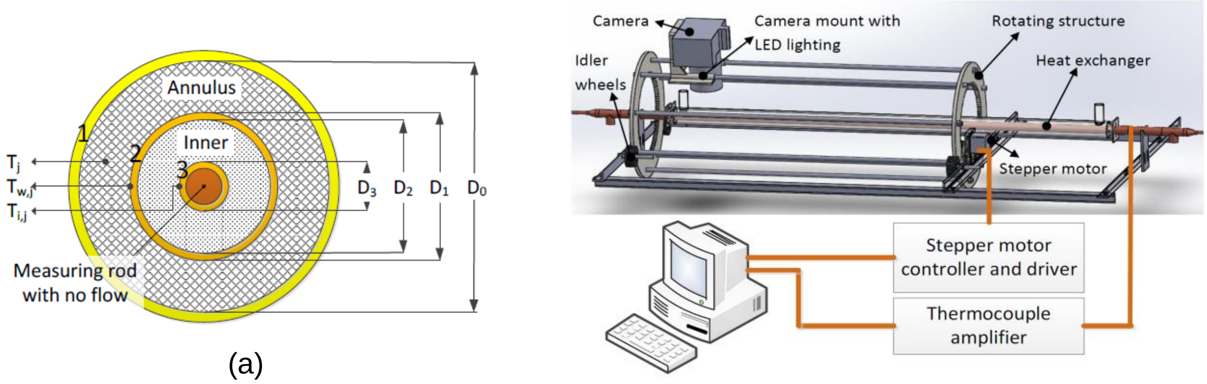

(a)

(b)

Figure 2-9: (a) The concentric tube layout; and (b) the experimental setup diagram (image from Van der Westhuizen et al. (2014))

A semi-autonomous mechanism was manufactured to capture photographs of the TLC surface. This mechanism, which can be seen in Figure 2-9 (b), would capture the response of the TLC surface so that the surface could be stitched together. A camera was fixed to a rotating cage that was rotated around the heat exchanger by means of a stepper motor. Adjustments in the axial direction were done by hand.

Experiments for heated and cooled annuli were conducted with a diameter ratio of 0.54. Reynolds numbers for the test cases were 1 000 to 8 000 and 1 000 to 13 800 for the heated and cooled annuli respectively. The warm and cold inlet temperatures ranged from 20˚C to 43˚C, which was limited by the bandwidth of the TLCs used in the experiment.

The TLC surface was calibrated by a gradient calibration technique by circulating water of a known temperature through the flow passage and capturing its hue response. For the experiments, the hue values of the TLC surface were extracted, converted to temperature and the associative temperature field stitched together.

Section 2.6.7 offers a short description of the results. The uncertainties of the experimental setup were generally small. However, large uncertainties in the order of 180% were noted for the temperature measurements inside tube 3, as can be seen in Figure 2-9 (a).

The results of the investigation suggest that LCT is a viable technique for measuring temperature for water-based heat transfer investigations. The increase in heat transfer in the inlet region of a short-tube heat exchanger is often neglected, as can be seen from the experimental results.

In this study, the methodology developed by Van der Westhuizen et al. (2014) will be implemented in heat transfer studies of concentric annuli. To reduce the uncertainties encountered by Van der Westhuizen et al. (2014), the inner tube will be replaced by a constant heat flux source, as recommended by the authors. A fully autonomous image-capturing mechanism will be developed to capture more detailed surface temperature fields and reduce the experimentation time. The detailed surface temperature fields will be used to determine the local heat transfer coefficients for different inlet types and to study the transition from laminar to turbulent flow.

2.9 Summary

This chapter provided a brief overview and definitions of annular flow passages and the heat transfer encountered in these passages. Convective heat transfer in tubes was considered due to similarities in the heat transfer mechanisms and the abundance of data. Existing correlations were noted for both overall and local heat transfer in tubes.

Past studies that investigated convective heat transfer in annular flow passages were considered with particular attention to the local heat transfer coefficients along the flow passage. Limited literature is available on the heat transfer at the inlet region of a concentric annular flow passage, as well as on the influence on heat transfer for inlets of different sizes for annular flow passages.

LCT was presented as a viable alternative to thermocouples to capture the local temperature field of an annular flow passage. Past studies that used TLC as a technique to measure temperature were presented, with a focus on the study of Van der Westhuizen et al. (2014) in which TLCs were used in heat transfer studies of concentric annular flow passages.

3. Experimental setup

This chapter is dedicated to the experimental setup and experimental method. The main requirements of the experimental facility and the test section were to sustain controlled water flow rates and thermal inlet conditions, sustain heat transfer, capture the heat fluxes on the heat transfer surface, capture bulk inlet and outlet fluid properties, and autonomously capture the TLC colour response so that the exact location of each photograph is known. It is important to note that, due to the shortcomings of the work of Van der Westhuizen et al. (2015), the inner tube of the annular flow passage in this study consisted of a constant heat flux heating rod to reduce the levels of uncertainties in the investigation. Therefore, in this investigation only a uniform heat flux boundary condition is considered. Special care had to be taken to design and produce this rod, as will be discussed in the later sections of this chapter.

In the first section of this chapter, the experimental facility is described, followed by a section dedicated to the test section itself and then a section describing the thermography mechanism. The experimental methodology and test matrixes are discussed towards the end of the chapter.

3.1 Experimental facility

The experimental facility is depicted in Figure 3-1. The facility consisted of a cold water loop and the test section that was electrically heated (as will be described in more detail in Section 3.2).

Water was supplied to the flow loop from a 1 000-litre reservoir that was kept between 20 ˚C and 21 ˚C via the use of a 45 kW thermostatically controlled chiller. An electronically controlled positive displacement pump, with a maximum pumping capacity of 2 000 l/h, was used to achieve the required mass flow rates through the test section. The positive displacement pump was controlled by frequency drives so that specific mass flow rates could be achieved by increasing or decreasing the pump speeds. A four-litre blade accumulator was installed downstream from the positive displacement pump to dampen flow pulsations caused by the pump. The accumulator would ensure more consistent flow rate readings.

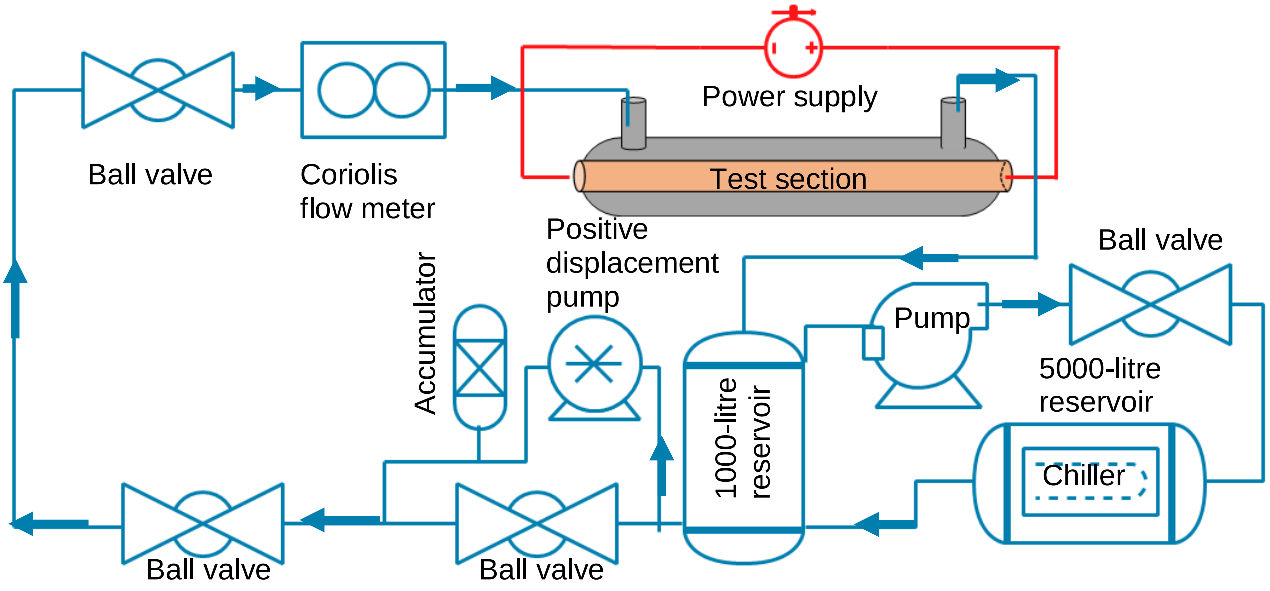

Figure 3-1: Experimental facility

A Coriolis flow rate meter was employed with a flow rate range of 0.0151 kg/s to 0.606 kg/s and a measurement uncertainty of 0.11% of the reading. Ball valves were installed at various locations in the flow loop to allow, restrict or block flow to certain sections of the flow loop.

Flow rate and temperature measurements were made by a data acquisition system that consisted of a National Instruments SCXI-1303 data card, a SCXI-1102 Thermocouple input module and a SCXI-1001 chassis, all connected to a personal computer with LabVIEW software.

The test section was heated by an Elektro-Automatik (EA 8360-30) DC power supply, which is discussed in more detail in Section 3.2.1 .

3.2 Test section

A short concentric annular flow passage, similar to the one schematically depicted in Figure 3-1, was manufactured. This acted as the test section. For this investigation, the inner wall of the flow passage was obtained using a uniform heat flux heating rod, as mentioned earlier. Water entered the annulus though the inlet orientated at 90˚ with respect to the flow passage length. In the test section, heat was transferred to the water from the heating rod, after which it exited the flow passage through an outlet, which was also orientated at 90˚.

A depiction of the annular flow passage is given in Figure 3-2. The figure shows the structure of the inner heating rod (outer diameter of D_1) within a transparent outer plexiglass tube (inner diameter of D_2) in relation to the 90˚ inlet section (inner diameter of D_3).

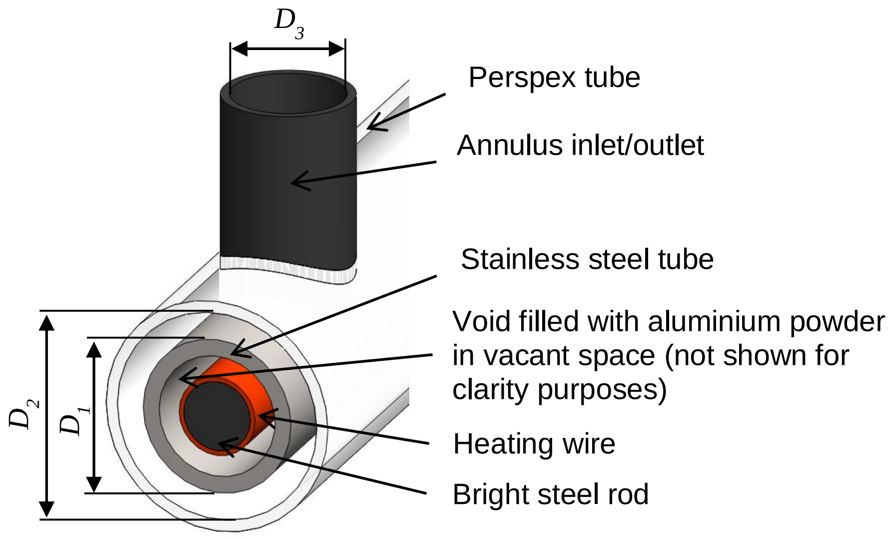

Figure 3-2: Cross-sectional view of the annular flow passage

3.2.1 Heating rod

Using a heating rod operated with a uniform heat flux offered a convenient method of obtaining the heat fluxes at the wetted wall. Such heat fluxes were later used to calculate the local heat transfer coefficients. It was therefore vital that the heating rod be manufactured with high accuracy to avoid local hot and cold spots that would jeopardise the study.

The construction of the heating rod with its subcomponents and annulus can be seen in Figure 3-2. The heating rod consisted of several layers placed around a 12 mm bright steel rod. Firstly, two constantan wires, which were insulated with polyvinyl chloride (PVC), were tightly wound around the bright steel rod. The wires were electrically connected in parallel with each other and acted as the heating element in the rod assembly. The effective electrical resistance was 44.4Ω (±0.1 Ω) and the maximum operating temperature was 140 ˚C. The bright steel rod, along with the heating wire, was carefully placed concentrically in a seamless tube made of 304 stainless steel that had outer and inner diameters of 26.67 mm and 20.93 mm respectively. The thermal conductivity of the stainless steel tube was 14.9 W/mK (Çengel and Ghajar, 2011). Both the stainless steel tube and the bright steel rod were manufactured to be 1 m, ±1 mm in length.

End caps were machined to ensure that the rod with heating wire maintained its concentric position. The 3.5 mm annular void between the stainless steel tube and the wound bright steel rod was filled with aluminium powder to reduce the thermal resistance between the heating wire and the outer surface of the stainless steel tube. The aluminium powder was pure, with a consistency comparable to that of flour. The thermal conductivity of the aluminium powder was estimated by experimentally determining its density when packed closely. The ratio of the volume occupied by air and aluminium was considered and the effective thermal conductivity was calculated to be 61.4 W/mK. The heating rod assembly was vibrated on a vibrating table while the aluminium powder was poured into the annular space. This ensured that the aluminium powder was compact and uniformly packed.

The uniformity of the heat flux was evaluated by powering the heating wire in the heating rod with an external power supply. The surface temperature of the complete heating rod was evaluated by means of a thermal camera. The surface of the heating rod was painted with matt black spray paint to ensure a uniform emissivity. A ThermaCAM E65 thermal camera with a thermal sensitivity of 0.1 ˚C at 30 ˚C, temperature range of -20 ˚C to 250 ˚C and accuracy of ±2 ˚C was used.

To assess the uniformity, the heating rod was powered to 80 W for 60 seconds, during which thermal images were taken of the heating rod's surface. This was done to ensure that the temperature of the heating wire did not exceed its operating temperature, which would result in the heating wire burning out. The power supplied to the heating rod was limited to 80W, to prevent burnout of the heating wire. Higher heating rates of 400 W would be anticipated during the experiments.

A typical image taken with the thermal camera for the investigation can be seen in Figure 3-3. Based on the surface temperature, which was found to be uniform, no significant hot or cold spots were evident along the axial length or circumference on the surface of the heating rod for the given heating rate of 80 W. Therefore, it was concluded that the manufactured heating rod was suitable for producing a uniform heat flux for the lower heating rate of 80 W, which was lower than the one used in the experiments.

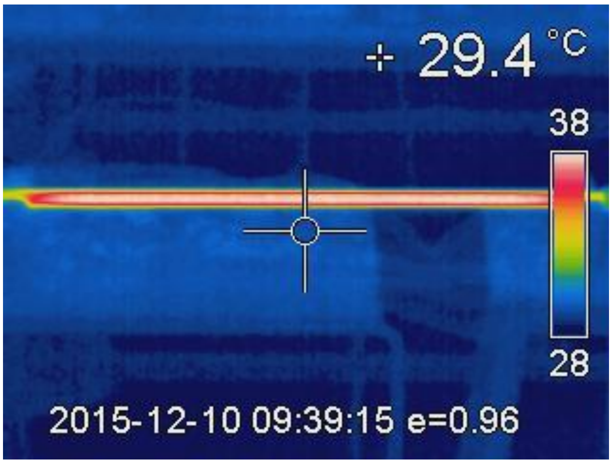

Figure 3-3: Image from the thermal camera of the temperature field of the heating rod

In addition to the uniformity of the heat flux, the axial heat conduction ability of the heating rod had to be analysed to determine if significant axial heat conduction might be present during experimental tests, which might influence the accuracy of the heat transfer data. The magnitude of axial heat conduction in the heating rod was examined analytically using a method prescribed by Maranzana et al. (2004). The method involves calculating a non-dimensional number (known as the M factor), which relates to the heat transfer rate by conduction in the axial direction as a ratio (or fraction) to the total heat transfer rate in the test section.

When using traditional analysis methods to determine convection heat transfer coefficients, Maranzana et al. (2004) suggest that the influence of axial conduction could be neglected if the M factor is smaller than 0.01 (less than 1% of the total heat transfer is passed down the axial direction via conduction). The worst case in terms of axial heat conduction is generally at low fluid flow rates. Based on the material properties of the heating rod assembly, the dimensions of the test section and the flow rate range under consideration in this investigation, it was found that the M factor for this study was well below 0.1. It had a maximum value 0.001 (0.01%) at the lowest Reynolds number condition. Therefore, the effect of axial heat conduction on the relevance of the results of this study is insignificant.

The heating wire in the heating rod was powdered by an Elektro-Automatik (EA 8360-30) with power, current and voltage ratings of 3 kW, 360 V and 30 A respectively, with an uncertainty of 0.2% of the displayed reading.

3.2.2 TLC layer

As mentioned, LCT was employed in this study to evaluate the surface temperatures on the inner wall of the annular duct. For this purpose, TLCs were applied to the outer surface of the heating rod, as depicted in Figure 3-2. The crystals used in this study were cholesteric or chiral nematic liquid crystals that optically react to changes in temperature by altering their colour (Hallcrest, 2014a).

The orientation of the crystals' lattice is a function of its temperature, which means that TLCs selectively reflect light at different temperatures. TLCs can be classified as being either temperature sensitive or temperature insensitive (shear-sensitive mixtures). Temperature sensitive TLC mixtures have a specific bandwidth in which they reflect bright colours that vary from 1° C to 20 °C (Hallcrest, 2014a). Liquid crystals have two distinct melting points at which the crystals are "activated" and reflect bright colours. The crystals change from invisible (in the visible spectrum) to red in colour when heated past the lower melting point, known as the activation point. When elevating its temperature further, the crystals appear as different colours of the visible spectrum altering from red to orange, yellow, green, blue and finally violet, after which the crystals revert back (outside the visible spectrum) at the higher melting temperature (Camci, 2008). The process of colour change with temperature is reversible and repeatable, if operated within in the visible colour range to prevent hysteresis of the crystals as discussed in Section 4.1, which deals with the calibration of the TLC's.

This permits a calibration to be performed between the reflected colour and temperature, allowing researchers to determine the temperature of the crystals by using visual means only.

Sprayable, water-based TLCs manufactured by LCR Hallcrest were used in this study. These TLCs were specified to have an activation temperature of 20 ˚C, ±1 ˚C and a bandwidth of 13 ˚C. However, it was found that the TLC used in this investigation had an active bandwidth from 19.8 ˚C to 34 ˚C. The uncertainty of the liquid crystals was ±1% of the bandwidth as stated by the manufactures of the TLCs, which equated to 0.13 ˚C. This uncertainty was used throughout the report although other authors have mentioned TLC's to be accurate to 0.1 ˚C (Piasecka, 2013) The experiments were all conducted before the liquid crystals' expiry date.

Before applying the TLC coat, a black base coat was applied to the surface of the stainless steel tube to ensure a uniform undercoat. The TLC coat and the base coat were applied to the heating rod with an airbrush. To ensure a smooth, uniform coating, a lathe was used to aid with the spraying process. The heating rod was secured in the chuck and tailstock of the lathe. The airbrush was placed in a purpose-built bracket that fixed the trigger of the airbrush during the spraying process. This ensured a constant spraying rate. The airbrush bracket was secured to the tool post of the lathe. Once operated, the heating rod would rotate in the lathe and the tool post would move along the length of the heating rod at a predetermined feeding to ensure a uniform application of the TLCs and base coat. A uniform application was desired to ensure that the entire heating rod surface had the same colour change with temperature. Only 660 mm of the heating rod was covered with TLCs due to length limitations of the imaging mechanism, which will be discussed in Section 3.3

The TLC mixture was water-based and soluble in water. Thus, additional care was needed to protect the TLC layers from the water flowing in the annulus. A transparent self-adhesive PVC film was applied over the TLCs to cover and protect the crystals. The protective film covered the entire length of the heating rod to ensure that the heating rod's diameter did not change. The adhesive layer was completely translucent and was commercially distributed as 10 m x 50 mm sheets rolled into a cylinder. A single sheet was wrapped twice around the crystals, which formed a protective layer with a thickness of 0.162 mm. The thickness of this protective layer was calculated by comparing the diameter of the heating rod with TLC before and after the protective adhesive layer was applied. The diameters were measured by means of a micrometer, with uncertainty of 10 µm at 50 random locations with and without the protective layer.

The adhesive film was applied with great care to ensure that no foreign material or air bubbles were trapped between the TLC layer and the PVC film. The indicated colour of the TLC would represent the thermal temperature state on the inside of the PVC film, not the wetted outside of the PVC film. For that reason, the effective thermal resistance of the PVC film and its interface, which would result in a temperature difference of the protective layer, had to be carefully measured. More information on this is supplied in Section 4.5.

3.2.3 Plexiglass tube

The outer wall of the annulus consisted of a plexiglass tube (see Figure 3-2). A transparent plexiglass tube was chosen to allow for a clear view of the TLC-covered surface. The plexiglass tube had an inner diameter of D_2 = 42 mm, an outer diameter of 50 mm and a thermal conductivity of 0.19 W/mK (Çengel and Ghajar, 2011). A wall thickness of 4 mm was chosen to limit the sag of the plexiglass tube over its length and to reduce heat loss to the surroundings by increasing the thermal resistance. The heating rod with its protective adhesive film had an outer diameter of D_1 = 27.2 mm, which resulted in an annular diameter ratio of $a = \frac{D_1}{D_2} = \frac{27.2}{42} = 0.648$.

An isometric view of the annular flow passage can be seen in Figure 3-4. The inlet and outlet of the annular flow passage were machined into the plexiglass tube. The inlet and outlet were manufactured from three-quarter inch threaded nylon rod with an inner diameter and D_3 of 20 mm, and were positioned vertically above the test section. Nylon bushes with different inner diameters were added to the inlet and outlet of the annular flow passage to alter the inlet size for the different test cases, as discussed in Section 3.2.4. The end supports and nylon spacers are visible in Figure 3-4. No obstructions were present for the flow in the cavity between the plexiglass tube and the heating rod.

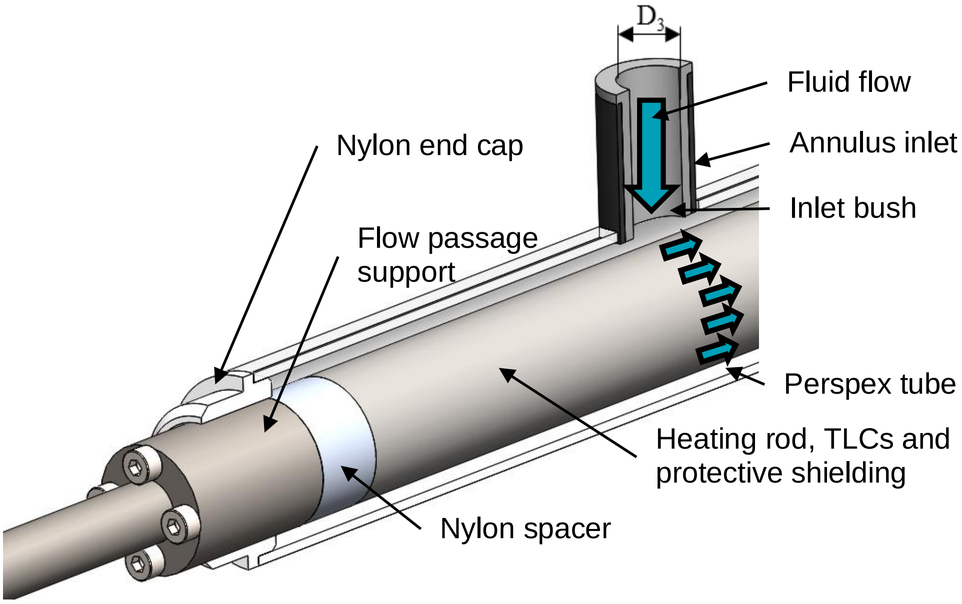

Figure 3-4: Isometric view of the annular flow passage

A schematic view of the test section is given in Figure 3-5. As seen from Figure 3-5, the test section had a wetted surface length of L_{ws} = 1 050 mm, with a centre-to-centre distance of 810 mm between the inlet and outlet of the annulus. The theoretical entry lengths for the test section under the flow cases noted in Table 3-1 is x = 148 mm for the turbulent flow cases (Çengel and Ghajar, 2011) which is well within the theoretical centre to centre distance. The wetted surface area was calculated by $A_s = \pi D_2 L_{ws}$ as 0.0897 m^2. The heating rod was secured concentrically into the plexiglass tube by end caps manufactured from nylon. These end caps were glued to the plexiglass tube to ensure a watertight seal between the heating rod and the plexiglass tube. These are also visible in Figure 3-4.

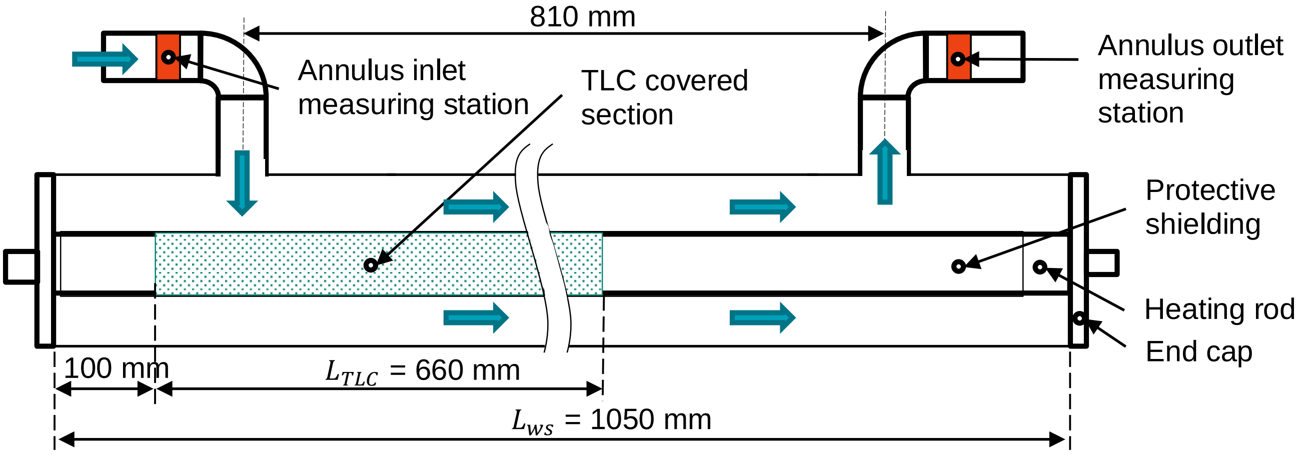

Figure 3-5: Schematic view of the test section

The bulk fluid inlet and outlet temperatures were measured by separate isothermal measuring stations. Each measuring station consisted of a short copper tube to which eight thermocouples were soldered. The thermocouples were of the T-type with a bead diameter of 0.8 mm. Eight thermocouples were installed to reduce the uncertainty of the temperature measurements and to ensure that the average bulk fluid temperature of the copper tube was recorded. The thermocouples were located around the circumference of the copper tube, approximately 45˚ apart. To limit axial heat conduction to or from these measuring stations to or from the test section, the annular flow passage was insulated from the measuring station by means of a rubber hose.

3.2.4 Inlet configurations

For this investigation, the sizes of the inlet and outlet were altered for varying Reynolds numbers. This was done to investigate the effect which different inlet configurations (sizes and on-axis and off-axis inlets) have on the heat transfer at the inlet region of the heat exchanger. There alterations in inlet size would not influence the flow rate, i.e. Reynolds number inside the annular flow passage. In total, four different inlet and outlet diameters were investigated. Note that both the inlet and outlet sizes were changed. Three on-axis inlets were tested with sizes of D_3 = 20 mm, D_3 = 15 mm, D_3 =

10 mm and one off-axis inlet with a size of D_3 = 10 mm off-centre to induce fluid swirl. The different inlet cases can be seen in Figure 3-6. The sizes of the inlet and outlet were altered by inserting nylon bushes into the standard inlet and outlet of the flow passage. This can also be seen in Figure 3-4. This meant that the outer casing of the annular flow passage did not have to be changed for the different test cases. For the induced swirl case, a nylon insert was manufactured with an inlet of D_3 = 10 mm, whereby the inlet was placed 3.5 mm off-centre from the vertical centre plane of the test section.

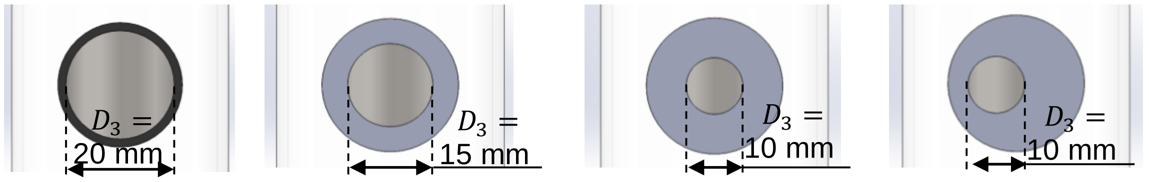

Test case A **Test case B** **Test case C** **Test case D**

Figure 3-6: Test cases with inlets of different sizes

These inlet sizes were chosen because they cover a large inlet size range so that possible trends may be confirmed. The off-axis inlet was chosen to be the same size as another inlet so that a clear comparison could be made.

3.2.5 Thermal insulation

To minimise heat losses to the environment, most of the flow passage was covered with removable elastomeric thermal insulation during tests. The thermal insulation was specified to have a thermal conductivity of 0.026 W/mK and a thickness of 18 mm.

Due to the measuring procedure employed in this investigation, a section of the flow passage had to be kept clear so that a camera could photograph the TLC surface. Thus, a section of 120 mm (at a time) could not be covered by the insulation. This resulted in 88% of the plexiglass tube being covered in thermal insulation at a given moment in time. This gap in insulation could be moved as required to map the temperature field around the circumference of the inner wall. The expected heat loss for the test range used in the study was 2%.

3.3 Imaging mechanism

An imaging mechanism was needed to capture the colour response of the TLCs. A mechanism was built to autonomously capture detailed photos of the entire TLC surface by moving a camera to all locations of the test section and the heat transfer surface in particular. These photos were stitched together to construct a complete temperature field of the inlet region of the annular flow passage. The imagining mechanism built for this study improved on the mechanism manufactured by Van der Westhuizen et al. (2014), with the focus of fully automating the mechanism to save on experimentation time and ensure accurate axial movements of the camera.

Consider Figure 3-7, which shows the imaging mechanism used to capture the thermal field of the heat transfer surface of the test section. It consisted of stationary and moving components. The stationary frame was used to position and fasten the test section in which fluid flowed from left to right (see Figure 3-7).

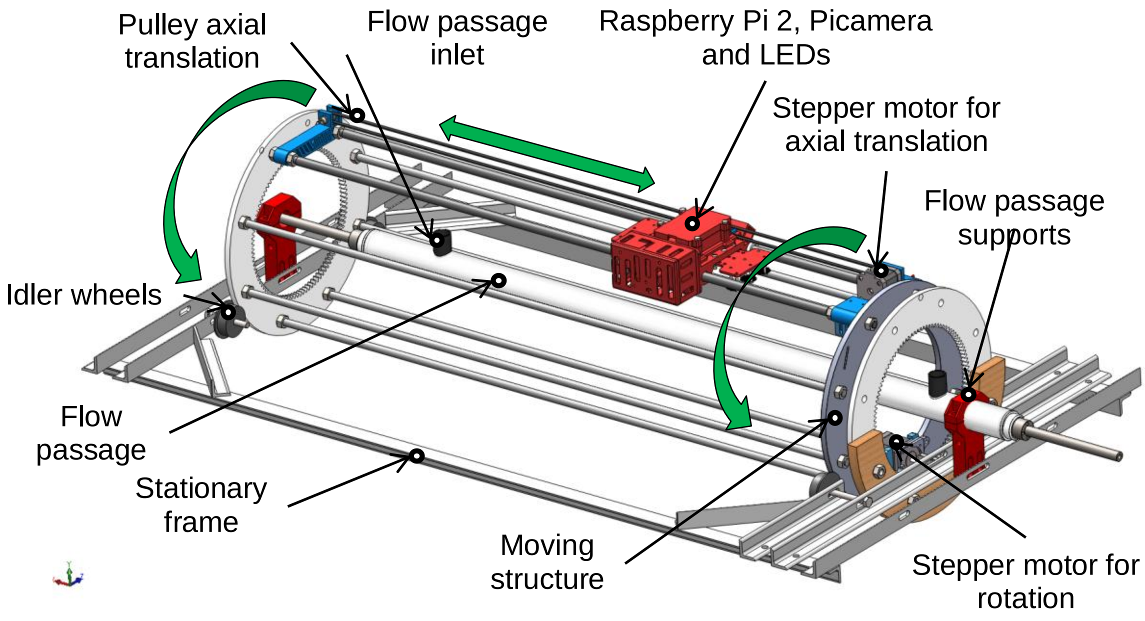

Figure 3-7: Imaging mechanism

The moving structure allowed the camera to be rotated around the test section and to be translated along the length of the test section. The moving structure was mainly manufactured from plexiglass and steel rods. The moving structure ran on idler wheels (fastened to the stationary frame), which allowed it to rotate freely about the test section. The moving structure was rotated by a stepper motor with gear and pinion assembly. The stepper motor was secured to one of the large plexiglass rings.

The camera was mounted to the steel rods. However, it could be translated along the length of the test section. An improvement to the mechanism manufactured by Van der Westhuizen et al. (2014), who carried out this translation by hand, was that the axial location of the camera was controlled by an additional stepper motor via a pulley-and-belt system. This would ensure that the camera would capture the images at the correct axial location and reduce experimentation time. The two stepper motors were controlled by a Raspberry Pi B 2 model and Pololu A4988 stepper motor controllers.

The entire system was powered by two lithium-ion batteries that were mounted to the plexiglass rings.

The images were captured by a 5- megapixel Raspberry Pi camera module. The camera module was controlled directly by the Raspberry Pi with a resolution of 2 595 x 1 944 pixels at 15 fps. The focal length of the camera was adjusted for a clear image of the TLC surface. All automatic features of the camera were switched off or fixed. This ensured that the camera did not enhance or alter the colour response of the TLC surface. These included fixing the shutter speed, analogue gain, digital gain and, International Organisation for Standardisation (ISO) value, and completely disabling any exposure modes and auto-white balances.

Light-emitting diode (LED) lights were used to illuminate the TLC surface during photography so that the lighting remained constant for all radial positions. In total, six LUXEON ES - CW200 LEDs were used. These were specified to emit light at a colour temperature of 5 500 K each at a maximum of 200 lumen.

Three LEDs were placed symmetrically on either side of the Pi camera lens (see Figure 3-8). Figure 3-8 (a) shows the bottom view of the Raspberry Pi camera and LED module, while Figure 3-8 (b) shows the side view. The LEDs were placed 85 mm away from the camera module and 170 mm apart to ensure that the reflections of the LED lighting did not protrude the region of interest of the images. The field of view (FOV), which is shown in the side view of the Pi camera, was 65˚. As seen from Figure 3-8 (b), the reflections caused by the LED lighting would be visible in the photographs. However, they were outside the region of interest of the images.

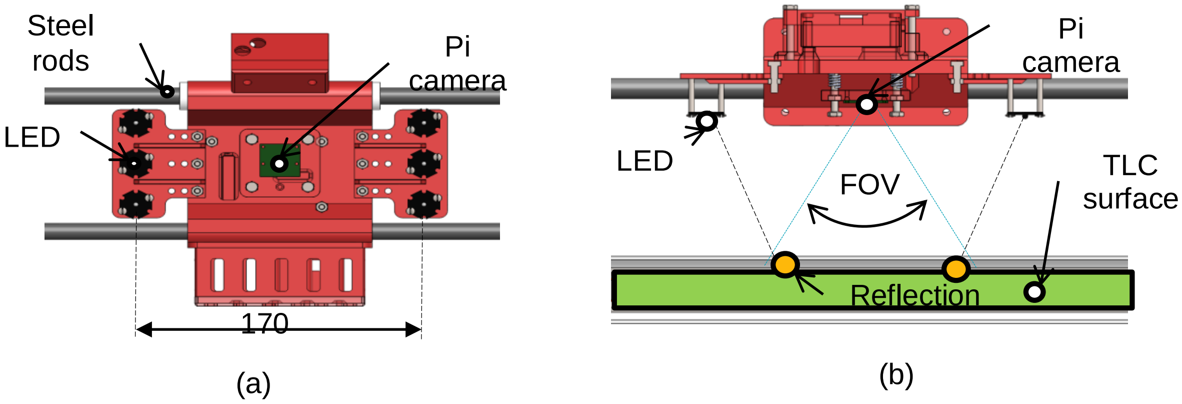

Figure 3-8: (a) Top view of Pi camera and LEDs; and (b) side view of camera and LEDs indicating LED reflections and FOV

The LEDs were powered by the lithium-ion batteries via a voltage and current regulator to ensure that the illuminance did not vary as the voltage of the batteries dropped. Matt black cardboard was fastened to the frame of the rotating structure to ensure that the background of the images remained uniform during the experiments.

A Raspberry Pi B 2 was used to control the stepper motors, camera and LED lighting. This allowed for simple and effective synchronisation between the stepper motor, LED lighting and camera. This was an improvement on the mechanism of Van der Westhuizen et al. (2014), in which the camera and motors were triggered and controlled separately. The improved mechanism was fully autonomous and required less user interaction, which could lead to experimental errors, and less time to gather the experimental data.

The torque of the stepper motors was set to match the capabilities of the 1 A motor drivers and the batteries, but it still supplied sufficient torque to correctly control the mechanism's motion. The speed of the stepper motors was set so that the systems moved smoothly without excessive vibrations. A pause period of 1.5 seconds was added at each radial stop (where a photo was taken) to allow the mechanical system to settle before the images were captured. The moving mechanism required 35 seconds to complete a revolution.

To secure the heating rod to the stationary frame, end supports were machined from steel and attached to the heating rod. A 10 mm nylon spacer was added between the end supports and heating rod to restrict heat loss to the surroundings.

3.4 Experimental procedure

This section addresses the tasks carried out to conduct the experiments. Test cases A to D were chosen to be in the low-to-turbulent flow regime, with Reynolds numbers ranging from approximately 2 000 to 7 500 at increments of 500. These exact Reynolds numbers could not be achieved, and only served as a guide for which flow rates needed to be tested.

Table 3-1 shows the different test cases for the experiments. Test case E, represents a test case that investigates the transition from laminar to turbulent flow. For this test case, experimental runs were performed with Reynolds numbers ranging from 200 to 2 000 with increments of 200 for an inlet size of D_3 = 20 mm. The Reynolds numbers shown in Table 3-1 are the actual flow rates achieved for the experiments.

Table 3-1: Experimental test cases

Test case symbol	A	B	C	D	E
Inlet/outlet size	D3 = 20 mm	D3 = 15 mm	D3 = 10 mm	D3 = 10 mm OC	D3 = 20 mm
Re achieved	2 041	2 033	2 051	2 055	2 026
	2 561	2 543	2 562	2 570	1 839
	3 079	3 053	3 072	3 085	1 624
	3 604	3 534	3 587	3 596	1 423
	4 122	4 042	4 097	4 109	1 221
	4 649	4 575	4 609	4 624	1 022
	5 129	5 057	5 121	5 136	820
	5 640	5 594	5 633	5 651	610
	6 167	6 103	6 141	6 161	410
	6 681	6 607	6 653	6 676	205
	7 200	7 117	7 157	7 188	-
	7 728	7 624	7 576	7 602	-

All testing was conducted in a small above-ground laboratory at the University of Pretoria. Testing during daytime is not ideal because the position of the sun changes during the day and with the seasons, thus testing with sunlight would result in different incident lighting angles, which affect the reflected colours of the TLC surface. It has been found that colour response of a TLC surface is very sensitive to changes in lighting angles and viewing angles (Rao and Xu, 2012). This, together with other factors, such as changes in cloud cover, would change the experiment's lighting conditions. This could lead to invalid results. Therefore, all tests were performed at night to limit the impact on the photography.

During the tests, all lights in the labs were switched off with only the LED lighting on the setup itself emitting light for the camera. Another reason for testing at night is that the TLCs are sensitive to ultraviolet (UV) light, which breaks down thermochromic crystals and alters their colour response with temperature (Hallcrest, 2014b). Prolonged UV light exposure would require regular recalibration. To protect the TLCs from UV light in the laboratory, the entire test setup was covered with a large protective sheet and the flow passage was covered with additional insulation.

The thermocouples and TLC surface were calibrated before the experimental test was conducted. The procedure in which the thermocouples and TLC surface was calibrated is discussed in Sections 4.2.2 and 4.1.

Figure 3-9 outlines the testing procedure that was followed during the experiments. The experiments were broken down into three major sections: start-up, test case data collection and shut down.

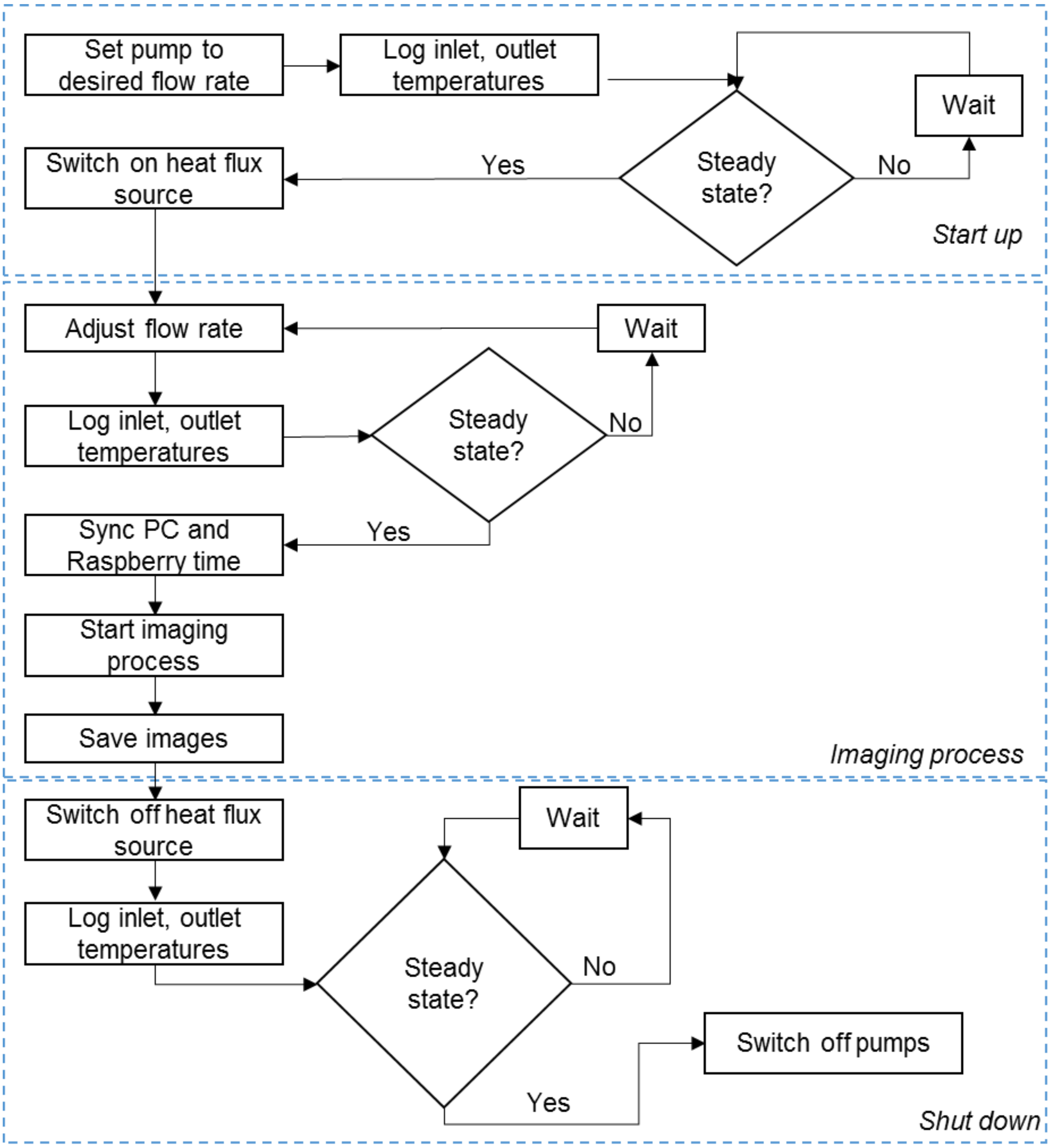

Figure 3-9: Experimental methodology

During start-up, the circulation pumps and chiller were switched on so that the water in the 1 000-litre reservoir (reference to Figure 3-1) reached a temperature of 21 ˚C, ±0.5 ˚C. Once achieved, the positive displacement pump was switched on and the inlet and outlet temperatures of the flow passage were recorded. For these experiments, steady state was set to be achieved once the difference between the inlet and outlet temperatures did not fluctuate more than 0.1 ˚C over a period of eight minutes, after which it was concluded that the initial steady state had been achieved.

For test case data collection, the flow rate was set to the required value and the power supply to the predetermined current and voltage values. For these tests, the power to the heating rod was set to 400 W, which equated to 4 917 W/m^2. This power rating was selected as the TLC reached the upper end of the active bandwidth for flow rates at the lower end of the Reynolds numbers range that was considered in this study. Once steady state had been achieved (once the temperature difference between the inlet and outlet measuring stations did not fluctuate by more than 0.1 ˚C for a period of five minutes) with the power supply on, the data collection process could commence. For this, the time on the Raspberry Pi and the data-logging computer was synchronised. The Raspberry Pi was set up to take all the pictures around the heat exchanger surface. The temperatures of the inlet and outlet measuring stations were recorded.

The imaging process started by switching on the LED lighting. The camera took eight equiangular images per revolution around the test section, each at a 45˚ circumferential interval from one another (more information on this will be supplied in Section 4.2.3). This was accomplished by engaging the stepper motor to rotate the cage around the radial position, stopping, taking a photo and continuing to the next radial position. Once all images had been taken around the circumference, the stepper motor would move the camera either 10 mm or 20 mm (depending on the location along the flow passage) to its new axial location. Once the camera was at a new axial location, a halt of five seconds was added so that the insulation could be adjusted on the heat exchanger for a clear view of the heating rod. This process continued until all the images had been taken. All images and inlet and outlet temperatures were saved.

For the shutdown procedure, the constant heat flux source was switched off and allowed to cool while water was still flowing over the surface. The pumps were switched off and water was drained from the annulus.

3.5 Summary of the experimental setup

This chapter described the experimental setup and facility used in this investigation. A cold-water flow loop was used to circulate water through the test section’s annulus. The inner surface of the annulus was heated by means of a heating rod that supplied uniform heat flux to the water. The outer surface of the heating element was treated with TLCs so that the surface temperature could be determined. Flow rates and inlet and outlet temperature readings would be logged by a National Instrument setup that was connected to a computer. An imagery mechanism was manufactured to capture the colour response of the TLCs. The mechanism was fully automated. The camera was rotated and moved along the length of the heat exchanger. The outer tube of the annulus was manufactured from plexiglass and the size of the inlet and outlet could be altered for the different test cases.

4. Data analysis

This chapter covers the methodology that was followed to calculate the local and overall heat transfer coefficients from the raw experimental results. Thermocouple calibration for the inlet and outlet measuring stations is also discussed. The calibration of the TLC surface with respect to colour and temperature, and the extraction of the wall temperatures from the TLC surface is covered in detail. The method to determine and account for the thermal resistance of the protective adhesive layer to protect the TLCs is described, together with how the uncertainties of the experimental results were calculated.

4.1 Thermocouple calibration

Thermocouples were used to measure the inlet and outlet bulk water temperatures, as well as the ambient air temperature. The procedure employed to calibrate the thermocouples is discussed in this section.

In total, 17 thermocouples were used in this study. Eight were used at the inlet measuring station, eight at the outlet measuring station and one to measure the ambient air temperature. All thermocouple tips were manufactured from scratch for this investigation. The thermocouples at the inlet and outlet were soldered to their measuring stations (copper tube) before calibration.

Calibration was performed by using a Lauda Proline thermal bath and a PT100 calibrated to 0.1 ˚C. The thermal bath was also calibrated to 0.1 ˚C, but had a temperature display indicating the temperature up to two decimal places. This ensured that an isothermal temperature reading up to 0.01 ˚C was reached, which was accurate to 0.1 ˚C.

The thermocouples were calibrated for temperatures from 16 ˚C to 26 ˚C at increments of 2 ˚C, to cover for a range larger than anticipated in the investigation. For calibration, the water in the thermal bath was first heated to 26 ˚C. Temperature readings from the thermocouples were only logged once the temperature of the PT100 did not vary by more than 0.1 ˚C and the temperature of the thermal bath by 0.01 ˚C for two minutes. The corresponding PT100 temperature was recorded for 600 thermocouple readings over a period of one minute. The water was cooled to 16 ˚C at increments of 2 ˚C. Once 16 ˚C was reached, the water was heated to 26 ˚C at increments of 2 ˚C, with PT100 and thermocouple readings taken at every 2 ˚C. This was done to calibrate the thermocouples for both a heating and cooling cycle. The thermocouples were calibrated at 12 isothermal temperatures.

A calibration curve, as seen in Figure 4-1, was created for each thermocouple by plotting the average measured temperature against the corresponding PT100 temperature for each isothermal temperature state. A linear curve fit was added to determine the calibration coefficients m and c of each thermocouple as seen in Equation 31. The calibrated temperatures were determined with Equation 31, where T_{cal} was the calibrated thermocouple reading, m the calibration gradient, T_{uncal} the uncalibrated thermocouple reading and c a calibration constant.

$$T_{cal} = m * T_{uncal} + c \tag{31}$$

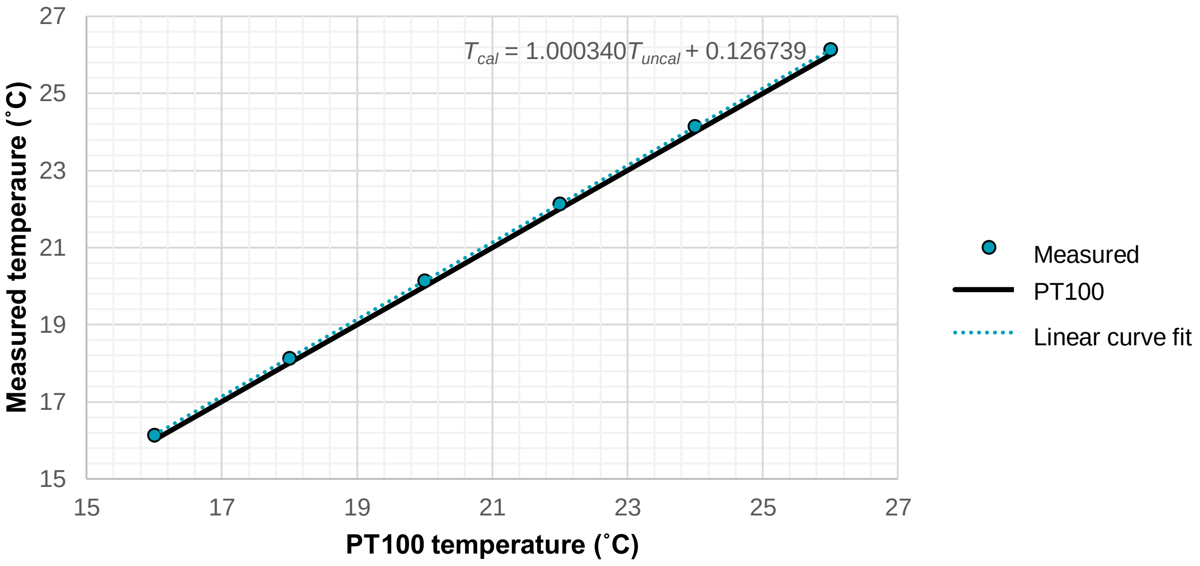

Figure 4-1: Temperature profile of the thermocouple before calibration

The thermocouple error before and after calibration was also considered to see the improvement after calibration. The error was considered to be the difference between the uncalibrated or calibrated thermocouple readings against the PT100 temperature readings. A typical thermocouple error graph can be seen in Figure 4-2. As seen from Figure 4-2, after calibration, the thermocouple error was drastically reduced from an error of -0.14˚C to one of ±0.01˚C. The error before and after calibration was considered for all thermocouples and can be seen in Appendix B.

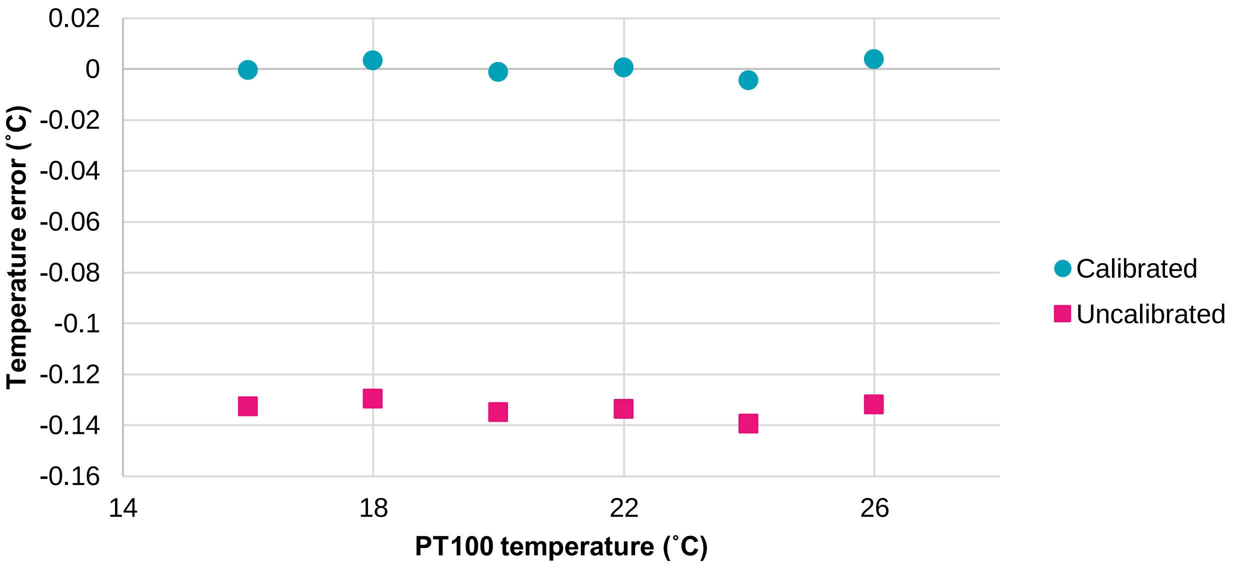

Figure 4-2: Thermocouple error before and after calibration

4.2 Thermochromic liquid crystals

This section covers all aspects regarding extracting temperatures from the TLC surface.

4.2.1 Interpretation of thermochromic liquid crystals

As mentioned, LCT is a visual technique to measure temperature, which uses TLCs. TLCs react to changes in temperature by changing colour.

Colours can be specified or described using different models, each suited to different applications. The models make use of a coordinate system, in which a point is used to specify a colour. Familiar colour models include red, green, blue (RGB), cyan, magenta, yellow (CMY) and hue, saturation, intensity (HSI).

In the RGB colour model, a Cartesian coordinate system is used, whereby each axis represents a primary colour. The RGB model is primarily used for colour monitors and video cameras (Stasiek et al., 2014).

The HSI colour model makes use of a cylindrical coordinate system to represent a point on the RGB colour model. The hue of a colour is used to specify the dominant wavelength of a pure colour and is determined by the angle between the orthogonal components of the RGB colour model (Smith et al., 2001). The hue values vary from 0° to 360°, where 0° and 360° refer to pure red, 120° to pure green and 240° to pure blue. Hue values may be normalised to a value between 0 and 1. The saturation refers to the degree by which a hue has been mixed with white light, and the intensity specifies the brightness of the light.

A conversion technique may be applied to convert colours from the RGB model to the HSI model. The HSI model is favoured for TLC studies, as the hue exhibits a monotonic relation to temperature. This allows researchers to analyse temperatures with high precision, while reducing sources of uncertainty (Smith et al., 2001). The hue value is no longer a function of brightness when the HSI colour model is implemented. This reduces the influence that changes in surrounding brightness may have on the experimental results.

There are a number of techniques to calculate the hue value from the RGB colour model. Conditional algorithms exist, which can carry out the conversion. However, researchers often make use of closed-form arc tangent formulations to calculate the hue values (Smith et al., 2001). Computer programs, such as Matlab, have built-in functions, such as *RBG2HSV,* to convert the RBG to hue, saturation, value (HSV), where the algorithm shown in Equation 32 is used to calculate the normalised hue value.

$$H = \begin{cases} \dfrac{G - B}{6(R - \min(R, G, B))} & if\ R = Max \\ \dfrac{2 + B - R}{6(G - \min(R, G, B))} & if\ G = Max \\ \dfrac{4 + R - G}{6(B - \min(R, G, B))} & if\ B = Max \end{cases} \tag{32}$$

For this investigation, the algorithm noted in Equation 32 was used in Matlab to convert colours from the RGB colour model to a normalised hue value.

4.2.2 TLC calibration

During the early stages of TLC research, the temperature response of a TLC surface was visually scrutinised. However, to increase the value and accuracy of heat transfer studies, image-processing techniques were employed (Camci, 1996).

The hue-to-temperature relationship of the TLC surface needs to be known before accurate temperature estimations can be made. Thus, a calibration process, where the hue values are captured at known temperatures, is performed. The colour response of TLC mixtures will vary due to differences in the batches and differences in applications with regard to camera angles, diffraction effects and different lighting conditions. Thus, a unique calibration is required for each experimental setup. Factors such as lighting angles and camera positions need to be kept constant during calibration and experimentation.

TLCs are anisotropic in nature, meaning that they exhibit different physical properties when viewed from different angles. Thus, consistent lighting and viewing angles are critical to ensure accurate temperature relations (Smith et al., 2001). A perpendicular on-axis view is not possible on all surfaces; therefore, good calibrations are vital in reducing the uncertainty associated with off-axis viewing and lighting arrangements. Localised TLC calibrations are encouraged for uneven surfaces.

The TLC calibration was conducted 240 mm away from the inlet, as this section of the TLC surface best represented the average hue value of the TLC surface for the entire temperature bandwidth considered. This was determined by considering the hue values of the entire TLC surface along the axial length for six isothermal temperatures.

It was noted that the hue-to-temperature response remained relatively constant along the length of the heat transfer surface of the test section, with a maximum variation in hue of 0.01, which corresponded to 0.15 ˚C. However, variations were noted around the circumference (radial positions). These, however, remained relatively constant along the axial length of the TLC surface. These variations were attributed to factors such as diffraction by the plexiglass tube or the photography mechanism. Thus, localised calibrations were performed for each radial position (eight in total and 45˚ apart) from which the images were taken during the experimental runs. Each radial position would thus have a unique calibration between temperature and reflected hue value.

Variations in the hue-to-temperature relation around the circumference may be attributed to a number of factors. The heating rod was placed in the annular flow region as concentrically as practically possible. It could, however, not be guaranteed that the distance between the plexiglass and TLC surface was the same for the entire flow passage. Variations in the distance between the heating rod and perspex tube would have had an influence on the diffraction angles for the imaging mechanism. The heating rod was also placed in the stationary frame of the imaging mechanism so that the heating rod would be concentric within the rotating structure. Variation in distance between the camera and TLC surface (±2 mm) may have also have contributed to the variations in hue around the circumference. Thus, two separate calibration curves were developed for each radial position.

As this investigation focused on heat transfer at the inlet region of an annular flow passage, more data points were collected at the inlet region than were compared to the region at which fully developed flow was anticipated. Sample areas (discussed in more detail in Section 4.2.3) would be extracted from the TLC photographs that would be stitched together to construct the entire temperature field. This meant that the TLC sample area considered for extraction at the inlet was smaller compared to the one for the fully developed flow “region”. Thus, two calibration curves were developed, one for the smaller and one for the larger sample areas. Thus, two calibrations were conducted for each radial position, which resulted in 16 calibration curves.

The calibration process was carried out by circulating water from a Lauda Proline thermal bath through the annuals of the annular flow passage. The thermal bath was set to circulate water at specific temperatures, which were within the bandwidth of the TLCs, through the flow passage. This ensured an isothermal annular flow passage for the calibration. The temperature of the water in the thermal bath and of the annular flow passage were monitored by the calibrated inlet and outlet measuring stations and a PT100 (uncertainty of 0.1 ˚C) placed inside the thermal bath.

The calibration process entailed setting the thermal bath to achieve a temperature within the range of 21.56 ˚C to 32.02 ˚C and allowing it to circulate though the flow passage. This temperature range was considered because it was found that TLCs only had a monotonic relationship in this range. Time was given for the test section to reach the isothermal temperature set on the thermal bath. The temperature of the test section was considered by analysing the temperature difference between the inlet and outlet measuring stations and the temperature reading of the PT100. An isothermal temperature was said to be achieved once the PT100 reached the desired temperature accurate to 0.1 ˚C and the temperature between the inlet and outlet measuring stations did not vary by more than 0.1 ˚C for five minutes. Once the system had reached this steady-state temperature, the temperature of the PT100 was noted, and photos were taken at the eight radial locations around the circumference of the annular flow passage at 240 mm from the inlet. The normalised hue value was extracted from the sample area (considered and discussed in Section 4.2.3) of these photos and calculated using Equation 32.

A calibration curve was developed by plotting the normalised hue value against its associated PT100 temperature. A typical calibration curve can be seen in Figure 4-3. For the calibration process, the hue value was captured at 52 independent temperatures. This was done to improve the accuracy of the calibration. Before and after all experiments had been completed, it was ensured that the hue-to-temperature behaviour did not change during the course of experimentation. As seen from Figure 4-3, the relationship between hue and temperature did not change during the course of the experimentation process and thus no recalibration was required.

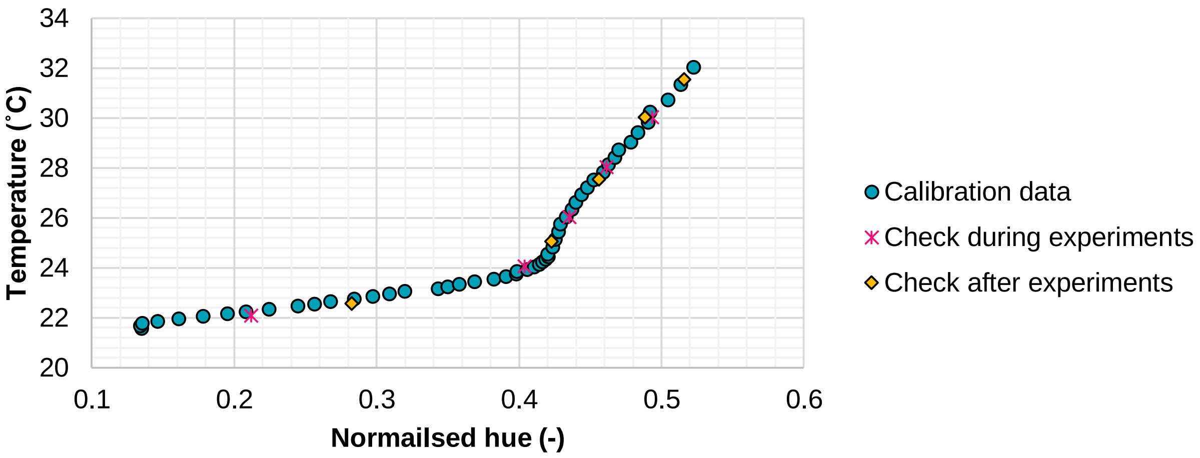

Figure 4-3: Calibration curve with spot checks before and after experiments

It was found that that the hue-to-temperature relation was not monotonic at the lower and upper ends of the manufacturer's specified bandwidth. Thus, the calibration curve was only set up for the values for the monotonic hue-to-temperature range. The monotonic range was 21.56 ˚C to 32.02 ˚C. Selecting the experimentation region within this monotonic range would eliminate the hysteresis effects noted by Sabatino et al. (2000) and Smith et al. (2001). These effects induced different behaviours during the cooling and heating cycles that prevailed when the TLCs were heated above and below their bandwidths.

As seen from Figure 4-3, the hue-temperature calibration exhibits two definite gradients. The lower region of the calibration curve exhibits a gentle slope, whereas the upper region of the curve exhibits a steeper slope. Two separate polynomials for the hue-to-temperature calibration were developed due to the difference in the slopes. Figure 4-4 shows the two separate calibration relations for the TLCs at a specific radial location. For the lower portion of the calibration curve, a sixth-order polynomial was developed to define the hue-temperature relationship, whereas for the upper region, a fifth-order relation was developed. These polynomials were chosen because they reduced the maximum error between the actual temperature (PT100) and the temperature as calculated with the developed polynomial. These polynomials were generated by a numerical solver.

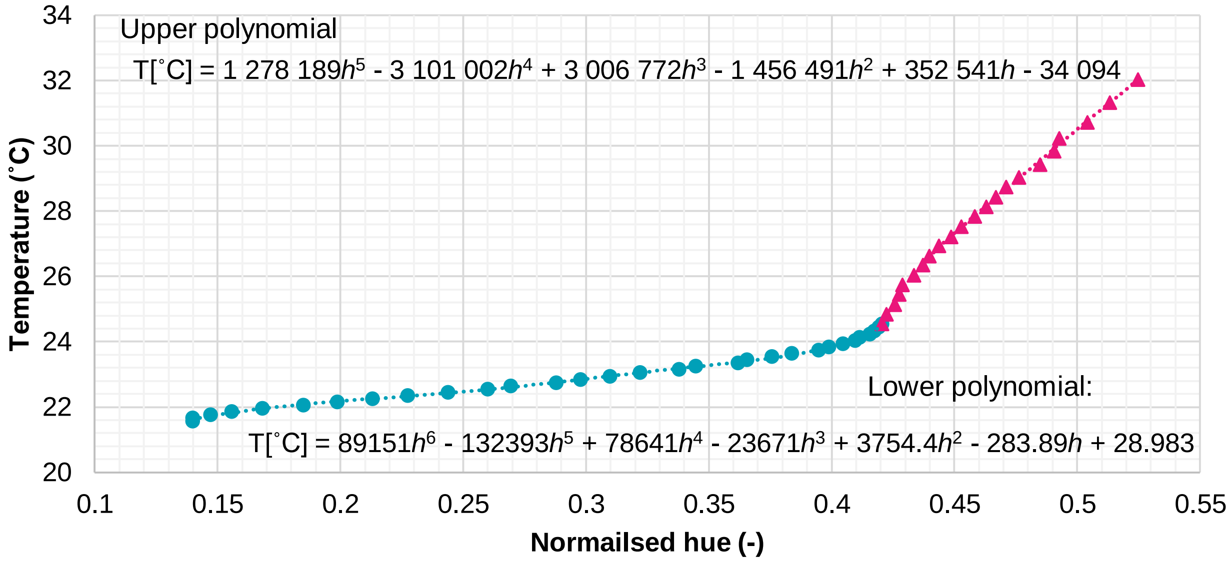

Figure 4-4: Hue-to-temperature calibrations with calibration polynomials

By making use of the developed polynomials, the temperatures corresponding to a specific hue value could be obtained. The largest absolute error between the PT100 temperature and the estimated temperature from the hue value was 0.236 ˚C, which was present at the upper end of the TLC active bandwidth. The average error was 0.036 ˚C, the average standard deviation was 0.037 ˚C and the maximum standard deviation was 0.047 ˚C. As suggested by Rao and Zang (2010) and (Rao and Xu, 2012), a value between 0.4 ˚C and 0.5 ˚C may be assumed for the uncertainty for one TLC pixel, which exceeded the value of 0.236 ˚C found for this investigation.

4.2.3 Sampling area and interpretation of hue values from the TLC photographs

The wall temperatures of the heating rod were determined by extracting the hue value of the TLCs and applying the TLC calibration polynomials to convert the hue values to temperature. Before the conversion from hue to temperature could be made, the size of the sample area extracted from the photographs (TLC surface) had to be determined. The entire heating rod surface area could not be extracted, as the TLCs are sensitive to changes in viewing and lighting angles.

A typical photograph from the experiment can be seen in Figure 4-5. In Figure 4-5, the heating rod treated with the TLCs (turquoise in this figure) is in the centre of the image and extends horizontally. The plexiglass tube that formed the annulus can also be seen extending from the edges of the TLC surface. The reflections seen on the outer edges of the plexiglass tube were caused by the LED lighting. Four reflections can be seen in the outer edges of the tube and two on the centre of the heating rod, which cannot easily be seen in this photograph.

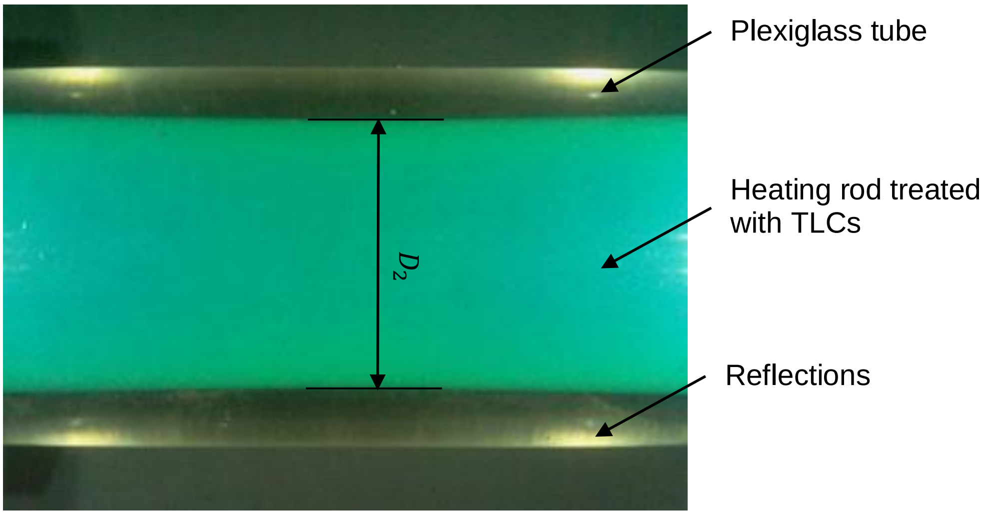

Figure 4-5: Typical photograph from the experiment

The area of interest or sample area, which would be extracted from the photographs of the experiment, had to be determined. Due to the sensitivity of the viewing and lighting angles of the TLCs, the size of the sample area was restricted. The larger the sample area, the larger the viewing angle span per image, which meant that the extracted hue and temperatures from the photographs would not be accurate representations of their true values. Small sample areas would be favoured, but these areas would increase the time required to photograph the entire TLC surface. This was not desirable because the annulus inlet water temperature tended to drift over time and it was important to keep the time lapse during test runs as short as possible. Thus, an investigation was performed to determine the optimal sample area or area of interest for this investigation.

For this, a reference rod was manufactured onto which a cylindrical coordinate system was drawn. The reference rod had the same dimensions as the actual heating rod. The reference rod was placed into the plexiglass tube and the annulus was filled with water. Photographs were taken of the reference rod and analysed. The reference rod was used to estimate the size of the sample areas and to get an indication of the number of pixels per unit length. This was done to account for the refraction caused by the plexiglass tube.

In the study by Van der Westhuizen et al. (2014), the optimal number of photographs taken around the circumference of the tube was considered. Investigations were performed for 40, 20, and 10 photographs around the circumference. It was found that the number of photographs around the circumference does not have a major influence on the captured hue values, i.e. temperature readings. If calibrated correctly, which means that calibration was performed for a number photographs around the circumference, the derived temperatures were close to the actual ones. The benefit of fewer photographs around the circumference means that less time is required for the tests.

For this study, it was considered to only use eight photographs around the circumference instead of the 10 Van der Westhuizen et al. (2014) used. The variation in temperature of a sample area for 10 photographs around the circumference was compared to the variation in temperature of a sample area if eight photographs were taken around the circumference. For the sample area of 10 circumferential stops, the maximum hue variation for the selected sample area was 0.0022, which equated to 0.11 ˚C. This variation was calculated by considering the highest and lowest hue value of all pixels in the sample area. For the sample area with eight rotational stops around the circumference, the maximum hue variation was 0.0025, which equated to 0.12 ˚C. The difference between the eight and 10 rotational stops was only 0.01 ˚C, which was considered to be insignificant. Thus, eight photographs were considered around the circumference for this investigation (see Figure 4-6), with each photograph taken 45˚ apart. This resulted in an arc length of 10.6 mm for each photograph.

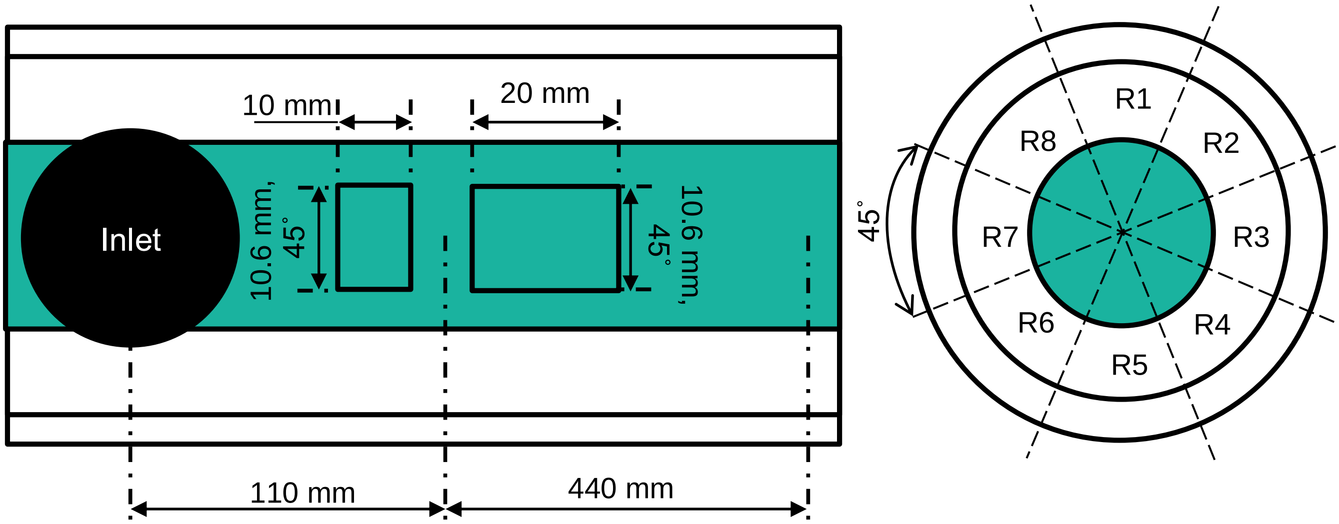

Figure 4-6: Sample areas considered

The axial length of the sample area was selected by considering the variation in hue about the length of the TLC surface. An investigation was performed to determine how the hue value varied along the axial length of the heating rod. For a sample length of 40 mm, the variation in hue was 0.012. This equated to a temperature variation of 0.77 ˚C. The variation in hue for a 20 mm sample area was 0.002, which was equivalent to 0.13 ˚C, while a 10 mm sample area was equivalent to 0.067 ˚C.

As mentioned earlier, a large number of data points were needed at the inlet region to capture the effect of the developed boundary layer. Less-populated results were required in the more thermally developed region. Thus, two different sample area sizes were considered. A small sample area was extracted for the inlet region and a larger one for further down the tube. The sample lengths considered were 20 mm and 10 mm. In total, 11 sample areas with a sample length of 10 mm would be captured and a further 22 with a sample length of 20 mm. As seen in Figure 4-6, the first 110 mm of the heat transfer surface, measured from the centre line of the inlet, was investigated with a sample area of 10 mm x 10.6 mm (arc length or 45˚) and the remaining 440 mm with a sample area of 20 mm x 10.6 mm (arc length or 45˚).

Once the sample area was identified from each image, it was cropped and processed. The cropped images were grainy when the TLC was viewed at a pixel level. This could have been caused by a number of factors, such as dirt or dust on the plexiglass tube or heating rod surface, an irregular (non-smooth) heating rod surface that caused shadows, the quality of the imaging equipment, non-uniform TLC application or dust in the atmosphere.

When the TLC surface was considered on a pixel level, the grainy surface meant that temperature differences of up to 0.05˚C were present between neighbouring pixels. As it is not possible for such large temperature difference to exist between pixels, a decision was made to consider the average hue value for the entire sample area. This would lower the resolution of the results, but would act as a filter to smooth out the wall temperature distributions.

4.2.4 Temperature extraction from TLC photographs

The procedure carried out to extract the temperatures from the TLC sample areas is discussed in this section. A computer script was developed to locate the sample area of each photograph, crop the sample area, and determine the average hue value. The average hue value was converted to a temperature reading after which all temperature readings were stitched together to form the resulting temperature field of the flow passage.

From the experiments, the photographs were grouped together for the different test cases. The images were named such that their title indicated the position (axial and radial location) where the image was taken. The images from the experiment, as seen in Figure 4-5, were 2592 x 1944 pixels in size. Each test case contained 264 images, for which there were 8 images about the circumference for the 33 images along the axis.

The computerised script ran as follows: each image was loaded into a loop in the script. For the sample area to be identified, the outer edges of the heating rod needed to be located. For this, the average horizontal red, average horizontal green and average horizontal blue colours values were considered. Spikes were present at the outer edges of the heating rod due to the vibrant colour of the TLCs. These colour spikes were used to determine the location of the heating rod.

Once the outer edges of the heating rod were located, two checks were run to ensure that the heating rod was located correctly. The typical diameter of the heating rod diameter in pixels was determined and compared to the number of pixels for the heating rod located by the script. If the heating rod diameters varied by more than 5%, the computer script prompted the user to manually locate the outer edges of the heating rod. The other test would compare the location of the upper and lower edge of the heating rod to approximated values. This would ensure that the correct colour spikes were identified. If this test also failed, the user was again prompted to manually locate the outer edge of the heating rod.

Once the outer edges of the heating rod were located, the sample area was identified on the TLC surface. This was done with basic trigonometry and adding a correction factor introduced by the refraction of the water in the annulus and plexiglass tube. The correction factor was determined by using the reference rod with a cylindrical coordinate system, as discussed in Section 4.2.3. The location of the sample area was drawn on the image and the sample area cropped for further processing. Figure 4-7 (a) shows the image of the heating rod, with the sample area indicated with the red positional lines. Once all sample areas had been located, a manual test was carried out, whereby all sample areas were checked with their respective positional lines, as in Figure 4-7 (a). Figure 4-7 (b) is a typical cropped sample area that was extracted for further analysis. The cropped sample areas were named accordingly to retain the information of where the image was taken. The cropped sample area contained 226 800 pixels on average for the larger sample area and 113 400 for the smaller sample area.

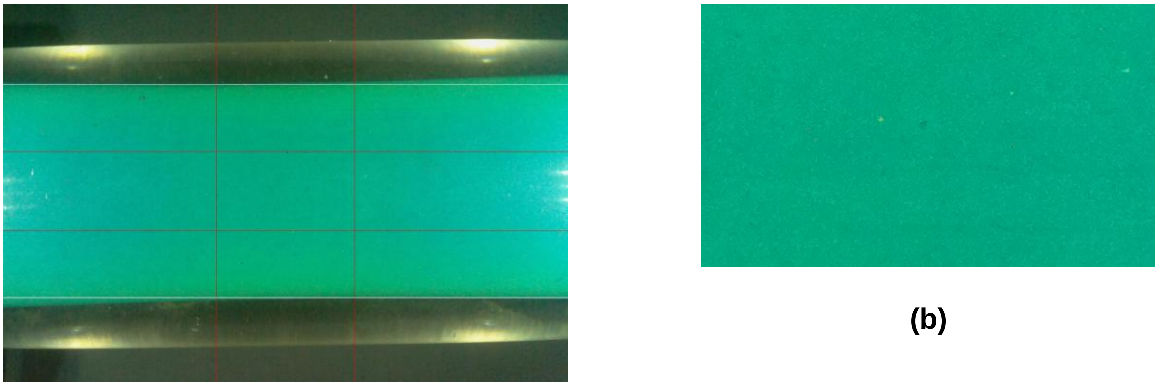

(b)

(a)

Figure 4-7: Processed experimental images: (a) with indications of heating rod and sample area; and (b) extracted sample area

The cropped images were loaded and the average hue value was computed for the entire area. The calibration polynomials developed during the TLC calibration were applied to the cropped images. Note that the correct TLC calibration polynomials had to be loaded for each image by considering the radial position of the image, as discussed in Section 4.2.2. Each cropped image now resembled a temperature. The temperatures of all cropped images were saved into a matrix to represent the entire temperature field.

A typical temperature field of the heating rod can be seen in Figure 4-8. The temperature field is considered here as a flat surface that represents the circular shape of a cylinder. The vertical axis represents the radial position and the horizontal axis the axial location of where the image was taken. This temperature field is for the test case of $\mathrm{Re} = 2000$, $\dot{q} = 4\ 700$ W/m^2 (test case A). The smaller and larger sample areas can be clearly seen in Figure 4-8, where smaller sample areas were used in the inlet region. A colour scale was added to easily visualise the resulting temperature field, with red indicating the warmer temperatures. These temperature fields were later used to determine the heat transfer coefficients for the test cases.

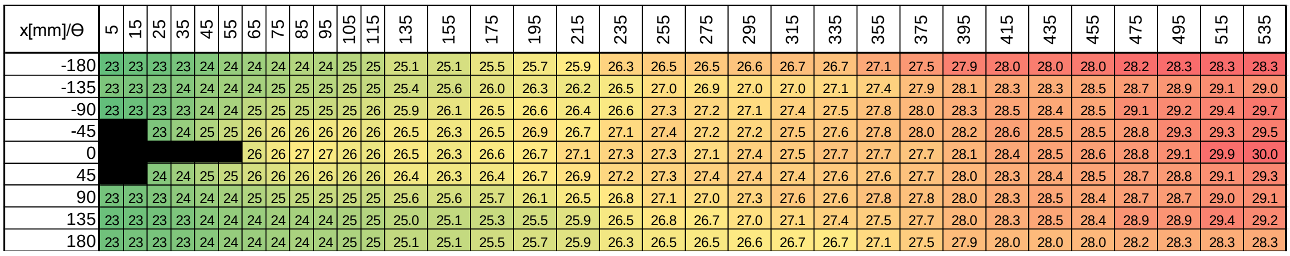

x[mm]/Θ	5	15	25	35	45	55	65	75	85	95	105	115	135	155	175	195	215	235	255	275	295	315	335	355	375	395	415	435	455	475	495	515	535
-180	23	23	23	23	24	24	24	24	24	24	25	25	25.1	25.1	25.5	25.7	25.9	26.3	26.5	26.5	26.6	26.7	26.7	27.1	27.5	27.9	28.0	28.0	28.0	28.2	28.3	28.3	28.3
-135	23	23	23	24	24	24	24	25	25	25	25	25	25.4	25.6	26.0	26.3	26.2	26.5	27.0	26.9	27.0	27.0	27.1	27.4	27.9	28.1	28.3	28.3	28.5	28.7	28.9	29.1	29.0
-90	23	23	23	23	24	24	25	25	25	25	25	26	25.9	26.1	26.5	26.6	26.4	26.6	27.3	27.2	27.1	27.4	27.5	27.8	28.0	28.3	28.5	28.4	28.5	29.1	29.2	29.4	29.7
-45			23	24	25	25	26	26	26	26	26	26	26.5	26.3	26.5	26.9	26.7	27.1	27.4	27.2	27.2	27.5	27.6	27.8	28.0	28.2	28.6	28.5	28.5	28.8	29.3	29.3	29.5
0							26	26	27	27	26	26	26.5	26.3	26.6	26.7	27.1	27.3	27.3	27.1	27.4	27.5	27.7	27.7	27.7	28.1	28.4	28.5	28.6	28.8	29.1	29.9	30.0
45			24	24	25	25	26	26	26	26	26	26	26.4	26.3	26.4	26.7	26.9	27.2	27.3	27.4	27.4	27.4	27.6	27.6	27.7	28.0	28.3	28.4	28.5	28.7	28.8	29.1	29.3
90	23	23	23	24	24	24	25	25	25	25	25	25	25.6	25.6	25.7	26.1	26.5	26.8	27.1	27.0	27.3	27.6	27.6	27.8	27.8	28.0	28.3	28.5	28.4	28.7	28.7	29.0	29.1
135	23	23	23	23	24	24	24	24	24	24	25	25	25.0	25.1	25.3	25.5	25.9	26.5	26.8	26.7	27.0	27.1	27.4	27.5	27.7	28.0	28.3	28.5	28.4	28.9	28.9	29.4	29.2
180	23	23	23	23	24	24	24	24	24	24	25	25	25.1	25.1	25.5	25.7	25.9	26.3	26.5	26.5	26.6	26.7	26.7	27.1	27.5	27.9	28.0	28.0	28.0	28.2	28.3	28.3	28.3

Figure 4-8: Temperature field of wall ($\mathbf{Re} = 2000$, $\dot{\mathrm{q}} = 4\ 700$ W/m^2, test case A)

For this investigation, the images in the proximity of the inlet could not be used as the inlet of the annulus either blocked the view or cast shadows over the TLC region being investigated. Thus, the affected images were no longer considered.

4.3 Heat transfer rate

As mentioned, a direct-current (DC) power supply was used to power the heating wire inside the heating rod. The rate at which the power was transferred or dissipated, $\dot{Q}_{elec}$, may be described by Equation 33.

$$\dot{Q}_{elec} = IV \tag{33}$$

The quantities of V and I refer to the voltage and current supplied to the rod that was indicated on the display of the power supply. The heat generated by the heating rod heated the water in the annular flow passage. The rate at which heat was transferred to the annular flow passage, $\dot{Q}_a$, may be described by Equation 34.

$$\dot{Q}_a = \dot{m}C_p(T_{bout} - T_{bin}) \tag{34}$$

For this heat transfer rate equation, the value of $\dot{m}$ refers to the mass flux of the water flowing through the annulus, which was measured by a Coriolis flow rate meter. The value of C_p refers to the specific heat capacity of the water and was calculated by the equations proposed by Popiel and Wojtkowiak (1998), calculated at the mean temperature between the inlet and outlet measuring stations. The value of T_{bout} and T_{bin} refers to the arithmetic average of the eight inlet and eight outlet thermocouples that are mounted on the temperature-measuring stations.

4.4 Energy balance

The energy balance was calculated to determine how well the setup was insulated against heat losses or gains to the environment. Lower energy losses equate to more accurate and reliable experimental results.

The energy balance (eb) was calculated by comparing the amount of heat transferred to the test section (by the DC power supply) to the amount of heat absorbed by the water flowing in the annulus. This energy balance is calculated as a percentage with the formula shown in Equation 35, where smaller energy balances are favoured.

$$eb = \frac{\dot{Q}_{elec} - (\dot{Q}_a + (\dot{Q}_{loss})}{(\dot{Q}_{elec} + \dot{Q}_a)/2} * 100 \qquad (35)$$

An energy balance of 0% can only be achieved theoretically. For an energy balance of 0%, all heat emitted by the heating rod should be transferred to the water in the annular passage and no heat may be gained or lost to the environment. It is difficult to achieve an energy balance of 0% for experiments, as heat is either gained or lost to the environment.

It is possible to account for some heat losses to and from the environment. For this investigation, the major heat losses or gains were accounted for by a mathematical first-order approach. The major heat losses were identified as follows:

- Heat loss through the plexiglass tube and insulation
- Heat loss through the plexiglass tube without insulation
- Heat loss though the end supports

For all the experiments, the maximum and minimum amounts of heat losses or gains accounted for equated to 4.01 W and 0.31 W. The largest energy balance value was found to be 2.56% after all losses or gains had been accounted for. The manner in which the heat losses or gains were accounted for are discussed in the following sections.

4.4.1 Heat loss through the plexiglass tube and insulation

Heat was gained or lost through the plexiglass tube and insulation if there was a temperature difference between the bulk fluid and the ambient air. In this case, the thermal resistive network was a series network comprising the following resistances:

- Convective thermal resistance at the inner surface of the annulus
- Conductive thermal resistance through the plexiglass tube
- Conductive thermal resistance through the insulation
- Convective thermal resistance at the insulation to the ambient air

By first-order approximations, it was found that both convective thermal resistances were negligible to the thermal resistances by conduction. Thus, only the conductive thermal resistances were considered. By first-order approximations, the conductive thermal resistance by a cylinder ($R_{cylinder}$) may be expressed as follows:

$$R_{cyl} = \frac{\ln\left(\frac{r_2}{r_1}\right)}{2\pi L k} \qquad (36)$$

Here, r_1 and r_2 refer to the inner and outer radii of the cylinder, L to the length of the cylinder and k to the thermal conductivity of the cylinder. The thermal conductivities of the plexiglass tube (R_{pg}) and insulation (R_{ins}) were as specified by the manufacturers' datasheets and as reported earlier in sections 3.2.3 and 3.2.5. The effective thermal resistance by the plexiglass tube and insulation (R_{tot}) was calculated by adding their separate resistances as:

$$R_{total} = R_{pg} + R_{ins} \qquad (37)$$

The heat lost or gained through the plexiglass tube and insulation was approximated by using Equation 38). The term T_b and T_{amb} in Eqn. (38) referred to the average bulk fluid temperature and the ambient air temperature.

$$\dot{Q}_{per,ins} = \frac{T_b - T_{amb}}{R_{tot}} \qquad (38)$$

4.4.2 Heat loss through the plexiglass tube without insulation

Due to the nature of the experiments, part of the plexiglass tube could not be covered with insulation while the experiments were carried out, as the TLC surface had to be photographed. At any given time, a 120 mm section of the tube was cleared for this purpose and was not covered with insulation.

Equations 37 to 39 may be used for the first-order heat transfer calculations, where the term R_{ins} is neglected due to the absence of insulation.

4.4.3 Heat loss through end supports of the annulus

Heat was either lost or gained through the end supports of the heating rod. A 10 mm-nylon spacer (Figure 3-4) was inserted between the heating rod and end supports to increase the thermal resistance so that the heat losses or gains could be reduced. Bolts were used to fasten the end supports to the heating rod. The thermal resistance by axial heat conduction (R_{cond}) was calculated using Equation 39, where L refers to the length of the space, k to the thermal conductivity of the nylon – 0.29 W/mK (Çengel and Ghajar, 2011) – and A_c to the cross-sectional area of the nylon end support.

$$R_{cond} = \frac{L}{kA_c} \tag{39}$$

The thermal resistance by the bolts sectoring the end supports to the heating rod (R_{bolt}) was calculated using Equation 39, with a cross-sectional area and thermal conductivity of 45.3 W/mK used for the bolts (Çengel and Ghajar, 2011).

The equivalent thermal resistance (R_{total}) offered by the nylon spacer and bolts was calculated using Equation 40 by considering them as an equivalent parallel resistive network.

$$\frac{1}{R_{tot}} = \frac{1}{R_{nylon}} + \frac{1}{R_{bolt}} \tag{40}$$

The heat transferred through the end supports was then calculated using Equation 38.

4.5 Thermal resistance of protective adhesive layer

As mentioned, the TLCs used in this investigation were water soluble. To protect the TLCs, a transparent adhesive layer was applied to prevent them from being washed off by the water in the annular flow passage. Van der Westhuizen et al. (2014) used a clear acrylic layer. However, to ensure a layer with consistent thickness, the protective adhesive layer was used.

The water in the annular flow passage would be in contact with the protective adhesive layer. The adhesive layer was a transparent PVC and had the properties mentioned in Section 3.2.2. The indicated TLC colour would represent the temperature state on the inside of the PVC film, not the wetted outside of the PVC film. Thus, the effective thermal resistance of the PVC film and its interface would result in a temperature difference over the protective layer. This temperature difference across the adhesive layer ΔT_{adh} had to be determined. The actual wetted wall temperature, T_w, was determined by subtracting the temperature difference across the protective layer from the temperature measurements of the TLCs, T_{TLC}. This equated mathematically to Equation 41.

$$T_w = T_{TLC} - \Delta T_{adh} \tag{41}$$

The temperature difference across the protective layer, ΔT_{adh}, could be calculated once the thermal resistance of the layer, R_{adh}, was known. For a specific heat rate, $\dot{Q}$, this could be calculated using Equation 42.

$$\Delta T_{adh} = \dot{Q} R_{adh} \tag{42}$$

The value of ΔT_{adh} had a major influence on the results of this investigation due to the local heat transfer coefficient dependence on the wall temperature and, more specifically, the local difference between the wall and the fluid temperatures. Thus, an effort was made to determine the value of R_{adh} as accurately as possible. Two distinctly different methods were used to approximate the value of R_{adh}. A first-order mathematical approximation and an experimental investigation were used to ensure an accurate representation of the temperature difference across the adhesive layer.

For the mathematical approximation, the value of R_{adh} was approximated by using Equation 36, where the values of r_2 and r_1 were measured with a micrometer that has an accuracy of ±0.01 mm. The adhesive layer was manufactured from pure PVC, with an assumed thermal conductivity of 0.19 W/mK (Callister and Rethwisch, 2007). The first-order mathematical approximation estimated the value of R_{adh} to be 0.004996 ˚C/W.

For the experimental approach, an investigation was performed in which the temperature readings of the TLCs were compared for two and three protective adhesive layers. By running a baseline test with two and then three protective layers, the increase in temperature due to the extra layer could be used to calculate the value of the thermal resistance of the protective adhesive layer. Initially, two protective layers were applied over the TLCs, after which the temperatures were recorded for six different flow rates, while keeping the heat rate constant. The tested flow rates ranged from Re = 2 000 to Re = 6 000 with increments of 1 000. After all temperature readings had been taken, a third layer was applied. Temperature readings were also recorded for the same heat flux and flow rates. The TLC temperature difference between two and three layers could now be used to calculate R_{adh} by employing Equation 42. From the investigation, the value of R_{adh} was approximated to be 0.00494 ˚C/W. This is within 1.1% of the value obtained with the first-order mathematical approach. For more information regarding the experimental investigation, please refer to Appendix D.

The experimentally calculated value for R_{adh} was employed for the remainder of the investigation and was used for all calculation purposes, as it was based on actual experimental data.

4.6 Annular fluid heat transfer rate and bulk temperature

The bulk fluid temperature at all locations along the flow passage was needed to calculate the heat transfer coefficients. This bulk fluid temperature could not be measured, as it would obstruct the imaging process and it was thus approximated.

The bulk fluid temperature at any axial position, x, was calculated by remembering that a uniform heat flux source was used and that the temperature of the bulk fluid increased linearly along the length of the heating rod. It was also assumed that the heat losses or gains were insignificant and were neglected (see Section 4.4). This assumption was valid, as the percentage error between the calculated and measured temperature, with respect to the measured temperature, was at a maximum 2.01% and on average 0.6%, which seemed to be insignificant. Equation 43 was used to calculate the bulk fluid temperature at any axial location $T_b(x)$.

$$T_b(x) = T_{bin} + \frac{x}{L_{ws}} \frac{(\dot{Q}_{elec} - \dot{Q}_{loss})}{\dot{m}Cp} \tag{43}$$

In Equation 43, T_{bin} refers to the inlet bulk fluid temperature that was recorded, L_{ws} refers to the length of the wetted surface, $\dot{Q}_{elec}$ refers to the heating rate of the heating rod, and $\dot{m}$ refers to the mass flux of water in the annulus. The values of C_p and any other fluid properties were calculated by the method proposed by Popiel and Wojtkowiak (1998) at the average bulk fluid temperature between the inlet and outlet measuring stations.

4.7 Annular heat transfer coefficients

For this investigation, the local heat transfer coefficients were determined at the inlet region of the annular flow passage for different inlet geometries. The local heat transfer coefficients were obtained at 33 axial locations along the heating rod. Equation 44 was used to calculate the local heat transfer coefficients at any axial location $h(x)$.

$$h(x) = \frac{(\dot{Q}_{elec} - (\dot{Q}_{loss})}{A_s(T_w(x) - T_b(x))} \tag{44}$$

In Equation 44, $\dot{Q}_{elec}$ refers to the heat rate of the heating rod, A_s refers to the surface area of the heating rod, and $T_w(x)$ and $T_b(x)$ refer to the wall and bulk fluid temperature at any axial location x. The use of the total heat transfer rate and total wetted surface area is suitable because of the uniformity of the heat flux. The wetted surface was calculated in Section 3.2.3 as 0.0897 m^2.

The wall temperature $T_w(x)$ represented the average wall temperature around the circumference of the heating rod at a specific axial location, x. This wall temperature was calculated as the arithmetic average temperature of the eight radial locations. Note that the value of T_w was calculated using Equation 41 and accounts for the temperature difference across the protective adhesive layer. The bulk fluid temperature, $T_b(x)$, was calculated using Equation 43.

4.8 Local Nusselt numbers

The local Nusselt numbers, $\mathrm{Nu}(x)$, were calculated from Equation 45. For this, the local heat transfer coefficients had to be calculated from Equation 44.

$$\mathrm{Nu}(x) = \frac{h(x)D_h}{k(x)} \tag{45}$$

In Equation 45, $h(x)$ refers to the local heat transfer coefficients, D_h refers to the hydraulic diameter, and k refers to the thermal conductivity of the fluid in the annular passage. The thermal conductivity was calculated by the relations proposed by Popiel and Wojtkowiak (1998), using the mean bulk temperature.

The local heat transfer coefficients and local Nusselt numbers allow one to study the inlet effects of an annular flow passage. One may get an idea of how the boundary layers grow and how heat transfer is restricted with fully developed flow.

4.9 Area-weighted heat transfer coefficients

This section deals with calculating the area-weighted heat transfer coefficients. As mentioned in Section 3.2.3, the annular flow passage was L_{ws} = 1 050 mm in length. However, the heat transfer coefficients could only be determined for 540 mm, as measured from the inlet, due to restrictions of the imaging mechanism.

The area-weighted heat transfer coefficients were determined by calculating the average of the local heat transfer coefficients. As two different sample area sizes were used in this study, the average could not simply be calculated.

As the smaller sample areas were half the size of the larger sample area, these areas were considered by calculating the sum of the local heat transfer coefficients and dividing the sum by two as the sample area was half that of the larger sample area.

For the larger sample areas, the average was computed as usual. With this method, there were now 27 sample lengths of 20 mm (used to compute the area-weighted heat transfer coefficients with a sample length of 20 mm). However, there were still 33 sample lengths. Equation 46 was used to calculate the area-weighted heat transfer coefficients. The first summation term represents the smaller sample areas and the second the larger sample areas.

$$h_{avg} = \left(\frac{\sum_{i=1}^{12} h_i}{2} + \sum_{i=13}^{27} h_i\right)/27 \tag{46}$$

4.10 Account for inlet water temperature drift

Drifts in the inlet bulk water temperature were inevitable. Heated water from the annular flow passage resulted in a temperature escalation of the water in the 1 000-litre reservoir and cold water entered the reservoir from the 5 000-litre reservoir, cooled by the chiller. An effort was made to design and build the experimental setup so that the readings could be taken as quickly as possible and so that these temperature drifts could be limited.

A typical temperature drift of inlet and outlet temperatures can be seen in Figure 4-9. These temperatures represented the average temperature of the eight thermocouples located at each measuring station. The photography mechanism typically took 19 minutes to capture all the required photographs. The temperature drift was generally 0.06 ˚C over the 19 minutes. The typical temperature drift was small as the thermostatically controlled chiller in the 5 000-litre reservoir only engaged once the temperature exceeded its upper operating limits. The temperature drift seen in Figure 4-9 was caused by the warmer water exiting the annular flow passage and mixing with the water in the 1 000-litre reservoir. Also see Figure 3-1.

This temperature drift had to be considered because the local heat transfer coefficients were calculated from the bulk fluid temperature, as expressed in Equation 44. With a temperature drift, the bulk inlet fluid temperature would not remain constant with time. Unless the local bulk fluid temperature was not adjusted in accordance with the drift at the inlet of the test section, it would lead to incorrectly calculated heat transfer coefficients.

As mentioned, the system clocks on the Raspberry Pi and data-logging computer were synchronised. Thus, all readings were logged against the same reference time scale. The time at which each picture was taken was stored as metadata for the picture. The wall temperatures of the of the annular flow passage were adjusted to incorporate the temperature drift with reference to the inlet temperature when the experiment was started. Thus, the effect of the drift had been eliminated.

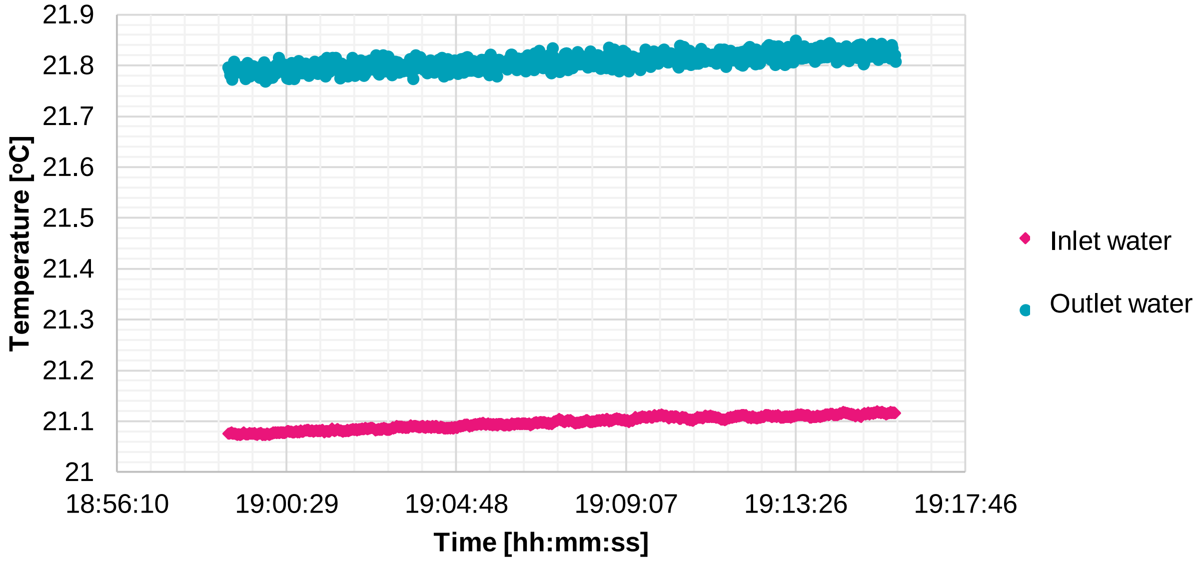

Figure 4-9: Typical inlet water temperature drift

In some cases, other temperature drift patterns were present. Figure 4-10 is a typical representation of what happened when the thermostatically controlled chiller was engaged. Initially, the inlet and outlet water temperatures increased steadily, after which a drastic decrease in inlet water temperatures is seen. This decrease is due to the chiller engaging when the water in the cold-water storage tank reached the upper thermostatic limiting temperature.

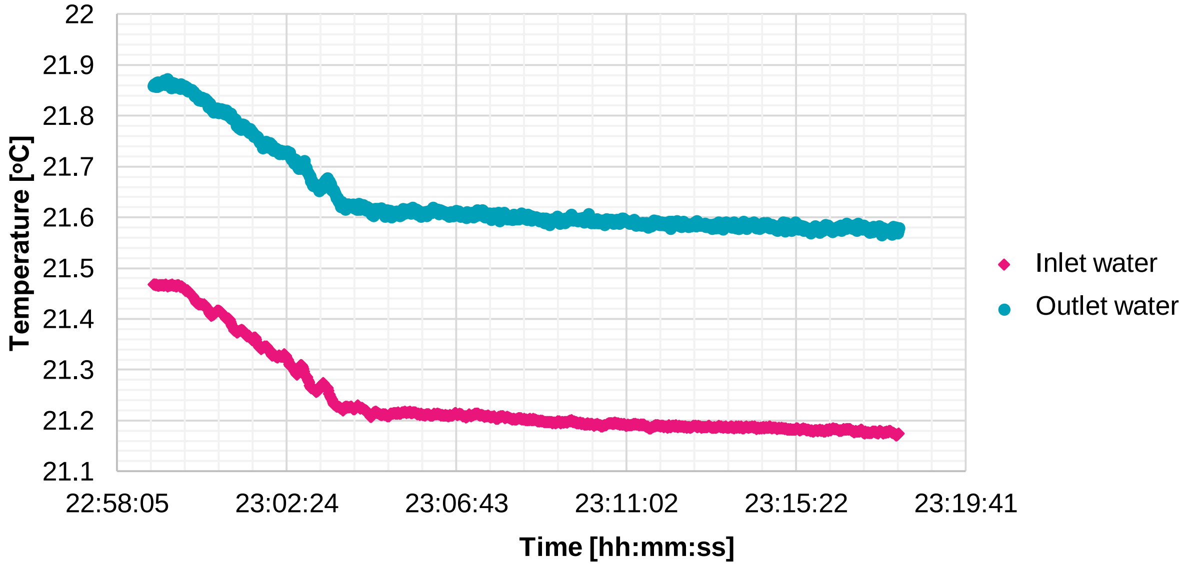

Figure 4-10: Inlet water temperature drift due to the chiller

An effort was made to run experiments while the chiller was not on to gather accurate and repeatable results. Cases that exhibited the inlet temperature history profile such as the one shown in Figure 4-10 were not included in the final set of results, since steady-state conditions could not have been guaranteed for the entire time span of the experiment, even though such cases might have reached a steady state at the start of the test.

4.11 Uncertainty analysis

Errors that occur during measurements have uncertainties associated with the measured values. These uncertainties influence the experimental results and the level of certainty in the results. For this reason, an uncertainty propagation analysis is vital for all experimental investigations in order to predict the range in which the actual values of a measurement or calculation lies. This is also referred to as the uncertainty interval.

It is important to express the uncertainty of a result of an investigation with the same weights as the individual measurements used to calculate the result. During an uncertainty analysis, one is able to estimate the influence that the individual uncertainties may have, known as a sensitivity analysis. The method used to calculate the uncertainties in this investigation is the method prescribed by Moffat (1988).

The uncertainty of a calculated result (δR) was calculated by using the root-sum square combination, where $X_1, X_2, X_3 \ldots X_N$ are independent measurements or calculations. The uncertainty of a calculation will have the same unit as the result itself.

$$\delta R = \left\{ \sum_{i=0}^{n} \left(\frac{\partial R}{\partial X_i} \delta X_i \right)^2 \right\}^{0.5} \tag{47}$$

As the thermal resistance of the protective adhesive layer was found by experimentation, the scatter of the experimental results was used to determine the uncertainty of the thermal resistance of the protective adhesive layer. The method employed for this was the one suggested by Dunn (2014), which deals with the precision or confidence interval in terms of the true mean of a value, which is the mean thermal resistance in this case. The uncertainty was calculated by employing Equation 48, in which $t_{v,P}$ refers to a constant in a two-sided T-type distribution and $S_{\bar{x}}$ to the standard deviation.

$$\delta R = t_{v,P} S_{\bar{x}} \tag{48}$$

Please consult Appendix C for more information on the uncertainty analysis and sample uncertainty calculations.

4.11.1 Uncertainties of measured quantities and material properties

Several measuring devices were used in this study. The uncertainties of these devices, along with the measuring methods that were used, had a significant impact on the uncertainties of the results. The uncertainty values of the devices or methods used are summarised in Table 4-1 and were obtained from the manufacturers' data. All uncertainties listed as percentages were converted to the units in which the measurement appeared. These uncertainties are obtained by multiplying the uncertainty percentage with the measured value.

Table 4-1: Uncertainties of equipment used

Device	Range	Uncertainty
Single thermocouple	-200 ˚C to 350 ˚C	±0.11 ˚C
PT100	0 ˚C to 100 ˚C	0.1 ˚C
ThermaCAM E65	-20 ˚C to 250 ˚C	±2 ˚C
TLC pixel	20 ˚C to 41 ˚C	0.5 ˚C
Coriolis flow meter	0.015 kg/s to 0.603 kg/s	0.11% of reading
Vernier calliper	0 mm to 200 mm	20 µm
Micrometer	0 mm to 30 mm	10 µm
Measuring tape	0 mm to 5 000 mm	1 mm
Power supply	0 V to 360 V 0 A to 30 A	0.2% of reading 0.2% of reading

Table 4-2 lists all the uncertainties associated with the thermophysical properties used in this study. The properties were calculated by the relations prescribed by Popiel and Wojtkowiak (1998).

Table 4-2: Uncertainties associated with the thermophysical properties

Property	Range	Uncertainty (%)
Cp	0 to 150 ˚C	0.06
k	0 to 150 ˚C	2.00
ρ	0 to 150 ˚C	0.04
μ	0 to 150 ˚C	1.00

4.11.2 Results of the uncertainty analysis

Uncertainty analyses were performed for all test cases. A sample calculation of the uncertainty analysis can be found in Appendix C. Table 4-3 shows a condensed list of the uncertainties calculated for some of the experimental results to analyse the propagation of the uncertainties from the raw measured data to the final calculated results.

Table 4-3: Condensed uncertainties for test case A

Re	$\delta\dot{q}$ (%)	δT_B ($^{\circ}C$)	δT_{TLC} ($^{\circ}C$)	δR_{adh} ($^{\circ}C$)	$\delta\Delta T_{adh}$ ($^{\circ}C$)	δT_w ($^{\circ}C$)	δh_{max} (%)	δh_{avg} (%)
2 041	0.794	0.0389	0.0015	8.81	0.348	0.348	17.68	9.20
3 079							20.41	9.98
4 121							24.90	12.10
5 129							28.21	13.59
6 167							27.74	14.42
7 200							29.93	15.55

It is evident from Table 4-3 that the uncertainty of the heat flux, $\delta\dot{q}$ is quite small due to the accuracy of the measuring equipment and power supply. The uncertainty of the bulk fluid measuring station, δT_B, was drastically reduced from 0.11 ˚C for one thermocouple to 0.0389 ˚C because eight thermocouples were used to measure the temperature at each station. The same was evident for the uncertainty of the temperature reading of the TLC sample area, as the sample area was composed of 113 400 pixels. The measuring uncertainty of a single TLC pixel is said to be between 0.4 ˚C and 0.5 ˚C, as suggested by Rao and Zang (2010). Due to the vast number of pixels in the TLC sample area, this uncertainty is drastically reduced.

The uncertainty of the thermal resistance of the protective adhesive layer was relatively large at 8.81%. As mentioned, the thermal resistance of the protective layer was calculated by performing an experimental investigation. The results of the investigation were scattered about the mean and thus the uncertainty was calculated by considering the standard deviation around the mean of the thermal resistance. The uncertainty of the thermal resistance of the protective adhesive layer was carried over to the temperature difference across the protective adhesive layer. This uncertainty carried the most weight in the uncertainty of the wall temperature and heat transfer coefficients.

The uncertainties of the increased overall heat transfer coefficients ranged from 9.2% to 15.55% for the Reynolds numbers range of 2 041 to 7 200. The uncertainty of the overall heat transfer coefficient increased as the Reynolds numbers increased. The increase in uncertainties can be attributed to the decrease in the temperature difference between the wall and the bulk fluid temperatures.

When considering the uncertainties of the local heat transfer coefficients, the uncertainties for these local heat transfer coefficients ranged from 17.68% to 29.93%. The uncertainties were largest at the inlet region. The local uncertainties for some flow rates were plotted in Figure 4-11. From this, it is clear that the uncertainties are highest at the inlet and tend to decrease further down the tube. The reason for the uncertainties being large at the inlet is that the temperature difference between the wall and the bulk fluid temperature is small, which results in a large uncertainty. Further down the tube, this temperature difference increases, which results in a smaller local uncertainty. It is also evident that the higher the flow rate, the higher the uncertainty.

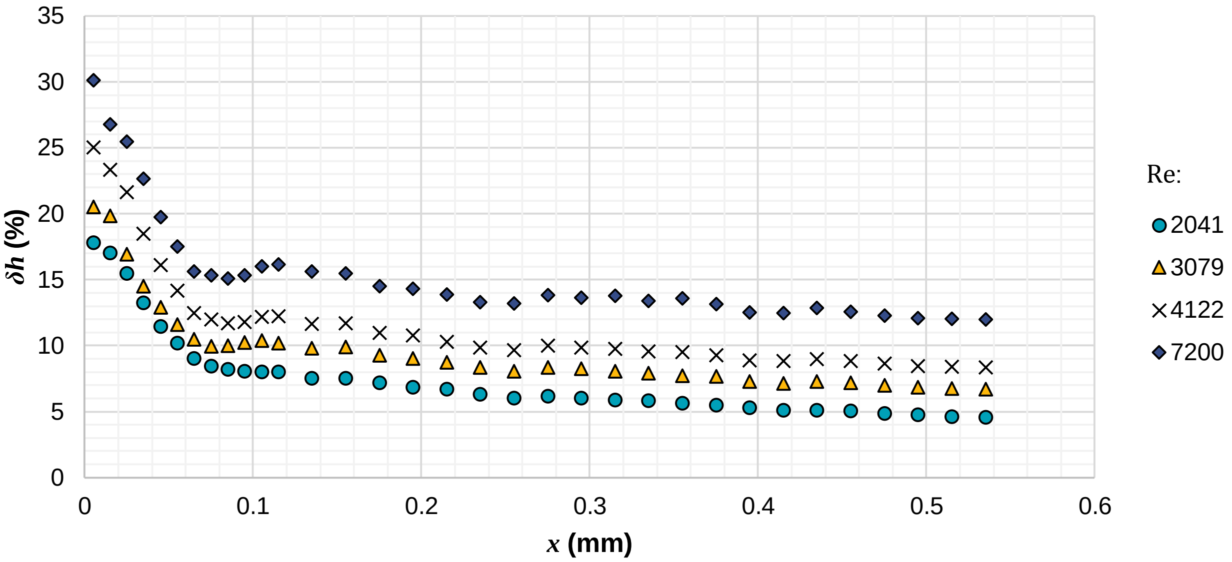

Figure 4-11: Local heat transfer coefficient uncertainties for test case A

The thermal resistance uncertainty of the protective adhesive layer was the largest contributor to uncertainties for the experiments. It must be said that the protective adhesive layer was never changed. Thus, all experiments were performed with the same protective adhesive layer with the same uncertainty, which means that they share the same common uncertainty.

4.12 Data analysis summary

This chapter dealt with the method used to calculate local and overall heat transfer coefficients from the raw experimental data. Particular focus was given to the calibration and interpretation of the TLC images and the method whereby the local temperatures were extracted from the images. The temperature difference across the protective adhesive layer needed to be known and was determined by means of an experiment. The section concluded with the uncertainty analysis. The largest contributor to the uncertainty was the thermal resistance of the protective adhesive layer.

5. Results

The experimental results obtained from processing the raw experimental data with the methods discussed in Chapter 4 are presented in this chapter. Tabulated results of a typical test case are presented, with an analysis of the TLC temperature fields. The local and overall heat transfer coefficients are considered for all test cases (varying inlet diameters and on- and off-axis inlet configurations) to determine the optimal inlet size and compare the results to existing correlations. The local and overall heat transfer coefficients are evaluated for the transition from laminar to turbulent flow. A new correlation is developed to anticipate the overall heat transfer of a short annular flow passage for low turbulent flow cases, considering the local heat transfer coefficients.

5.1 Test cases

In this section, the experimental test conditions are presented for test case A (on-axis inlet with D_3 = 20 mm, as discussed in Section 3.2.4). The Reynolds number, bulk inlet and outlet temperatures, mass fluxes and energy balances for the entire test range for test case A is presented in

Table 5-1.

The Reynolds number range for the test cases was in the lower turbulent to fully turbulent flow regime from approximately Re = 2 000 to Re = 7 500. The heat flux of the heating rod was kept constant for all test cases at 4 700 W/m^2. The flow states for test cases A, B and C were all in the turbulent, low turbulent flow regimes. In these flow states the effects of secondary flow (buoyancy driven flow) are minimalized and noted to be insignificant due to the chaotic flow of the fluid in the flow passage as noted by Ghajar and Tam (1994). Thus different heat fluxes/ heating rates would not influence or enhance the heat transfer in the flow passage as also identified in the work by Hallquist (2011).

The lower bound of the turbulent flow regime was found to begin at Reynolds numbers of 1 000, as discussed in Section 5.6.

As seen from

Table 5-1, the inlet temperatures for the experiments varied due to warming and cooling in the 1 000-litre cold water reservoir. The energy balances for the investigations were all smaller than 2.5%, with an average energy balance error of approximately 1.4%. This means that the test setup was relatively well insulated from heat losses or gains to and from the environment.

Table 5-1: Experimental test conditions for test case A

Re	$T_{B_{in}}$ (°C)	$T_{B_{out}}$ (°C)	$\dot{m}_a$ (kg/s)	$\dot{Q}_{elec}$ (W)	eb (%)
2 041	20.95	21.85	0.109	399.24	-0.6
2 561	21.08	21.79	0.136	399.24	-1.3
3 079	21.18	21.76	0.163	399.24	-1.3
3 604	21.29	21.80	0.190	399.24	-1.0
4 122	21.37	21.81	0.217	399.24	-1.0
4 649	21.47	21.62	0.244	399.24	-2.1
5 129	21.16	21.50	0.272	399.24	-1.3
5 640	21.17	21.48	0.299	399.24	-1.8
6 167	21.21	21.49	0.326	399.24	-1.4
6 681	21.26	21.52	0.353	399.24	-1.1
7 200	21.32	21.57	0.380	399.24	-2.2
7 728	21.38	21.62	0.407	399.24	-1.0

5.2 Temperature measurements

The wall and bulk fluid temperature measurements are discussed in this section. Emphasis is placed on the wall temperature measurements made with the TLCs. The temperature fields of the annular flow passage are presented first, after which the average circumferential wall temperatures for each axial location are considered.

The temperature fields presented here are the wall temperatures of the wetted surface in the annular flow passage. These temperatures were calculated from the temperatures of the TLCs by subtracting the temperature difference across the protective layer, as discussed in Section 4.5.

Not all temperature fields will be discussed here. Only important findings will be addressed.

5.2.1 Wall temperature measurements

A typical wall temperature field can be seen in Figure 5-1. The axial distance from the inlet along the annular flow passage is plotted on the horizontal axis (second row) and the radial position around the circumference on the vertical axis (first column). On the vertical axis, 0° is taken in line with the inlet. Some sections at the inlet of the temperature field were neglected and coloured black as the camera's view and lighting were obscured by the inlet of the annulus. A colour scale was added to the temperature field, where green represents the lower temperatures and red the higher temperatures of the temperature field.

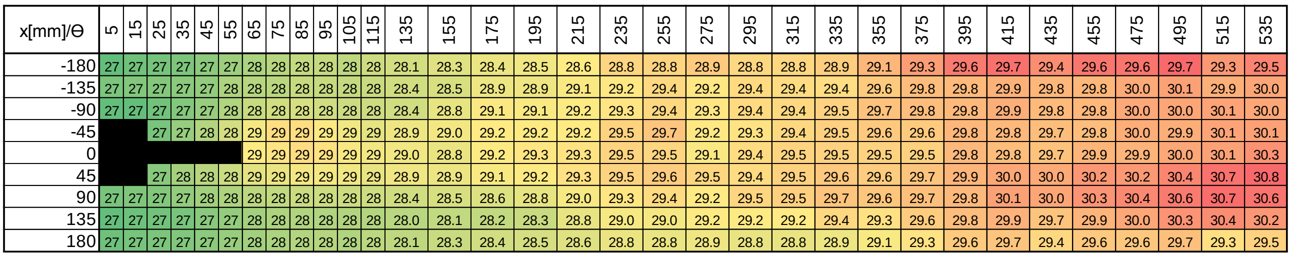

x[mm]/Θ	5	15	25	35	45	55	65	75	85	95	105	115	135	155	175	195	215	235	255	275	295	315	335	355	375	395	415	435	455	475	495	515	535
-180	27	27	27	27	27	27	28	28	28	28	28	28	28.1	28.3	28.4	28.5	28.6	28.8	28.8	28.9	28.8	28.8	28.9	29.1	29.3	29.6	29.7	29.4	29.6	29.6	29.7	29.3	29.5
-135	27	27	27	27	27	28	28	28	28	28	28	28	28.4	28.5	28.9	28.9	29.1	29.2	29.4	29.2	29.4	29.4	29.4	29.6	29.8	29.8	29.9	29.8	29.8	30.0	30.1	29.9	30.0
-90	27	27	27	27	27	28	28	28	28	28	28	28	28.4	28.8	29.1	29.1	29.2	29.3	29.4	29.3	29.4	29.4	29.5	29.7	29.8	29.8	29.9	29.8	29.8	30.0	30.0	30.1	30.0
-45			27	27	28	28	29	29	29	29	29	29	28.9	29.0	29.2	29.2	29.2	29.5	29.7	29.2	29.3	29.4	29.5	29.6	29.6	29.8	29.8	29.7	29.8	30.0	29.9	30.1	30.1
0							29	29	29	29	29	29	29.0	28.8	29.2	29.3	29.3	29.5	29.5	29.1	29.4	29.5	29.5	29.5	29.5	29.8	29.8	29.7	29.9	29.9	30.0	30.1	30.3
45			27	28	28	28	29	29	29	29	29	29	28.9	28.9	29.1	29.2	29.3	29.5	29.6	29.5	29.4	29.5	29.6	29.6	29.7	29.9	30.0	30.0	30.2	30.2	30.4	30.7	30.8
90	27	27	27	27	28	28	28	28	28	28	28	28	28.4	28.5	28.6	28.8	29.0	29.3	29.4	29.2	29.5	29.5	29.7	29.6	29.7	29.8	30.1	30.0	30.3	30.4	30.6	30.7	30.6
135	27	27	27	27	27	27	28	28	28	28	28	28	28.0	28.1	28.2	28.3	28.8	29.0	29.0	29.2	29.2	29.2	29.4	29.3	29.6	29.8	29.9	29.7	29.9	30.0	30.3	30.4	30.2
180	27	27	27	27	27	27	28	28	28	28	28	28	28.1	28.3	28.4	28.5	28.6	28.8	28.8	28.9	28.8	28.8	28.9	29.1	29.3	29.6	29.7	29.4	29.6	29.6	29.7	29.3	29.5

Figure 5-1: Wall temperature field for test case A, Re = 3 603

By considering the temperature field in Figure 5-1, it is evident that at approximately x = 65 mm to 115 mm and θ = -45˚ to 45˚, the tube was warmer compared to other radial positions at the same axial locations. This could be due to reduced fluid flow on this spot of the heating rod (due to the geometry of the inlet), which allows the heating rod to heat up in this section, as heat is not removed as effectively. This caused this section of the tube to heat up more compared to other radial locations due to the nature of the fluid flow in an annular flow passage.

Figure 5-2 shows the average wall temperatures for some axial position ranges around the circumference of the heat transfer surface. The radial positions are plotted on the horizontal axis and the wetted wall temperatures are plotted along the vertical axis. It must be noted that the temperature for the axial position x = 0 mm to 50 mm does not extend though the entire radial location as some wall temperatures needed to be neglected at the inlet region due to visual interference by the inlet on the imaging equipment as mentioned previously. There are large temperature variations in the radial positions at the inlet region (x = 0 mm to 50 mm and x = 50 mm to 100 mm). These large variations are caused by the layout of the inlet, which causes an impingement of the heat transfer surface as the fluid flows around the heating rod when it enters the annular flow region. As the flow develops further down the tube, the temperature distribution starts to steady out. The wall temperatures increase as the flow moves further down the heating rod, as seen from Figure 5-1 and Figure 5-2.

For test cases A, B, C and E, a symmetric temperature profile is anticipated as the flow enters the annulus with an on-axis inlet. The wall temperature distributions in Figure 5-1 and Figure 5-2 seem relatively symmetric about the θ = 0˚ radial position. Small variations may be caused by variations on the painted surface or by non-uniform heat fluxes. A symmetric temperature profile is not anticipated for the off-axis inlet, for test case D, which will be discussed shortly.

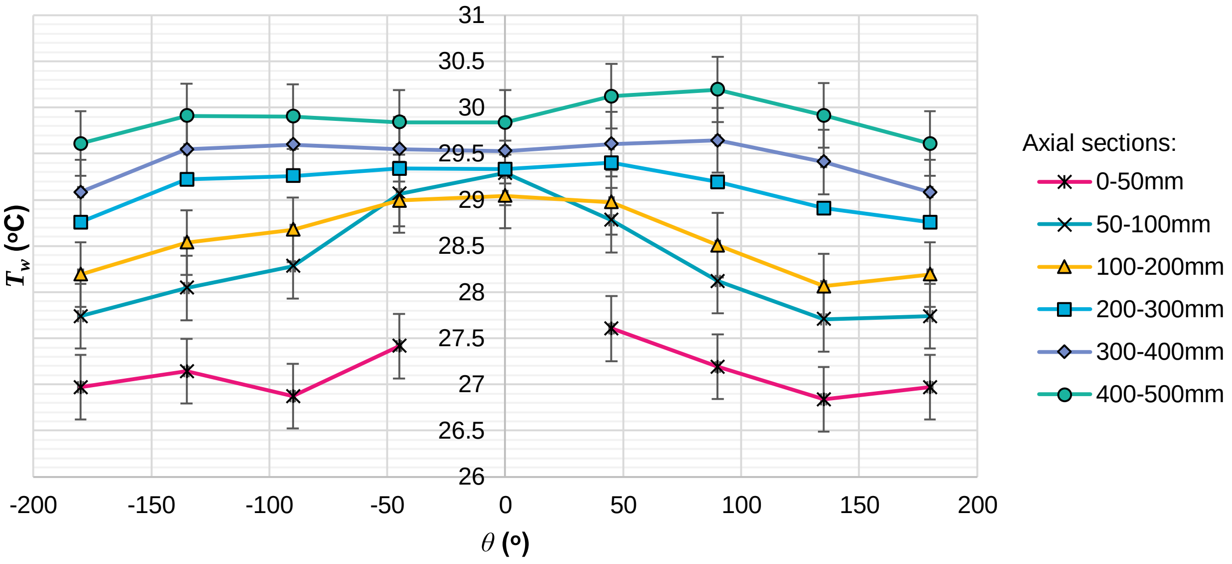

Figure 5-2: Wall temperature distribution around the circumference

The wall temperature fields for the other on-axis test cases A, B, C and E were similar to the one observed in Figure 5-1. It was clear that the overall wall temperatures decreased and the flow rate of the water in the annulus increased as the heat flux was kept constant for the test cases.

For the off-axis inlet case, test case D, fluid swirl was induced in the annular flow passage. The induced fluid swirl can be visualised by considering the wetted wall temperature, which is shown in Figure 5-3. Definite warm and cool temperature bands can be seen diagonally across the temperature field. This swirl effect caused a non-uniform temperature distribution around the heating rod. These bands are caused either by different flow velocities of the fluid in the annulus or by water bands flowing concurrent to each other with different temperatures.

The temperature bands tend to be stretched out further down the tube, suggesting that the swirl motion tends to die out further from the inlet. Figure 5-3 highlights the potential of using TLC in heat transfer studies.

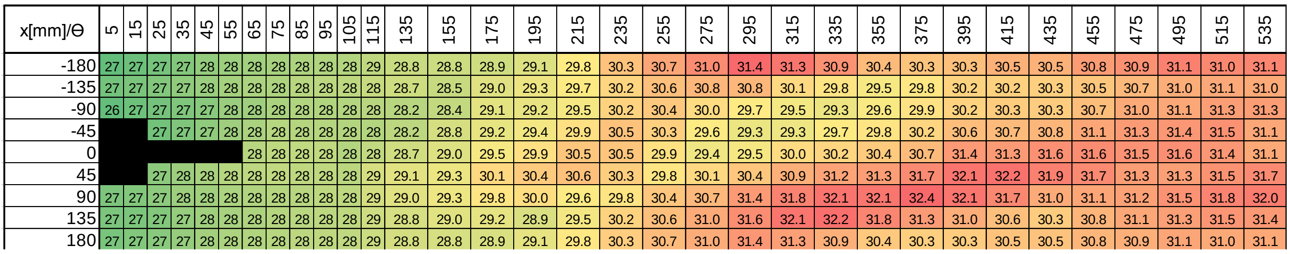

x[mm]/Θ	5	15	25	35	45	55	65	75	85	95	105	115	135	155	175	195	215	235	255	275	295	315	335	355	375	395	415	435	455	475	495	515	535
-180	27	27	27	27	28	28	28	28	28	28	28	29	28.8	28.8	28.9	29.1	29.8	30.3	30.7	31.0	31.4	31.3	30.9	30.4	30.3	30.3	30.5	30.5	30.8	30.9	31.1	31.0	31.1
-135	27	27	27	27	28	28	28	28	28	28	28	28	28.7	28.5	29.0	29.3	29.7	30.2	30.6	30.8	30.8	30.1	29.8	29.5	29.8	30.2	30.2	30.3	30.5	30.7	31.0	31.1	31.0
-90	26	27	27	27	27	28	28	28	28	28	28	28	28.2	28.4	29.1	29.2	29.5	30.2	30.4	30.0	29.7	29.5	29.3	29.6	29.9	30.2	30.3	30.3	30.7	31.0	31.1	31.3	31.3
-45			27	27	27	28	28	28	28	28	28	28	28.2	28.8	29.2	29.4	29.9	30.5	30.3	29.6	29.3	29.3	29.7	29.8	30.2	30.6	30.7	30.8	31.1	31.3	31.4	31.5	31.1
0							28	28	28	28	28	28	28.7	29.0	29.5	29.9	30.5	30.5	29.9	29.4	29.5	30.0	30.2	30.4	30.7	31.4	31.3	31.6	31.6	31.5	31.6	31.4	31.1
45			27	28	28	28	28	28	28	28	28	29	29.1	29.3	30.1	30.4	30.6	30.3	29.8	30.1	30.4	30.9	31.2	31.3	31.7	32.1	32.2	31.9	31.7	31.3	31.3	31.5	31.7
90	27	27	27	28	28	28	28	28	28	28	28	29	29.0	29.3	29.8	30.0	29.6	29.8	30.4	30.7	31.4	31.8	32.1	32.1	32.4	32.1	31.7	31.0	31.1	31.2	31.5	31.8	32.0
135	27	27	27	27	28	28	28	28	28	28	28	29	28.8	29.0	29.2	28.9	29.5	30.2	30.6	31.0	31.6	32.1	32.2	31.8	31.3	31.0	30.6	30.3	30.8	31.1	31.3	31.5	31.4
180	27	27	27	27	28	28	28	28	28	28	28	29	28.8	28.8	28.9	29.1	29.8	30.3	30.7	31.0	31.4	31.3	30.9	30.4	30.3	30.3	30.5	30.5	30.8	30.9	31.1	31.0	31.1

Figure 5-3: Wall temperature field for test case D, $\mathrm{Re} = 3\ 595$

5.2.2 Average circumferential wall temperatures

In this section, the average circumferential wall temperature profiles along the length of the test section are discussed. The circumferential wall temperatures were calculated as the average wall temperature for each axial location. Figure 5-4 shows the average circumferential wall temperatures for some flow rates expressed in terms of Reynolds numbers for test case A. The axial position along the flow passage is plotted along the horizontal axis, where x = 0 mm is considered to be the centre of the inlet, and the average circumferential wall temperature is plotted on the vertical axis.

Figure 5-4 shows that the circumferential wall temperatures increase along the length of the annular flow passage. As the Reynolds numbers increased, the average wall temperatures decreased along the flow passage. For the given heating rate of 399 W (for this test case), the wall temperature increase over the length were typically in the range of 6.4 ˚C to 1.8 ˚C for the low and high flow rate cases respectively.

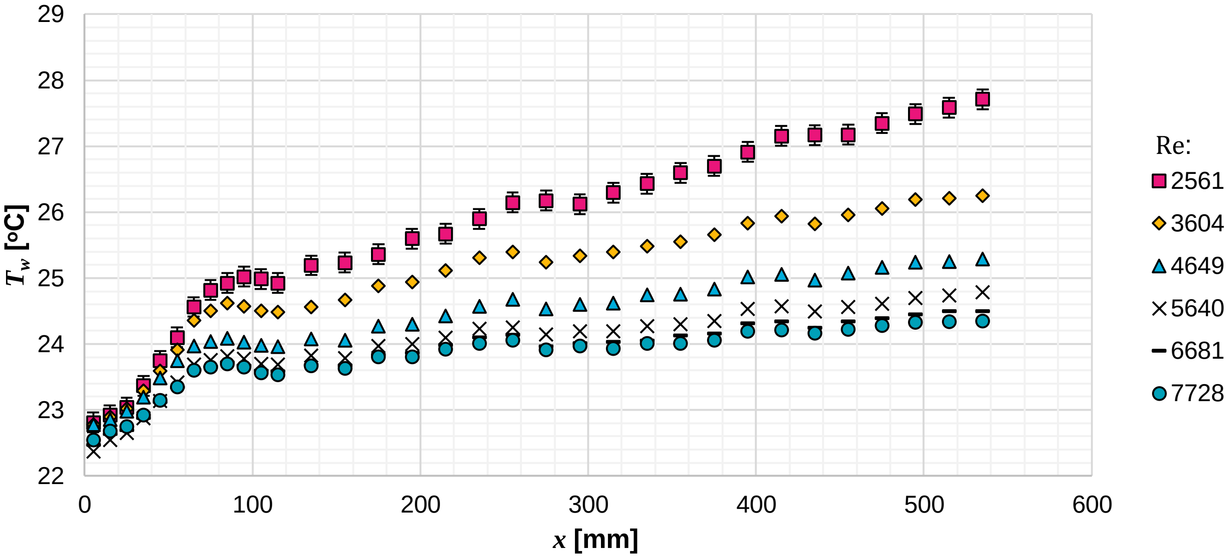

Figure 5-4: The average circumferential wall temperatures for the varying flow rates for test case A

Considering the shapes of the wall temperature distributions, it is evident that the rate at which the circumferential wall temperatures increase is not uniform over the length of the flow passage. Near the inlet, the circumferential wall temperatures increase steeply, after which the rate steadies out from approximately x = 75 mm to 85 mm. Here, there is a definite kink in the shape, after which the gradients of the wall temperature increase change. The differences in the rate at which the temperatures increase may be attributed to the development of the boundary layers. The kink may be interpreted as the entry length of the heat exchanger, where the thermal and velocity boundary layers merge in the annulus. The observed kinks are discussed in more depth in Section 5.3, where the local heat transfer coefficients and boundary layer development is considered. Two additional minor kinks at x = 275 mm to 295 mm and x = 415 mm to 435 mm are present in the circumferential wall temperature distributions, but these are smaller in magnitude and do not alter the rate at which the average wall temperature changes.

To confirm that the kinks seen in the circumferential wall temperature distributions were not due to a heating rod defect or imperfection of the TLC surface, a laminar test case was also considered with Re = 1 000. Figure 5-5 shows the average wall temperature distribution for this case. As can be seen from Figure 5-5, the wall temperature increases steadily and contains no real kinks or jumps in the region of 75 mm to 85 mm and at x = 275 mm to 295 mm and x = 415 mm to 435 mm. Thus, it may be concluded that the kinks seen in Figure 5-4 are due to the flow state and are not caused by imperfections on the painted surface.

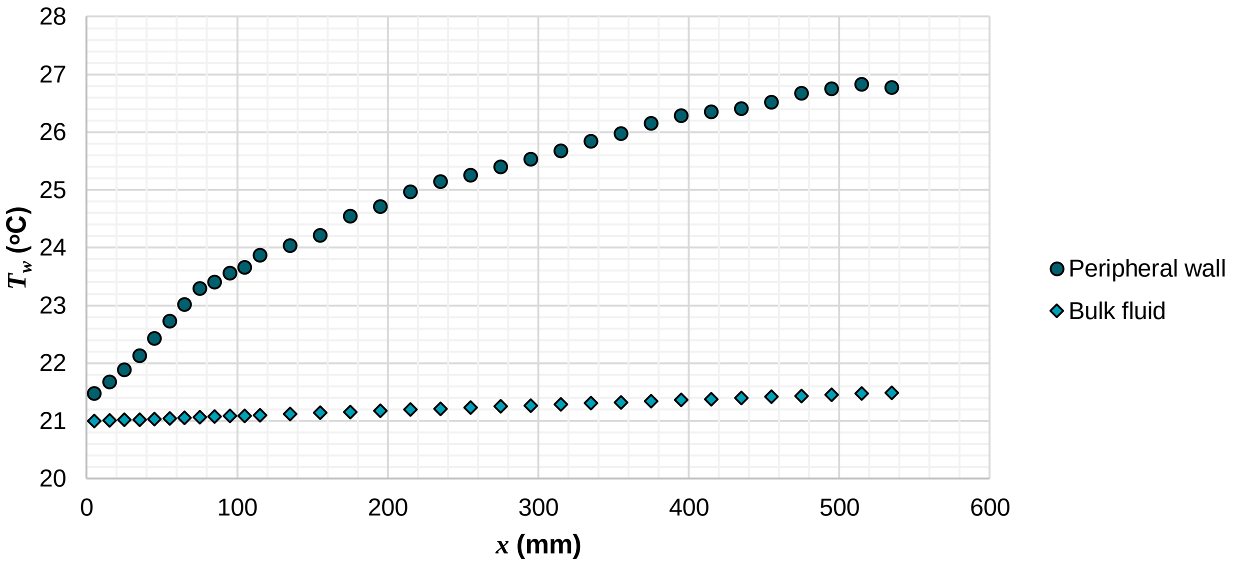

Figure 5-5: Average wall and bulk fluid temperature for Re = 1 021 in test case E

In addition to the peripheral wall temperature, the bulk fluid temperature is also shown in Figure 5-5. The bulk fluid temperature was calculated as discussed in Section 4.6, and thus has a constant gradient. Larger heat transfer coefficients will be anticipated at the regions where the temperatures of the peripheral wall and bulk fluid temperatures are closer together. In the regions where the bulk fluid and peripheral wall temperatures are far apart, smaller heat transfer coefficients are anticipated. Thus, larger local heat transfer coefficients are anticipated at the inlet region of the flow passage, which will decrease as one moves further down the heating rod.

5.3 Local heat transfer coefficients

The main focus of the current study was to experimentally determine the local heat transfer coefficients at the inlet region of a short concentric annular flow passage to study boundary layer growth. This section presents and discusses the experimentally determined local heat transfer coefficients by comparing them to existing correlations and past findings. The local heat transfer coefficients along the length of the annular flow passage were calculated as discussed in Section 4.7. In this section, only test cases A (D_3 = 20 mm), B (D_3 = 15 mm) and C (D_3 = 10 mm) will be considered with on-axis inlet geometries.

It must be noted that the inlet of the annular flow passage obscured the view of the camera and thus the entire surface area at the inlet could not be mapped.

The typical local heat transfer coefficients along the length of the annular flow passage can be seen in Figure 5-6 for test case A, with Re = 3 500. The uncertainties for the local heat transfer coefficients are also plotted, together with the anticipated local heat transfer coefficients, as determined by the correlation of Gnielinski (2009). This correlation is documented in Table 2-3 as Equation 24.

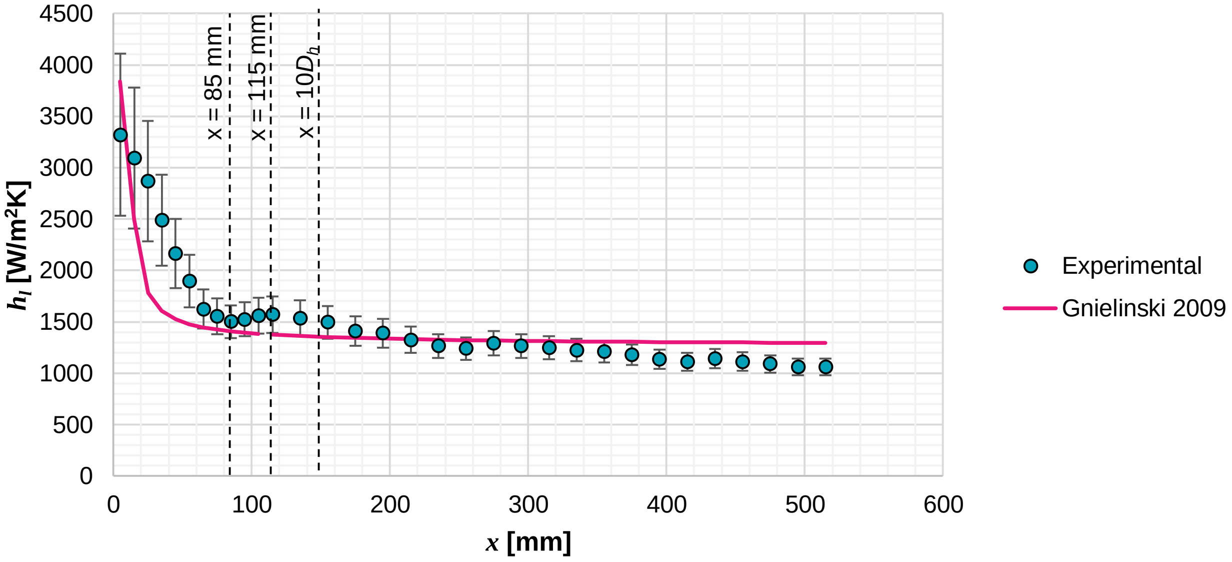

Figure 5-6: Local heat transfer coefficients for test case A at Re = 3 603

The experimentally determined local heat transfer coefficients confirm the literature detailed in Section 2.5 and Section 2.6 in that the local heat transfer coefficients decrease from a maximum at the inlet region of the flow passage to a relatively constant heat transfer coefficient further along the length of the flow passage. The high local heat transfer coefficients at the inlet region are attributed to the absence and development of the boundary layers that have not yet merged in the centre of the flow passage. Further down the flow passage, the local heat transfer coefficients tend to be a relatively constant value once the boundary layers have merged.

The correlation developed by Gnielinski (2009) (Equation 24) is used to describe the average heat transfer coefficient for an annular flow passage of a particular length. From the correlation of Gnielinski (2009), the local heat transfer coefficients were derived from the overall heat transfer coefficients using the midpoint rule of integration.

For the first axial location of x = 5 mm, the local heat transfer coefficient was assumed to be the same as the overall heat transfer coefficient for an annular flow passage of 5 mm. For the next axial location of x = 15 mm, the local heat transfer coefficient was determined so that the average heat transfer coefficient was equal to that of the overall heat transfer coefficients for an annular flow passage of 15 mm. This process continued until all local heat transfer coefficients were determined for the length of interest.

The correlation developed by Gnielinski (2009) follows the same trend as the experimental results for the local Nusselt numbers along the annular flow passage. It must be noted that the suggested Reynolds number range for the Gnielinski correlation is $\mathrm{Re} >$ 10 000, which is above the Reynolds numbers considered here. The correlation does, however, follow the experimental data with some accuracy. The experimental results and correlation suggest a similar fully developed local heat transfer coefficient for x > 115 mm. The experimental local heat transfer coefficient for fully developed flow tends to decrease continually for the length of interest, whereas the correlation suggests a relatively stable value.

As mentioned, the local heat transfer coefficient decreases from a maximum to a relatively constant value further along the flow passage, with a kink between x = 75 mm and x = 115 mm. If one considers the local heat transfer coefficients from the inlet, they decrease from a maximum to approximately x = 85 mm, where the local heat transfer coefficients tend to reach a local minimum value. The local heat transfer coefficients increase from this local minimum to a local maximum at x = 115 mm, after which the local heat transfer coefficients continue to decrease at a slow rate along the flow passage.

This kink, together with the change from a local minimum to a local maximum heat transfer coefficient, may be present due to the boundary layers that merge in the centre of the annular flow passage. This kink has not been identified in such detail by previous authors and is a novel finding for boundary layer development in the annular flow passage. The boundary layers restrict heat transfer and, once developed, limit the heat transfer to a theoretically constant value. For turbulent flow, theory suggests that the hydrodynamic and thermal entry length may be approximated to be $10D_h$ (Çengel and Ghajar, 2011). For this investigation, for test cases A, B and C this equates to a thermal and hydrodynamic entry length of 148 mm. By considering the local heat transfer coefficients as seen in Figure 5-6, the entry length may be approximated 115 mm, which is considered to be the location of the local maximum in the region of the kink. For all flow rate cases considered in the current investigation, the entry length remained relatively constant and only varied by approximately 10 mm. This confirms that, for turbulent flow, the entry length is not significantly dependant on the flow rate, as suggested in theory by the entry length approximation of $10D_h$.

The local heat transfer coefficients for the current study's experimental results and approximations made by the correlation of Gnielinski (2009) for a number of flow rates for test case A are plotted in Figure 5-7. It is evident from Figure 5-7 that higher flow rates result in higher heat transfer rates. All local heat transfer rates follow the same trend from a maximum at the inlet, which decreases to a relatively constant fully developed heat transfer rate value.

By only considering the experimental results in the region from x = 75 mm to x = 115 mm, it is evident that the kink noted and discussed earlier is larger for higher heat transfer rates. At low flow rates with Re = 2 041, the kink is barely visible. However, for high flow rates with Re = 7 200, the kink is the largest. The position of the kink does not change with changes in the flow rates and remains in the region of x = 75 mm to x = 115 mm.

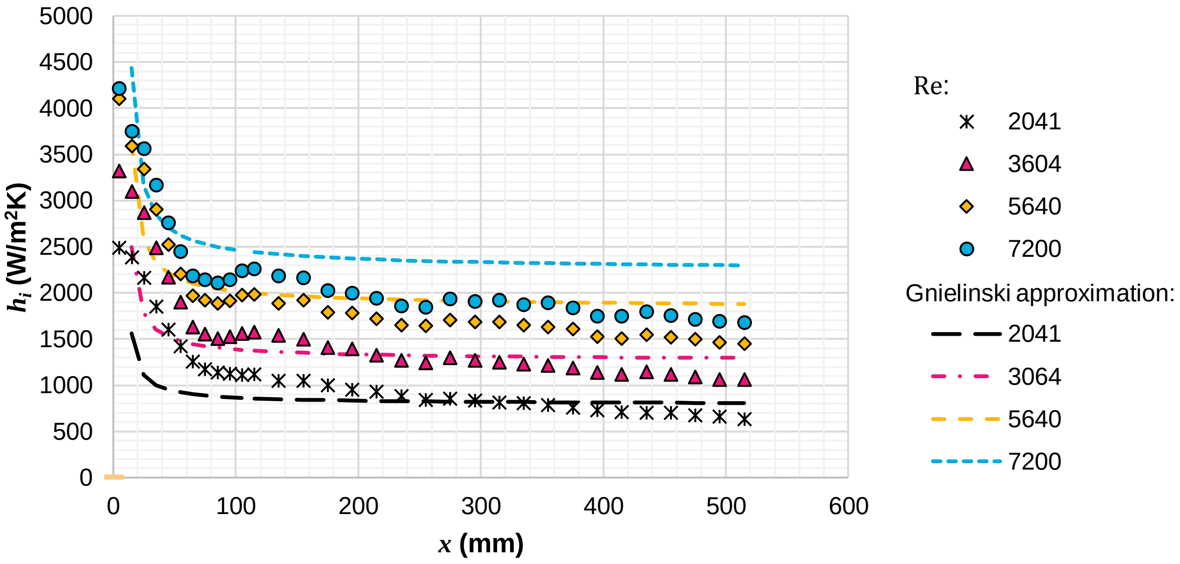

Figure 5-7: Local heat transfer coefficients for test case A and approximations by the correlation of Gnielinski (2009)

Considering the correlation developed by Gnielinski (2009) and the derived local heat transfer coefficients shown in Figure 5-7, it is evident that, for lower flow rates, the correlation under-predicts the local heat transfer rates at the inlet region. For higher flow rates, the correlation better predicts the heat transfer at the inlet region. Considering the local heat transfer coefficients for x > 200 mm, the correlation better predicts the heat transfer rates for developed flow for the low flow rates cases (Re = 2 041). For this region, the heat transfer is over-predicted for the high flow rate cases. This was not anticipated as the correlation of Gnielinski (2009) was developed for flow rate cases with Re > 10 000. The difference between the experimental and anticipated local heat transfer coefficient at x = 535 mm was 24.8%, 20.5%, 27% and 31.4% for the flow rate cases Re = 2 041, Re = 3 604, Re = 5 640 and Re = 7 200. The correlation of Gnielinski (2009) does not anticipate a gentle decreasing slope of local heat transfer coefficients, as captured by the experimental results.

As noted in Section 2.4, the correlations used to predict the heat transfer (Nu) in circular tubes is usually in the form of $\mathrm{Nu} = CRe^{y}\mathrm{Pr}^{z}$ where C, y and z are constants. The Prandtl number is a fluid property which varies with temperature. The inlet fluid temperatures for the experiments varied from 21.05 $^{\circ}\mathrm{C}$ to 21.5 $^{\circ}\mathrm{C}$, with associative inlet fluid Prandtl number range from 6.767 to 6.685. The drift in inlet temperatures has been accounted for as discussed in Section 4.10. For the different flow rates, the bulk fluid temperatures would increase at different rates depending on the flow rate for a constant heat flux. For the flow rate of Re ≈ 2000, the Prandtl number typically decreased by 0.103 over the length of 545 mm from the inlet. Similar for the flow rate case of Re ≈ 7500, the Prandtl number decreased by 0.028 for the same length. Water was the only fluid used in the experiments and thus the influence of other Prandtl number could not be investigated distinctively.

The influence of changing Prandtl number due to inlet fluid temperature drifts and bulk fluid temperature increases was investigated by computing the Chilton-Colburn J Factor, also known as the j factor. The j factor is calculated as $j = \mathrm{Nu}/\mathrm{RePr}^{1/3}$. In Figure 5-8, the Nu and j factor are plotted along the axial length of the flow passage. As seen the Nu and j factor follow the same trend.

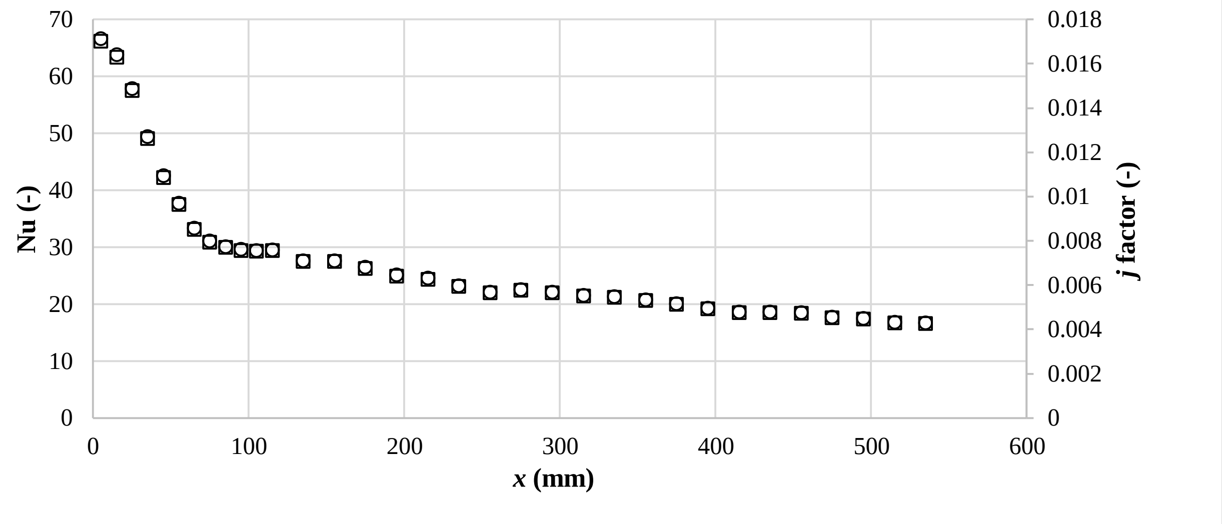

Figure 5-8: Nusselt number and j factor along axial length

As heat transfer in a concentric annular flow passage depends on a number of factors, such as diameter ratio, inlet configuration, flow regime and direction of heat transfer, it is difficult to develop a correlation with which to compare the local heat transfer coefficients. Thus, it is often useful to compare current findings to past experimental results. Figure 5-9 shows local heat transfer coefficients from studies by Peyghambarzadeh (2011), Van der Westhuizen et al. (2014) and Lee (1968).

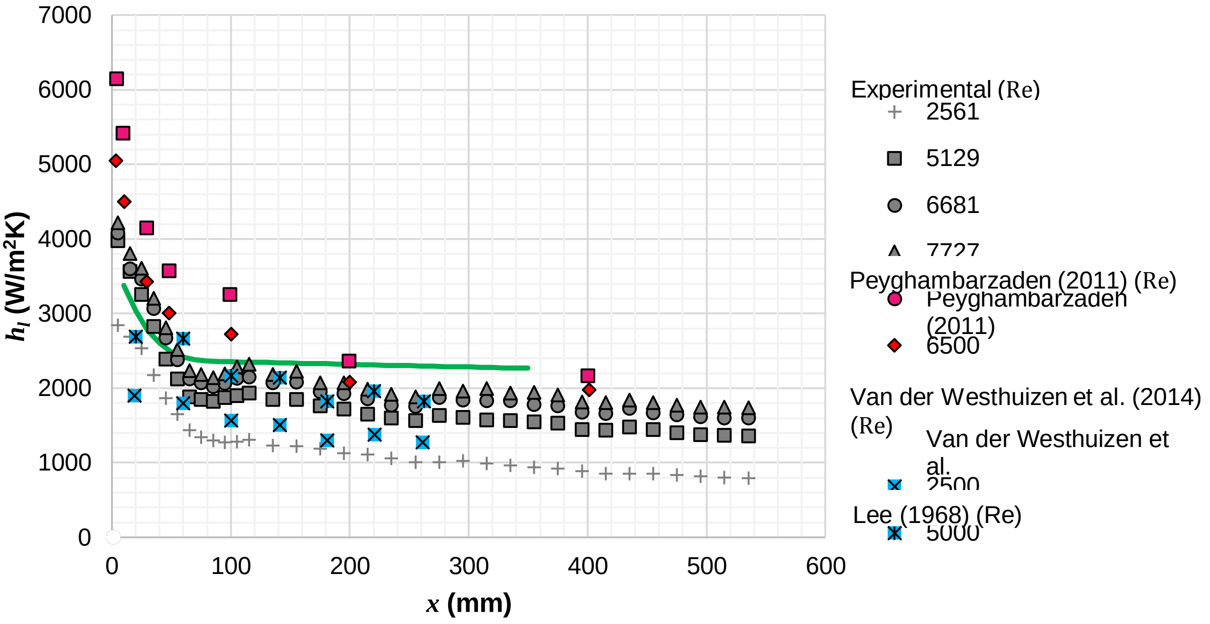

Figure 5-9: Local heat transfer coefficients compared to previous findings for heated annular/tube cases

The local heat transfer coefficients along the length of an annular flow passage from the current and previous investigations are plotted in Figure 5-9. The shown experimental results are from test case A, with the flow rates chosen to match those of past studies.

The experimental results of the Peyghambarzadeh (2011) study are shown in Figure 5-9. The author investigated the local Nusselt numbers of an electrically heated horizontal tube, with a hydraulic diameter of 5 mm and flow in the turbulent flow regime. For more information on this study, consult Section 2.5. The findings of Peyghambarzadeh (2011) show that the local heat transfer coefficients follow the same trend as the current investigation's experimental findings. Peyghambarzadeh (2011) presented two flow rates with Reynolds numbers of 6 500 and 8 500, of which the flow rate of 8 500 was outside the range for the current study. The experimental results will only be explicitly compared for the flow rate case for Re = 6 500.

The local heat coefficients of Peyghambarzadeh (2011) were up to 20% larger at the inlet region, compared to the ones found in the current study. Peyghambarzadeh's local heat transfer coefficients for the developed flow region (x > 150 mm) were up to 9% larger. The shape of local heat transfer coefficients also portrayed a kink at x = 100 mm. A similar kink can be seen in the results of the current investigation. Although the results of Peyghambarzadeh's study are related to a tube, the theory of boundary layer development remains the same and may be used as a reference to estimate the local heat transfer coefficients of an annular flow passage.

In the study of Van der Westhuizen et al. (2014), the local heat transfer coefficients of an annular flow passage were experimentally determined with temperature measured using TLCs. The flow rates of their study matched those of this study. Their annular flow passage had a hydraulic diameter of 0.54 compared to 0.65, as was used in this study. For more information on the study of Van der Westhuizen et al. (2014), please consult Section 2.6.5.

The local heat transfer coefficients derived from the study of Van der Westhuizen et al. (2014) were similar to those found in this investigation. For Van der Westhuizen et al. (2014), the flow rate case of Re = 2 500 as the local heat transfer coefficient was, on average, 10% larger than the ones found in the current investigation. For the flow rate case of Re = 5 000, the local heat transfer coefficients of Van der Westhuizen et al. (2014) were, on average, 11% larger than the ones found in the current investigation. Considering the shape of the local heat transfer coefficient numbers, Van der Westhuizen et al. (2014) did not capture the large decrease in local heat transfer coefficient along the flow passage length, as found by the other authors. This may be due to the density of their results.

If one considers the shape of the local heat transfer coefficient of Van der Westhuizen et al. (2014), one could interpret the local Nusselt number at x = 60 mm as the kink noted in the current investigation. However, not enough data points are available to make such an assumption.

In the numerical study of Lee (1968), the ratio of the local heat transfer coefficient to the overall heat transfer coefficient was derived for an annular flow passage by means of the momentum and heat transfer integral equations. The local heat transfer coefficient shown in Figure 5-9 was derived by assuming an overall heat transfer coefficient for the given flow rate and interpolating it to a Prandtl number of 6, as typically found in this study. Thus, only the shape of the local heat transfer coefficient of this study can be compared to the current investigation.

By comparing the findings of this investigation to those of past findings and an existing correlation, it is possible to say that the local heat transfer coefficient found in the current investigation follows the same general trend as the results of past studies.

5.4 Area-weighted average heat transfer for all test cases

In this section, the area-weighted average heat transfer are considered. These coefficients are considered for 545 mm of the flow passage, as measured from the inlet. These heat transfer coefficients are expressed as area weighted average Nusselt numbers were determined as discussed in Section 4.9, and the associative uncertainties were determined as described in Section 4.11.

The area-weighted Nusselt numbers for all the test cases were plotted against their Reynolds numbers in Figure 5-10. Please note that some experimental results were neglected as the bulk fluid inlet temperature drifted by a significant amount. It is evident from Figure 5-10 that the average Nusselt numbers increase as the annular flow rate is increased. For test cases A, B and C, the Nu_{avg} were similar in magnitude for Reynolds numbers between 2 000 and 4 000. However, deviations in Nu_{avg} were evident as the Reynolds numbers increased beyond 4 000.

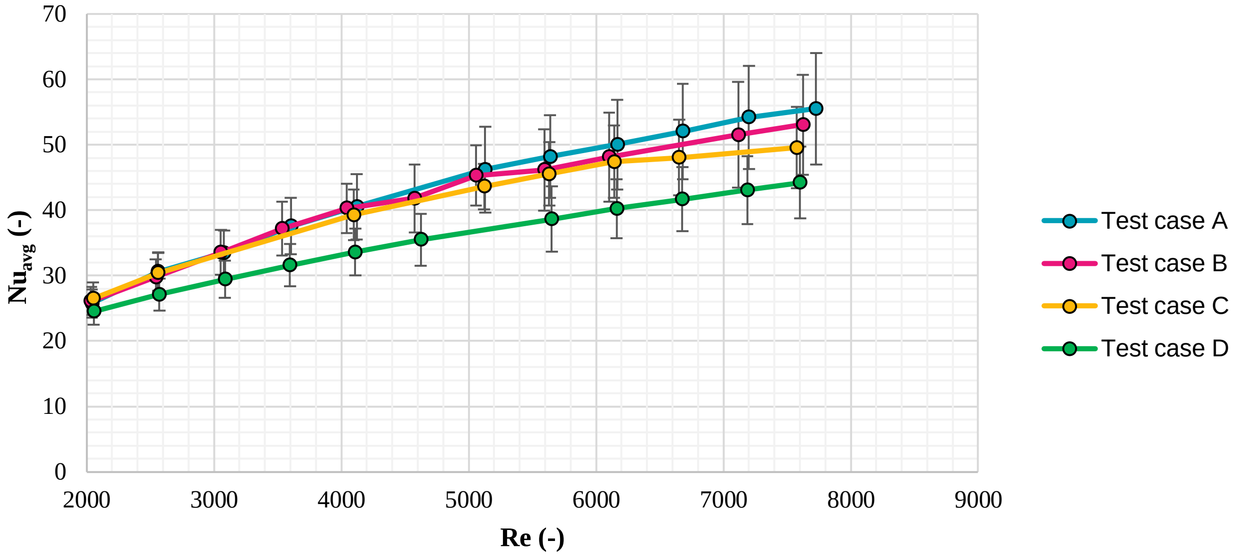

Figure 5-10: Area weighted average Nusselt numbers and associative uncertainties

For Reynolds numbers larger than 5 000, the inlet size has an influence on Nu_{avg}. Larger inlet sizes encourage higher heat transfer rates. The improvement in the Nu_{avg} is not significant, with a 5% improvement in heat transfer from test case B to test case A, and a 10% improvement from test case C to test case A for Reynolds numbers in the region of 7 700. Note that the Nu_{avg} for test cases A, B and C all fall within the same uncertainty band, which may suggest that the findings are inconclusive. The thermal resistance of the protective adhesive layer had the largest influence on the magnitude of the uncertainty. Since the protective layer was common to all cases, the relative magnitudes of the Nu_{avg} indicate the impact of the inlet size. As all test cases shared the same protective adhesive layer. Thus the influence of the uncertainty of the thermal resistance of the adhesive layer can be seen to be common between the test cases, which suggests that the uncertainty of the protective layer can be ignored between the test cases.

The area-weighted heat transfer for the swirl case, test case D, is smaller than test case C, which shared the same inlet size. A 5% to 23% reduction in area-weighted heat transfer was noted. Dirker et al. (2014) noted an increase in heat transfer for a swirl inlet to their test section, which comprised a rectangular micro channel without an inner wall (annulus). Their tests were run in the laminar and transitional flow regime, where the flow rates were in the turbulent flow regime, as shown in Section 5.6.

In the case of the study by Dirker et al. (2014), the swirl motion of the fluid encouraged the colder, denser fluid to be pushed against the heated outer wall of the micro channel due to the centrifugal forces of the swirling motion. The centrifugal force is the product of the particles mass and the angular acceleration. Thus, the particles with a lower density, higher mass will have a larger centrifugal force compared to warmer particles, lower density. Thus in the case of the current study, the centrifugal forces would again push the colder fluid towards the outer tube as they have a greater centrifugal force. This results in the in the warmer fluid being in the proximity of the inner tube of the flow passage.

With the presence of this warmer fluid near the heating rod, the surface temperature of the heating rod would be higher, resulting in higher TLC temperature readings. With higher temperature readings, the difference between the temperature of the wall and the bulk fluid would be larger. By consulting Equation 44 in Section 4.8, it is evident that a larger temperature difference between the wall and the bulk fluid would result in smaller heat transfer coefficients.

The inlet configuration of the study of Dirker et al. (2014) was in line with the flow passage. For the current study, the inlet was perpendicular to the annular flow passage, which resulted in a smaller impingement effect caused by the water entering the flow passage. This resulted in lower heat transfer coefficients.

The reduced impingement effect due to the warmer fluid near the heating rod caused lower heat transfer coefficients for an annular flow passage that is heated with the presence of fluid swirl.

Considering the shape of the Nu_{avg} over the Reynolds number range, it is apparent that the Nu_{avg} gradient decreases with increasing Reynolds numbers. It is as though the heat transfer coefficients reach an asymptotic level, after which the heat transfer coefficients do not increase with increasing Reynolds numbers.

5.5 Area-weighted average heat transfer coefficients compared to existing correlations

In this section, the experimental results of the area-weighted average Nusselt numbers are compared to the findings of previous studies. Heat transfer in annular flow passages depends on a number of factors, such as the diameter ratio, flow rate and the length of the flow passage, to name a few. This makes it difficult to gather previous experimental results with the same experimental conditions. Existing correlations make it easier to analyse and evaluate experimental findings. The experimental results for test cases A, B and C will be considered.

The area-weighted Nusselt numbers are compared to existing correlations and previous experimental results in Figure 5-11. The existing correlations were presented in Table 2-3. Experimental results from the study of Van der Westhuizen et al. (2014) were included due to similarities in the studies where TLCs were used for wetter surface temperature measurements. As seen from Figure 5-11, the correlation by McAdams (1954) predicts the highest heat transfer rates, followed by the correlation by Dittus and Boelter (1930) and Gnielinski (2009). The correlation by Dirker et al. (2004) anticipated the lowest heat transfer rates and is the most conservative correlation that was considered.

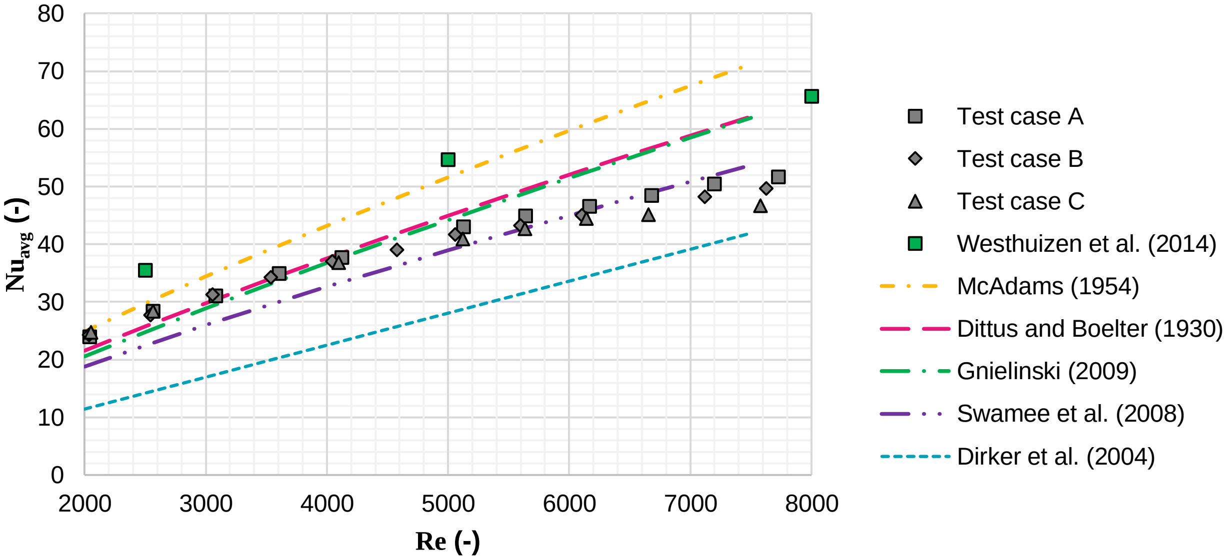

Figure 5-11: Comparison of experimental results and existing correlations

The experimental results follow the same general trend as the existing correlations. As the Reynolds numbers increased, so did the area-weighted average Nusselt numbers. However, as previously mentioned, for the higher Reynolds number cases, the Nusselt numbers from this investigation tend to reach a maximum, which results in a dip in the Nusselt numbers for higher flow rates, which is not anticipated by the existing correlations.

The correlation of Gnielinski (2009) and Swamee et al. (2008) best predict the area-weighted average Nusselt numbers for the flow rates investigated. For the lower flow rate cases with Reynolds numbers from 2 000 to 5 000, the correlations of Dittus and Boelter (1930), Gnielinski (2009), Dirker et al. (2004) and Swamee et al. (2008) under- predict the average Nusselt numbers. For Reynolds numbers from 5 000 to 6 000, the correlations of Swamee et al. (2008) accurately anticipated the heat transfer. For the higher end of the tests cases with Reynolds numbers from 5 500 to 7 700, the correlations over-estimated the experimentally obtained Nusselt numbers.

The overall Nusselt numbers from the results of the investigation of Van der Westhuizen et al. (2014) were considered and are shown in Figure 5-11. Their experimental results suggested higher Nusselt numbers (generally 31% to 36% higher) than those found in this investigation. Van der Westhuizen et al. (2014) associated large uncertainties with their experimental results, which could have led to their large heat transfer rates. Considering the shape of their overall Nusselt numbers vs Reynolds numbers, their experimental results also seem to dip as the Reynolds numbers increase and reach an asymptotic value, as noted in the experimental results of this investigation.

For this study, the area-weighted average Nusselt number for test case A, B and C are all calculated for the first 545 mm as measured from the inlet of the heat exchanger (limited by the photography mechanism used in the experimental facility). The entry length for the test cases are theoretically all the same for turbulent flow conditions as described in the book by Çengel and Ghajar (2011). If longer flow passages are considered, as for the cases by the other authors, the influence of the heat transfer in the inlet region would be smaller resulting in lower overall heat transfer coefficients.

5.6 Transition from laminar to turbulent flow conditions

The transition from laminar to turbulent flow was investigated with the experimental setup from a heat transfer perspective. Critical Reynolds numbers for annuli are seldom reported in literature and it was important to make sure that the results presented earlier were for turbulent flow regimes. Flow rates from Reynolds numbers of Re = 204 to Re = 7 727 were tested with 18 intermediate flow rate cases over two separate experimental runs. The transition from laminar flow to turbulent flow is of interest to researchers due to improvements in heat transfer without excessive heat loss. The work in this section was not the main focus of this investigation, thus the results will not be discussed in detail. Test cases A and E, for which the size of the inlet (D_3 = 20 mm) to the annular flow passage remained constant, were considered for this section.

The area-weighted average Nusselt numbers were plotted against their respective Reynolds numbers in Figure 5-12 on a logarithmic scale with base 10 for both axes. With this type of graph, the transition between the flow rates can easily be visualised by considering the different gradients of data. The experimental data from test cases A and E have been plotted in Figure 5-12, together with data from the heat transfer correlation for laminar flow by Morcos and Bergles (1975). Their correlation was added to visualise the typical gradient for laminar flow conditions. Their heat transfer correlation for laminar flow is given in Equation 49, where D was replaced with D_h to be suitable to an annular case.

$$\mathrm{Nu}_f = \left(4.36^2 + \left(0.145\left(\frac{\mathrm{Gr}^*\mathrm{Pr}^{1.35}}{Pw^{*0.25}}\right)^{0.265}\right)^2\right)^{0.5} \tag{49}$$

where $\mathrm{Gr}^* = g\beta\rho^2 D_h^4 q''/\mu^2 k$, $Pw^* = kD_h/k_w t$

In Equation 50, $\mathrm{Nu_f}$ refers to the fully developed Nusselt numbers, Gr^* refers to the modified Grashof number, Pr refers to the Prandtl number, and Pw^* refers to the modified tube wall parameter. The term Gr^* was calculated with g, which refers to the gravitation acceleration, D_h refers to the hydraulic diameter, q'' refers to the circumferential heat flux, and β, ρ, μ and k refer to the fluid volumetric expansion coefficient, density, dynamic viscosity and thermal conductivity respectively. The term Pw^* was calculated with previously mentioned terms and k_w, which refers to the thermal conductivity of the wall (304 stainless steel in this case), and $t,$ which refers to the tube wall thickness.

By considering the shape of the experimental data and the correlation by Morcos and Bergles (1975), it can be seen that three distinctive gradients are present. For the portion of the graph for which Re > 1 000, the gradient is the steepest, followed by the section for which 200 < Re < 1 000. The correlation noted in Equation 49 is for the overall Nusselt number for laminar flow. This correlation, together with the anticipated Nusselt numbers, has been added to Figure 5-12 to visualise the typical gradient for laminar flow. Experimental tests were only run to a minimum Reynolds number of 200. When considering the gradient of the correlation for laminar flow and the experimental data for 200 < Re < 1 000, the gradients are not the same, which suggests that the region for 200 < Re < 1 000 is in the transitional flow regime. The lower bound of this region could not be confirmed, as insufficient data was captured at lower Reynolds numbers. Turbulent flow was noted for Re > 1 000 and transitional flow in the Reynolds number range from 200 < Re < 1 000.

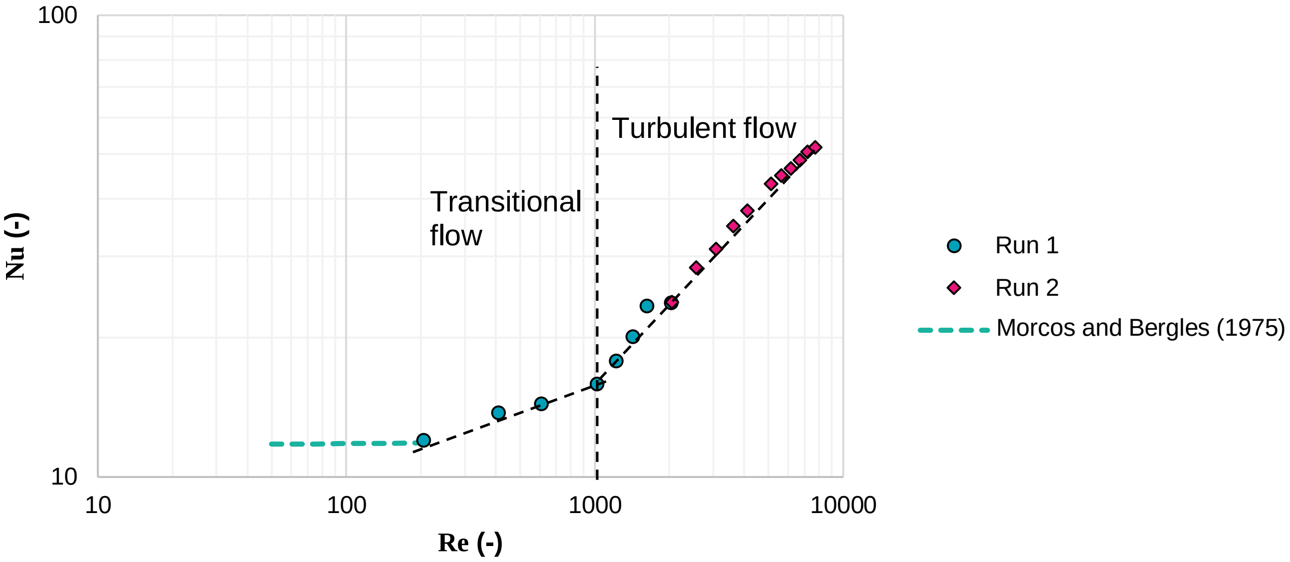

Figure 5-12: Overall Nusselt numbers against Reynolds numbers on a log-10 scale

The local heat transfer coefficients along the length of the annular flow passage are plotted in Figure 5-13 for a range of flow rate cases covering transitional and turbulent flow rate cases. It is evident that higher heat transfer rates were present for the cases with higher flow rates. For all flow rate cases, the heat transfer was at a maximum at the inlet region, which decreased due to the development of the boundary layers along the annular flow passage.

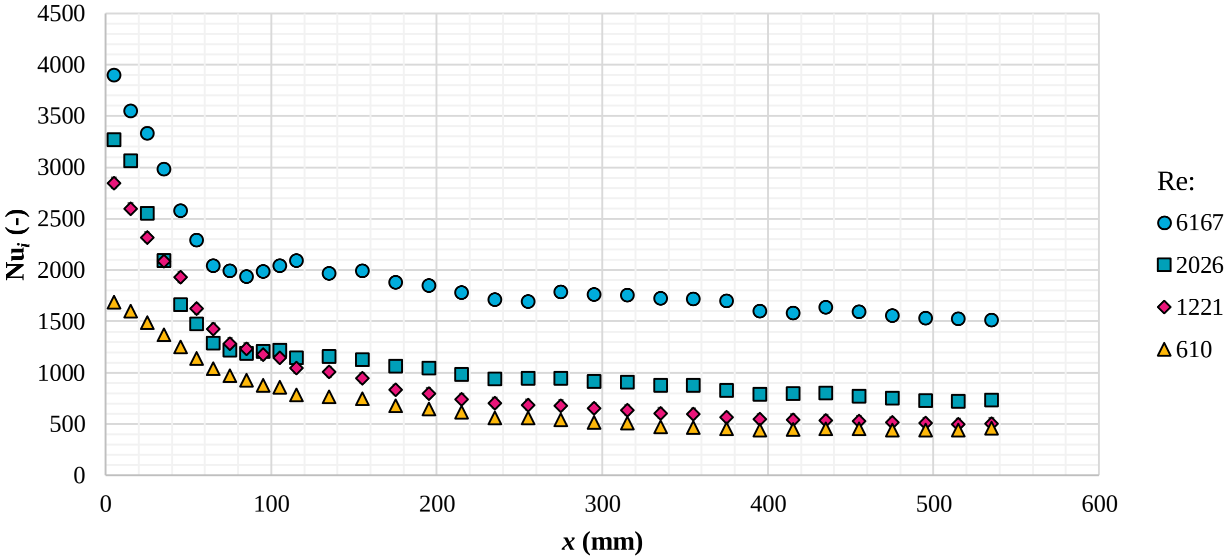

Figure 5-13: Local heat transfer coefficients for laminar, transitional and turbulent flow

The local Nusselt numbers along the length of the flow passage depict different shapes for different flow rate cases. For the flow rate cases with Re = 610 and Re = 1 221, the Nusselt numbers decrease smoothly from a maximum value at the inlet to a constant value. No bumps or uneven transitions are present. For the turbulent flow case, Re > 2 026, the Nusselt numbers do not decrease smoothly. Kinks, as well as local minimums and maximums were present, as discussed in Section 5.3. The transition from laminar to turbulent flow cannot be read off easily from Figure 5-13, and it is better visualised by considering the area-weighted average Nusselt numbers for the different flow rate cases.

5.7 Development of correlation for low turbulent flow state

This section deals with the development of a new heat transfer correlation that describes the experimental results of this investigation. As there is a gap in knowledge on heat transfer in the Reynolds number range from 2 000 to 10 000, the new correlation will optimise the design of short heat exchangers for many applications, including solar-driven power cycles, as discussed in Section 1.1. Considering all the heat transfer correlations from Table 2-1, Table 2-2 and Table 2-3, it was noted that the heat transfer in concentric annuli can usually be best described by Re, Pr, a,f, μ_b/μ_w or T_b/T_w and a factor considering the length of the flow passage, which is often noted as D_h/L.

Considering the factors noted above, it was decided to use the correlation developed by Gnielinski (2009)¸ tabulated in Table 2-3 as Equation 24, as a starting point from which the new correlation would be developed, as the correlation of Gnielinski (2009) contains the factors noted above in addition to a factor that considers the length of the flow passage (D_h/L). The correlation developed by Gnielinski (2009) was only valid for a flow rate state with Re > 10 000. However, as seen in Section 5.3 and Figure 5-11, the correlation anticipated the experimental results with relative accuracy in the flow rate ranges from Re = 2 000 to Re = 7 700. For more information on how the correlation of Gnielinski (2009) was developed, please consult Section 2.6.4.

The correlation developed by Gnielinski (2009) describes the overall heat transfer of concentric annuli of a particular length. To derive the local heat transfer coefficients, annular flow passages with lengths equal to the central locations of the sample areas (x = 5, 15, 25, 35….495, 515, 535 mm), the sample area lengths and the associative local heat transfer coefficients derived by means of the integral midpoint rule were considered.

The experimental local heat transfer coefficients are compared to the ones predicted by the correlation of Gnielinski (2009) for a number of flow rates in Figure 5-14. As seen from Figure 5-14, for low turbulent flow rate cases with Re < 5 500, the heat transfer is under-predicted at the inlet region. Further down the flow passage, x > 250 mm, the correlation tends to overestimate the heat transfer with a constant value, which was not captured by the experimental results. For the higher flow rate cases, Re > 5 500, the correlation predicted the heat transfer at the inlet region well. For the heat transfer further down the flow passage, the correlation over-predicts the heat transfer by up to 30%. A new correlation was developed to account for these variances at the inlet region for cases with low flow rates and the over-estimation of heat transfer for fully developed flow.

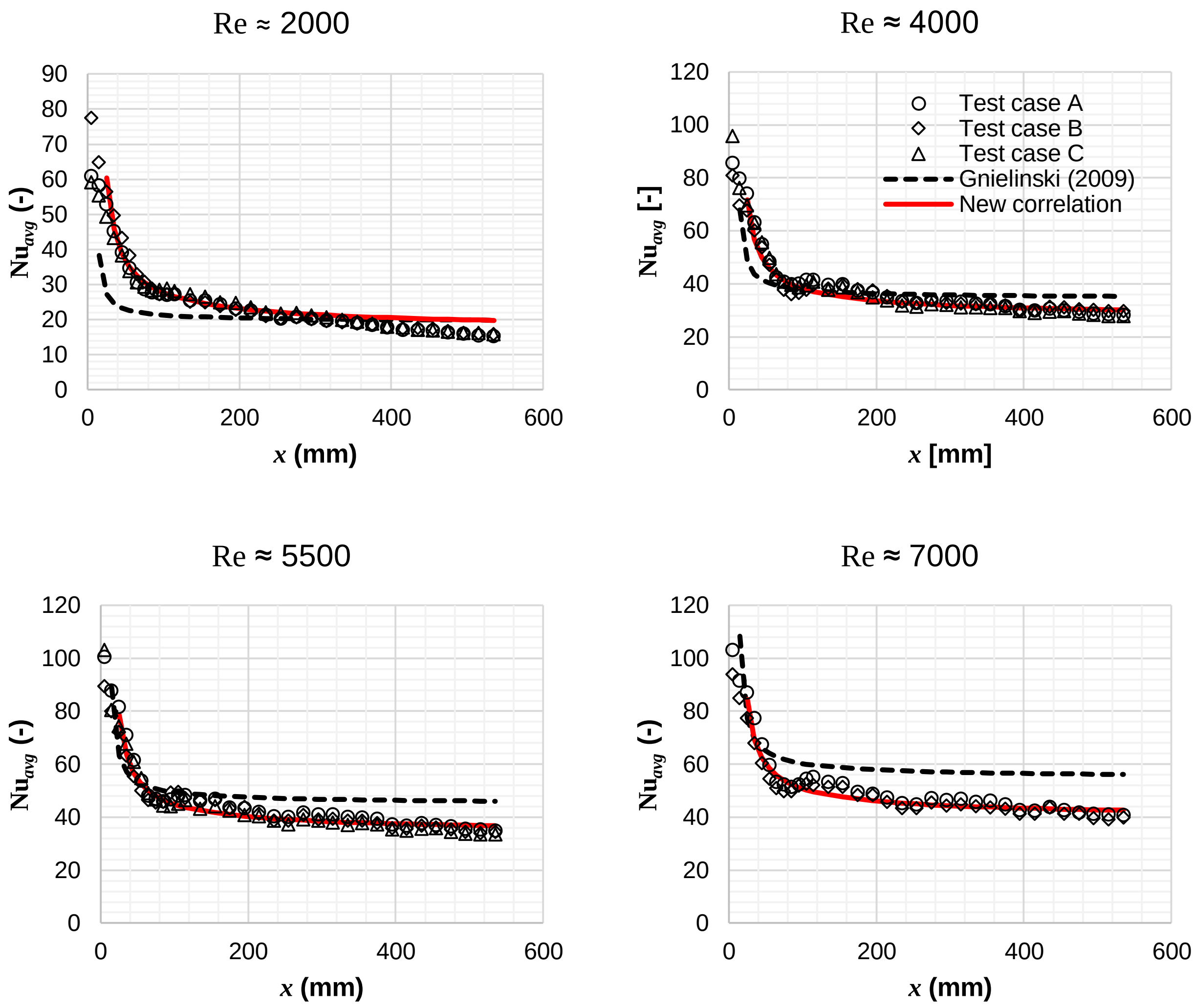

Figure 5-14: Local Nusselt numbers from experimental results, the developed correlation and the correlation developed by Gnielinski (2009)

Considering the correlation of Gnielinski (2009), an entrance correction factor derived by Hausen (1943) was added to account for the increased heat transfer at the entrance region. The correction factor derived by Hausen (1943) was $\left(1+\left(\frac{d_h}{L}\right)^{\frac{2}{3}}\right)$. To better predict the experimental results, this entrance correction factor was adapted to be $\left(1+\left(\gamma\frac{d_h}{L}\right)^{\frac{2}{3}}\right)$, where $\gamma = 32700/\mathrm{Re}$. This value of β was determined by means of optimisation and reducing the value of the root means square error. By adapting this entrance region factor, the heat transfer in the fully developed region was still over-predicted.

In the correlation of Gnielinski (2009), the term $\varphi = 1.07 + \frac{900}{Re_{D_h}} - \frac{0.63}{1+10Pr_a}$, as developed by Petukhov and Kirillov (1958), is used. This term, φ, was altered to better predict the heat transfer in the fully developed region of the experimental results in this investigation. The term was altered to $\varphi = 2.04 + \frac{14\,500}{Re_{D_h}} - \frac{0.63}{1+10Pr_a}$. This adaptation to φ reduced the predicted heat transfer. The new correlation and its approximated local heat transfer coefficients are plotted in Figure 5-14. It is evident that the new proposed correlation better predicts the local Nusselt numbers for cases with high and low flow rates for the entire region of interest. It must be noted that the equation is only valid for cases in which the flow passage length is greater than 20 mm.

The area-weighted average Nusselt numbers against the Reynolds numbers are plotted in Figure 5-15 with past experimental results from Van der Westhuizen et al. (2015) together with the correlations by Swamee et al. (2008), Gnielinski (2009) and Dirker and Meyer (2005). The comparison of the correlations has been discussed in Section 5.5. As seen from Figure 5-15, the new correlation predicts the overall Nusselt numbers better. The new correlation captures the Nusselt number dip with increasing annular flow rates, as noted by the experimental results.

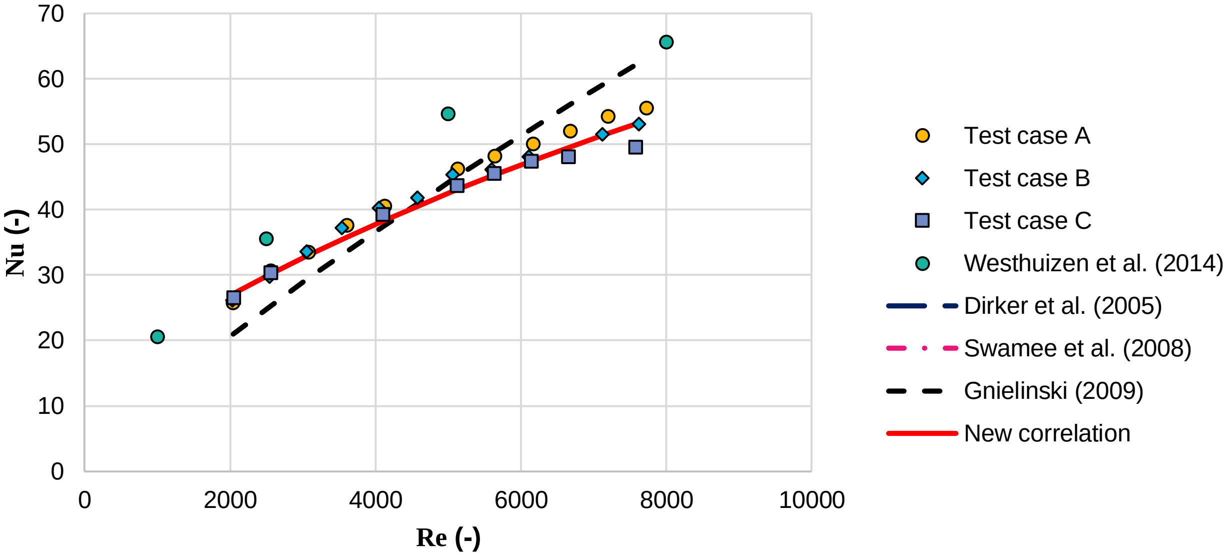

Figure 5-15: Overall Nusselt numbers from the experimental results and the newly developed correlation

The Nusselt number predictions by the new correlation are plotted against the experimental Nusselt numbers in Figure 5-16. As seen in this figure, the predictions all fall within the 10% error bands. The average percentage error with reference to the experimentally determined value was 2.7% and the standard deviation was 2.49%. This aids in reaching the conclusion that the new correlation successfully captures the experimental results.

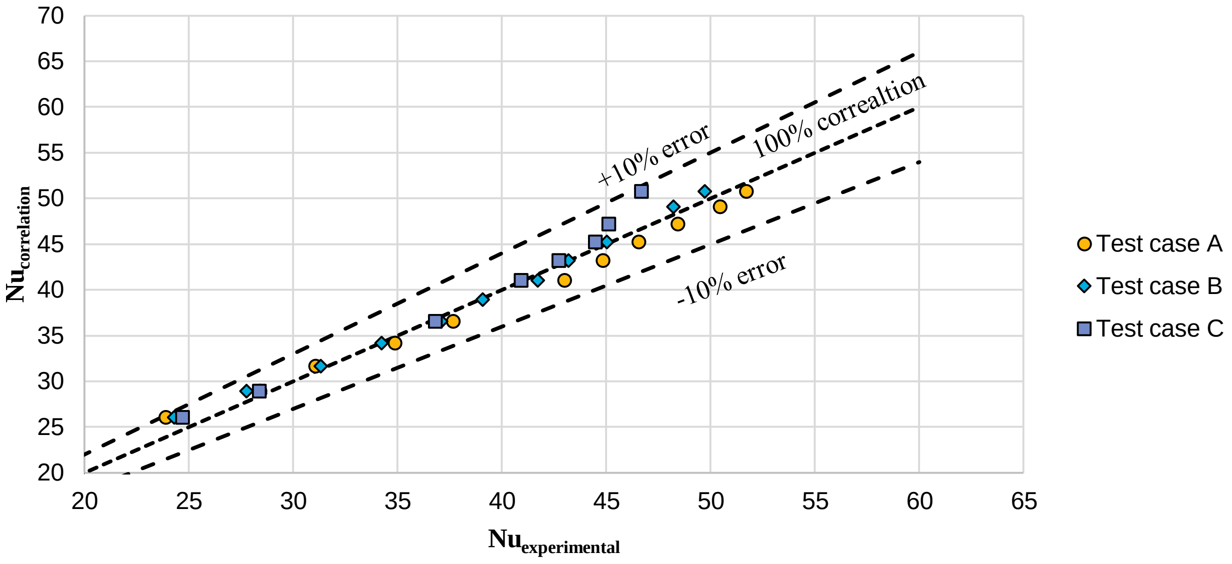

Figure 5-16: Predictions of correlations and error bands

The new proposed correlation is therefore:

$$Nu_{D_h} = \frac{\left(\frac{f}{8}\right) Re_{D_h} \mathrm{Pr_a}}{\varphi + 12.7\sqrt{\left(\frac{f}{8}\right)}\left(Pr_a^{\frac{2}{3}} - 1\right)}\left(1 + \left(\gamma \frac{D_h}{L}\right)^{2/3}\right) F_{ann} K$$

$$\gamma = \frac{32\ 700}{Re}$$

$$\varphi = 2.04 + \frac{14\ 500}{Re_{D_h}} - \frac{0.63}{1 + 10Pr_a}$$

$$K = \left(\frac{Pr_a}{P_{riw}}\right)^{0.11}$$

$$F_{ann} = 0.75a^{-0.17}$$

$$f = (1.8\log_{10} Re^* - 1.5)^{-2}$$

$$Re^* = Re_{D_h}\frac{(1 + a^2)lna + (1 - a^2)}{(1 - a)^2 \ln a}$$

The limitations of this correlation are that the flow rate state must be 2 000 < Re < 7 500, and L > 20 mm.

5.8 Summary of experimental results

In this section, the experimental results captured from the experiments were presented and discussed. The local temperature measurements were discussed. The local heat transfer coefficients were presented from which boundary layer development can be approximated. A kink in the local heat transfer coefficients was captured at the location at which the boundary layers merge, which has not been captured in detail by previous authors. The local heat transfer coefficients coincide with experimental data from other authors.

Considering the area-weighted average heat transfer coefficients, no improvements in heat transfer was seen for the different inlet sizes with flow rates for Reynolds numbers smaller than 4 000. However, for flow rates larger than 5 000, a larger inlet is favoured for higher heat transfer rates. For test case D and induced swirl, lower area-weighted average heat transfer coefficients were captured compared to the on-axis inlet types. The correlation developed by Gnielinski (2009) best describes the area-weighted average heat transfer coefficients. However, a maximum heat transfer capability of the heat exchanger seemed to be achieved at the higher end of the flow rate cases.

The change from transitional to turbulent flow was also visualised with the area-averaged heat transfer coefficients. A distinct transition was visible for Reynolds numbers of 1 000, which was regarded as the transition from transitional flow to turbulent flow. Distinctively different local heat transfer coefficient shapes were visible along the length of the flow passage.

A new correlation was developed to anticipate the heat transfer of an annular flow passage. The correlation was adapted from literature to better predict heat transfer at the inlet region for low flow rate cases and developed for high flow rate cases. The new correlation predicted the area-weighted heat transfer coefficients within 10% and with an average error of 2.7% based on the experimental values.

6. Summary, conclusion and recommendations

6.1 Summary

Local heat transfer coefficients were captured for the inlet region of a concentric annular flow passage by means of temperature measurements made by TLC. The absence of boundary layers at the inlet region of a concentric tube heat exchanger results in an increase in heat transfer ability. Due to difficulties in measuring the local heat transfer coefficients at the inlet region of an annular flow passage, little experimental data and correlations are available to describe heat transfer during boundary layer development. The influence of the size of the inlet with on- and off-axis inlets has not been studied before and was investigated.

The inner tube of the annular flow in this study consisted of a constant heat flux heating rod to reduce the levels of uncertainty in measuring the bulk fluid temperature of the inner tube. TLCs were applied to the outer surface of the heating rod and had to be protected from the fluid in the annular flow passage by a protective adhesive layer. The temperature difference of the protective layer had to be determined, as it acted as a thermal interface between the wetted surface of the heating rod and the TLCs. An imaging mechanism was built to autonomously capture the temperature response of the TLC surface. These images were cropped, converted from hue to temperature and stitched together to produce a detailed wall temperature field.

The detailed wall temperature fields gave an indication of fluid flow for the different inlets studied in this investigation. Local heat transfer coefficients were derived from the wall temperatures and gave an indication of boundary layer development. The local heat transfer coefficients decreased from a maximum at the inlet to a minimum steady value beyond fully developed flow. A kink with local maximum and minimum values for the heat transfer coefficients was noted at the location at which the boundary layers merge in higher turbulent test cases. The largest source of uncertainty for this investigation was the thermal resistance of the protective adhesive layer.

The local heat transfer coefficients from this investigation were in agreement with those captured in previous studies and predicted local heat transfer coefficients derived from existing correlations for turbulent flow in an annular flow passage.

The size of the inlet does not have a major influence on the overall heat transfer in cases with a low flow rate and Reynolds numbers between 2 000 and 4 000. For cases with a high flow rate, a large inlet, which leads to higher overall heat transfer coefficients, is favoured. The results from this investigation followed the trends of existing correlations, however, a dip in the gradient for overall

Nusselt numbers as opposed to Reynolds numbers was noted when the Reynolds number is larger than 5 000. A new correlation was developed to better suit the experimental data based on literature. The new correlation estimated the area-weighed heat transfer coefficients noted in this study to within 10%. Different test cases were tested to study the effect of different inlet sizes on heat transfer in a heat exchanger.

Low to high flow rates were investigated to identify the transition from laminar to turbulent flow. Differences were noted in the shapes of the local heat transfer coefficient for the transitional and turbulent flow regimes.

6.2 Recommendations

This section deals with recommendations made to future researchers who use TLCs to study heat transfer in a concentric annular flow passage.

The largest source of uncertainty for this investigation was the protective adhesive layer's thermal resistance. An alternative way to protect TLCs from the fluid in the annuli may be sourced. The author made an effort to identify possible means of protecting the crystals. A protective adhesive layer proved to be most successful in protecting the TLCs. The thermal resistance of the protective adhesive layer was determined by experimentation. The uncertainty in determining the thermal resistance was 8.81%, which was the largest contributor to the experiment's uncertainty. This uncertainty may be reduced by other means to determine the thermal resistance.

The transition from laminar to turbulent flow was briefly investigated. LCT proved to be a viable testing method to investigate this transition. Future tests may implement LCT to test the transition from laminar to turbulent flow.

Due to the high accuracy of the temperature fields and local heat transfer coefficients, which may be derived from the tests, LCT may be implemented to study the effect of different passive flow components, inlet configurations and annular ratios.

Some of the photos at the inlet region were either directly blocked by the inlet of the annulus or shadows were cast over the TLC surface. For future investigations, the TLC surface with the shadows may be calibrated so that more of the surface at the inlet may be investigated. This will reduce some of the uncertainty at the inlet region.

In future investigations, additional cameras may be mounted to the mechanism to increase the rate at which data is captured from the experiment. This will reduce the effect that the changing inlet water temperature will have and provide more accurate experimental results.

This work paved the way for future investigations with TLCs in concentric tube heat exchangers.

To investigate the validity of the developed correlation, additional experiments can preformed, at different heat fluxes. The influence of different heat fluxes should be negligible and should yield the similar results. Larger heat fluxes could result in larger temperature difference potentials reducing the uncertainties of the experiments.

6.3 Conclusion

Detailed local heat transfer coefficients were captured at the inlet region of an annular flow passage by surface temperature measurements made by means of TLCs. The local heat transfer coefficients derived were in agreement with past experimental results and proved to be more detailed. These detailed results allowed the author to study the development of the boundary layers in more detail. Different inlet configurations were investigated, with the results of the investigation suggesting that, with in-line inlet configurations, larger inlets are favoured for flow rates with Reynolds numbers larger than 5 500. With flow rates in the low turbulent flow regime with Reynolds numbers smaller than 5 500, the size of the inlets does not have an influence on the area-weighted average heat transfer coefficients. With the off-axis inlet configuration, lower heat transfer coefficients were present. The transition from a laminar to a turbulent flow regime was investigated from a heat transfer perspective with the transition from transitional flow to turbulent flow present at Reynolds numbers of 1 000. A new heat transfer correlation was developed to account for boundary layer development that captured all the area-weighted heat transfer coefficients for all test cases within 10%.

7. References

BADUS'HAQ, R. F. 1993. Forced-convection heat transfer in the entrance region of pipes. *International Journal of Heat and Mass Transfer,* 36**,** 3343-3349.

BHATTI, M. & SHAH, R. 1987. Turbulent and transition flow convective heat transfer in ducts. *Handbook of single-phase convective heat transfer***,** 4.1-4.166.

CALLISTER, W. D. & RETHWISCH, D. G. 2007. *Materials science and engineering: an introduction*, Wiley New York.

CAMCI, C. 1996. Introduction to liquid crystal thermography and a brief review of past studies. *THE PENNSYLVANIA STATE UNIVERSITY*.

CAMCI, C. 2008. Introduction to liquid crystal thermography and a brief review of past studies. 12.

ÇENGEL, Y. A. & GHAJAR, A. J. 2011. *Heat and mass transfer: fundamentals & applications*, McGraw-Hill.

COLBURN, A. P. 1933. A method of correlating forced convection heat transfer data and a comparison with fluid friction. *Trans Am Inst Chem Eng,* 29**,** 174-210.

COLEBROOK, C. F. 1939. Turbulent flow in pipes, with particular reference to the transition region between the smooth and rough pipe laws. *Journal of The Ice,* 11**,** 133-156.

DIRKER, J. & MEYER, J. P. 2005. Convective heat transfer coefficients in concentric annuli. *Heat Transfer Engineering,* 26**,** 38-44.

DIRKER, J., MEYER, J. P. & GARACH, D. V. 2014. Inlet flow effects in micro-channels in the laminar and transitional regimes on single-phase heat transfer coefficients and friction factors. *International Journal of Heat and Mass Transfer,* 77**,** 612-626.

DIRKER, J., VAN DER VYVER, H. & MEYER, J. P. 2004. Convection heat transfer in concentric annuli. *Experimental Heat Transfer,* 17**,** 19-29.

DITTUS, F. W. & BOELTER, L. M. K. 1930. Heat transfer in automobile radiators of the tubular type. *University of California Publications on Engineering,* 2**,** 443-461.

DUNN, P. F. 2014. *Measurement and data analysis for engineering and science*, CRC press.

EVERTS, M. 2015. Heat Transfer and Pressure Drop of Developing Flow in Smooth Tubes in the Transitional Flow Regime.

GASLJEVIC, K. & MATTHYS, E. 1997. Experimental investigation of thermal and hydrodynamic development regions for drag-reducing surfactant solutions. *Transactions-American society of mechanical engineers journal of heat transfer,* 119**,** 80-88.

GEANKOPLIS, C. J. 1993. *Transport Processes and Unit Operations,* 3rd.

GHAJAR, A. J. & TAM, L.-M. 1994. Heat transfer measurements and correlations in the transition region for a circular tube with three different inlet configurations. *Experimental Thermal and Fluid Science,* 8**,** 79-90.

GNIELINSKI, V. 1976. New equations for heat and mass transfer in turbulent pipe and channel flow. *Int. Chem. Eng.,* 16**,** 359-368.

GNIELINSKI, V. 2009. Heat transfer coefficients for turbulent flow in concentric annular ducts. *Heat Transfer Engineering,* 30**,** 431-436.

HALLCREST 2014a. *Handbook of Thermochromic Liquid Crystal Technology,* 1911 Pickwick Lane, Glenview, IL 60026, LCR Hallcrest.

HALLCREST 2014b. TLC products for use in research and testing applications_ Hallcrest. *In:* HALLCREST (ed.) RT001 Rev 01 ed. Glenview: Hallcrest.

HALLQUIST, M. 2011. *Heat transfer and pressure drop characteristics of smooth tubes at a constant heat flux in the transitional flow regime.* University of Pretoria.

HAUSEN, H. 1943. Darstellung des warmeuberganges in rohren durch verallgemeinerte potenzbeziehungen. *Z. VDI Beih. Verfahrenstech,* 4.

LAM, C., TAM, L., TAM, H. & KUOK, C. 2013. Heat Transfer Measurements for the Horizontal Micro-Tubes Using Liquid Crystal Thermography. *Advanced Materials Research,* 816**,** 166-169.

LEE, Y. 1968. Turbulent heat transfer from the core tube in thermal entrance regions of concentric annuli. *International Journal of Heat and Mass Transfer,* 11**,** 509-522.

MARANZANA, G., PERRY, I. & MAILLET, D. 2004. Mini- and micro-channels: influence of axial conduction in the walls. *International Journal of Heat and Mass Transfer,* 47**,** 3993-4004.

MCADAMS, W. H. 1954. Heat Transmission. *3rd New York*.

MEYER, J. P. Heat transfer in tubes in the transitional flow regime. Proceedings of the 15th International Heat Transfer Conference, Kyoto, paper KN03, 2014. 11-15.

MEYER, J. P. & OLIVIER, J. 2011. Transitional flow inside enhanced tubes for fully developed and developing flow with different types of inlet disturbances: Part II–heat transfer. *International Journal of Heat and Mass Transfer,* 54**,** 1598-1607.

MOFFAT, R. J. 1988. Describing the uncertainties in experimental results. *Experimental thermal and fluid science,* 1**,** 3-17.

MOHAMMED, H. A. 2009. The effect of different inlet geometries on laminar flow combined convection heat transfer inside a horizontal circular pipe. *Applied Thermal Engineering,* 29**,** 581-590.

MORCOS, S. & BERGLES, A. 1975. Experimental investigation of combined forced and free laminar convection in horizontal tubes. *Journal of Heat Transfer,* 97**,** 212-219.

MUWANGA, R. & HASSAN, I. 2006. Local heat transfer measurements in microchannels using liquid crystal thermography: methodology development and validation. *Journal of Heat Transfer,* 128**,** 617-626.

NUSSELT, W. 1931. Der Wärmeaustausch zwischen Wand und Wasser im Rohr. *Forschung auf dem Gebiet des Ingenieurwesens A,* 2**,** 309-313.

OGDEN, T. R. & HENDRICKS, E. W. 1984. Liquid crystal thermography in water tunnels. *Experiments in Fluids,* 2**,** 65-66.

PETUKHOV, B. S. 1970. Heat Transfer and Friction in Turbulent Pipe Flow with Variable Physical Properties. *Advances in Heat Transfer.*

PETUKHOV, B. S. & KIRILLOV, V. V. 1958. On heat exchange at turbulent flow of liquid in pipes. *Teploenergetika,* 4**,** 63-68.

PEYGHAMBARZADEH, S. 2011. Forced Convection Heat Transfer in the Entrance Region of Horizontal Tube under Constant Heat Flux. *World Applied Sciences Journal,* 15**,** 331-338.

PIASECKA, M. 2013. Determination of the temperature field using liquid crystal thermography and analysis of two-phase flow structures in research on boiling heat transfer in a minichannel. *Metrology and Measurement Systems,* 20**,** 205-216.

POPIEL, C. & WOJTKOWIAK, J. 1998. Simple formulas for thermophysical properties of liquid water for heat transfer calculations (from 0 C to 150 C). *Heat transfer engineering,* 19**,** 87-101.

PRANDTL, L. 1942. Führer durch die Strömungslehre. *Führer Durch Die Strömungslehre*.

PRINSLOO, F. P., DIRKER, J. & MEYER, J. P. Heat transfer and pressure drop characteristics in the annuli of tube-in-tube heat exchangers (horizontal lay-out). Proceedings of the 15th International Heat Transfer Conference, Kyoto, paper IHTC15-9225, 2014. 11-15.

QUARMBY, A. 1967. Some measurements of turbulent heat transfer in the thermal entrance region of concentric annuli. *International Journal of Heat and Mass Transfer,* 10**,** 267-276.

RAO, Y. & XU, Y. 2012. Liquid crystal thermography measurement uncertainty analysis and its application to turbulent heat transfer measurements. *Advances in Condensed Matter Physics,* 2012.

RAO, Y. & ZANG, S. 2010. Calibrations and the measurement uncertainty of wide-band liquid crystal thermography. *Measurement Science and Technology,* 21.

SABATINO, D. R., PRAISNER, T. J. & SMITH, C. R. 2000. A high-accuracy calibration technique for thermochromic liquid crystal temperature measurements. *Experiments in Fluids,* 28**,** 497-505.

SIEDER, E. N. & TATE, G. E. 1936. Heat transfer and pressure drop of liquids in tubes. *Industrial & Engineering Chemistry,* 28**,** 1429-1435.

SMITH, C. R., SABATINO, D. R. & PRAISNER, T. J. 2001. Temperature sensing with thermochromic liquid crystals. *Experiments in Fluids,* 30**,** 190-201.

STASIEK, J., JEWARTOWSKI, M. & KOWALEWSKI, T. A. 2014. The Use of Liquid Crystal Thermography in Selected Technical and Medical Applications—Recent Development. *Journal of Crystallization Process and Technology,* 4**,** 46-59.

STASIEK, J. A. & KOWALEWSKI, T. A. 2002. Thermochromic liquid crystals applied for heat transfer research. *Opto-electronics Review,* 10**,** 1-10.

SWAMEE, P. K., AGGARWAL, N. & AGGARWAL, V. 2008. Optimum design of double pipe heat exchanger. *International Journal of Heat and Mass Transfer,* 51**,** 2260-2266.

TAM, L.-M. & GHAJAR, A. J. 1997. Effect of inlet geometry and heating on the fully developed friction factor in the transition region of a horizontal tube. *Experimental thermal and fluid science,* 15**,** 52-64.

VAN DER WESTHUIZEN, J. E., DIRKER, J. & MEYER, J. P. 2014. Investigation into using liquid crystal thermography as primary temperature measurement technique for obtaining local wall temperatures and heat transfer coefficients in tube-in-tube heat exchangers.

VAN DER WESTHUIZEN, J. E., DIRKER, J. & MEYER, J. P. 2015. Implementation of Liquid Crystal Thermography to Determine Wall Temperatures and Heat Transfer Coefficients in a Tube-in-tube Heat Exchanger. *Experimental Heat Transfer*.

VAN ZYL, W. R., DIRKER, J. & MEYER, J. P. 2013. Single-phase convective heat transfer and pressure drop coefficients in concentric annuli. *Heat Transfer Engineering,* 34**,** 1112-1123.

Appendices

Appendix A. Axial heat conduction, M-factor

To consider the axial conduction of the heating rod, the following calculation was performed to determine the M-factor of the heating rod in the worst-case scenario.

Heat transfer by conduction:

As heat is transferred in the bright steel rod, aluminium powder and stainless steel rod, the combined heat transfer by conduction needs to be considered.

$$\dot{Q}_{cond} = \dot{Q}_{BS} + \dot{Q}_{AL} + \dot{Q}_{SS}$$

$$\dot{Q}_{BS}, \dot{Q}_{AL}, \dot{Q}_{SS} = \frac{k_s A_s}{L_s} \Delta T_s$$

$\dot{Q}_{BS}$	$\dot{Q}_{AL}$	$\dot{Q}_{SS}$
$k = 50.2\ W/mK$ $d_i = 0\ m$ $d_o = 0.012\ m$ $L = 1\ m$ $\therefore A = 0.000113\ m^2$ $\dot{Q}_{BS} = \frac{kA}{L}\Delta T$ $\dot{Q}_{BS} = 0.005971\ W/K$	$k = 273\ W/mK$ $d_i = 0.0154\ m$ $d_o = 0.02187\ m$ $L = 1\ m$ $\therefore A = 0.000189\ m^2$ $\dot{Q}_{AL} = \frac{kA}{L}\Delta T$ $\dot{Q}_{AL} = 0.040784\ W/K$	$k = 16.2\ W/mK$ $d_i = 0.02187\ m$ $d_o = 0.02667\ m$ $L = 1\ m$ $\therefore A = 0.000183\ m^2$ $\dot{Q}_{SS} = \frac{kA}{L}\Delta T$ $\dot{Q}_{SS} = 0.003121\ W/K$
$\dot{Q}_{cond} = \dot{Q}_{BS} + \dot{Q}_{AL} + \dot{Q}_{SS}$ $\dot{Q}_{cond} = 0.049875\ W/K$		

Total heat transfer by heating rod:

$\dot{Q}_{tot} = \dot{m}Cp_f\Delta T_f$

$$\dot{m} = 0.108\ kg/s$$

$$Cp = 4\,180\ J/kgK$$

$\dot{Q}_{tot} = 451.44\ W/K$

Now calculating the M-value, assuring that $\Delta T_s = \Delta T_f$

$$M = \frac{\dot{Q}_{conduction}}{\dot{Q}_{tot}}$$

$$M = 0.011\% < 1\%$$

Thus, the axial conduction will be insignificant. Even for the case for Re = 200, the M-value was less than 1%.

Appendix B. Thermocouple calibration curves

This section contains the calibration curves of the 16 thermocouples used to measure the inlet and outlet temperatures of the bulk fluid in the annulus. Eight thermocouples were placed at the inlet and outlet respectively. The thermocouples were calibrated with a PT100, which has an uncertainty of 0.1 ˚C. Separate calibration curves that detail the error of measurement prior to and after calibration can be seen below.

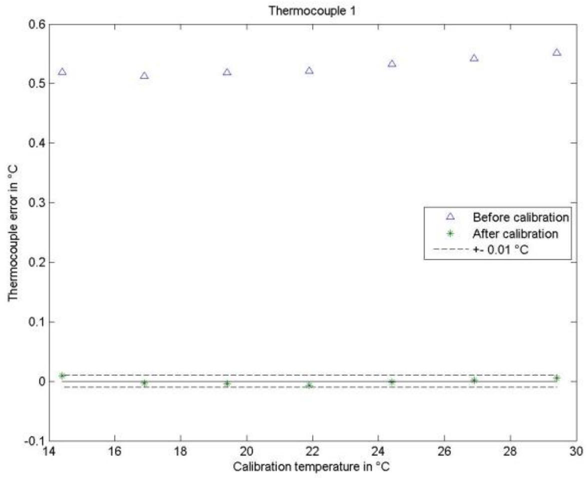

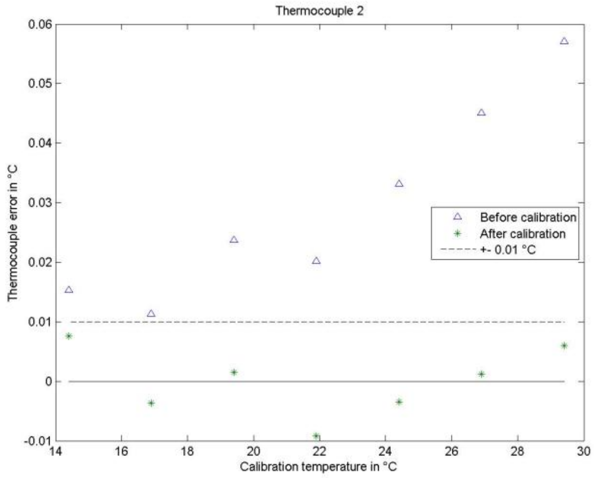

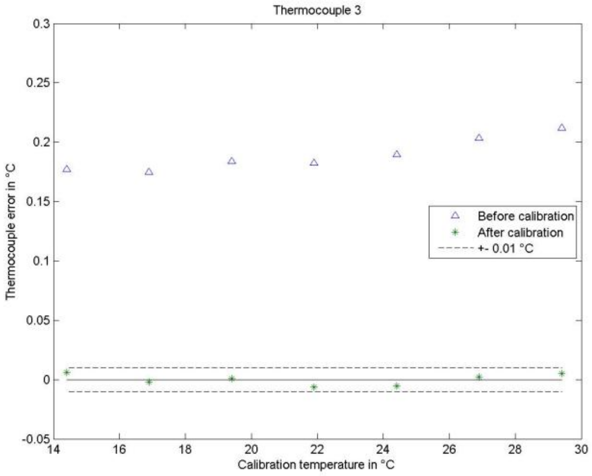

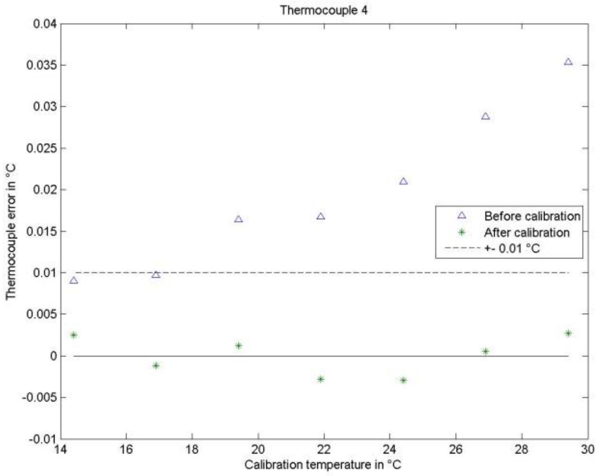

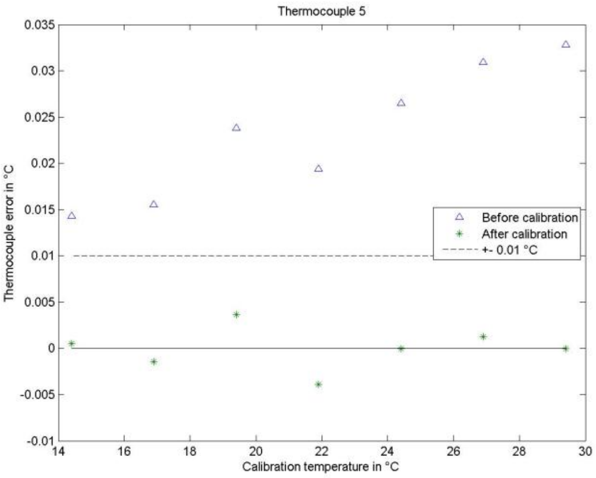
Thermocouple 5
0.035
0.03
0.025
0.02
0.015
0.01
0.005
0
-0.005
-0.01
Thermocouple error in °C
14
16
18
20
22
24
26
28
30
Calibration temperature in °C
Before calibration
After calibration
+- 0.01 °C

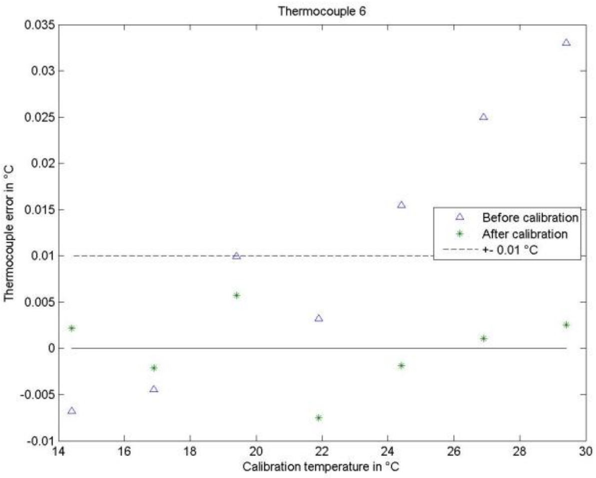
Thermocouple 6
0.035
0.03
0.025
0.02
0.015
0.01
0.005
0
-0.005
-0.01
Thermocouple error in °C
14
16
18
20
22
24
26
28
30
Calibration temperature in °C
Before calibration
After calibration
+- 0.01 °C

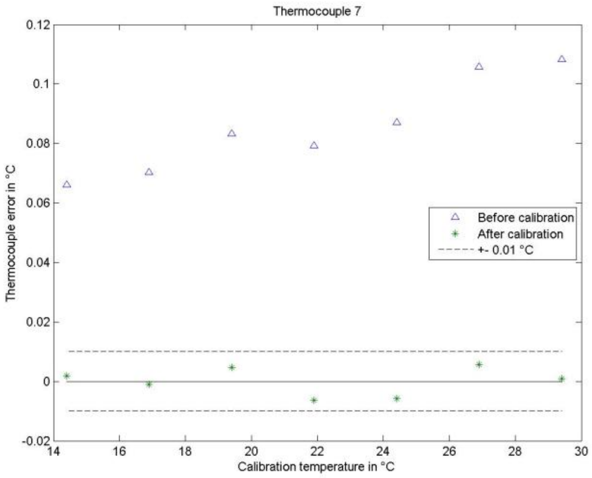
Thermocouple 7
0.12
0.1
0.08
0.06
0.04
0.02
0
-0.02
Thermocouple error in °C
14
16
18
20
22
24
26
28
30
Calibration temperature in °C
Before calibration
After calibration
+- 0.01 °C

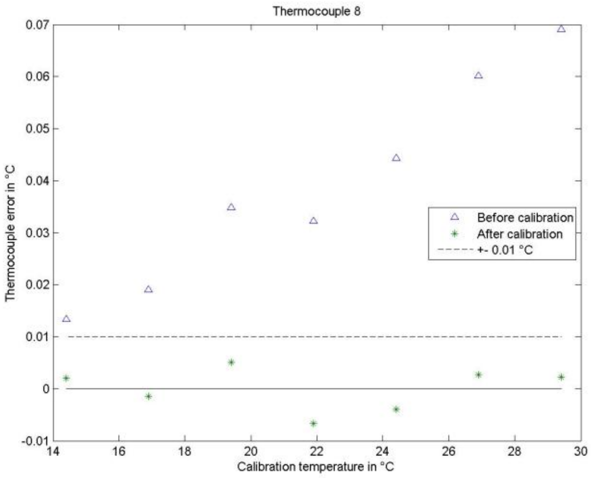
Thermocouple 8
0.07
0.06
0.05
0.04
0.03
0.02
0.01
0
-0.01
Thermocouple error in °C
14
16
18
20
22
24
26
28
30
Calibration temperature in °C
Before calibration
After calibration
+- 0.01 °C

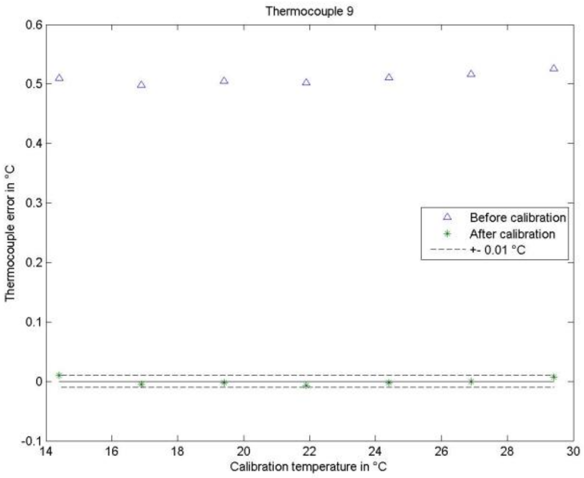
Thermocouple 9
0.6
0.5
0.4
0.3
0.2
0.1
0
-0.1
Thermocouple error in °C
14
16
18
20
22
24
26
28
30
Calibration temperature in °C
Before calibration
After calibration
+- 0.01 °C

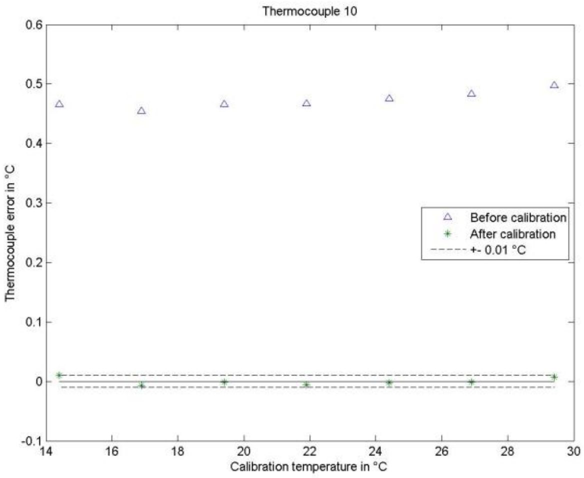
Thermocouple 10
0.6
0.5
0.4
0.3
0.2
0.1
0
-0.1
Thermocouple error in °C
14
16
18
20
22
24
26
28
30
Calibration temperature in °C
Before calibration
After calibration
+- 0.01 °C

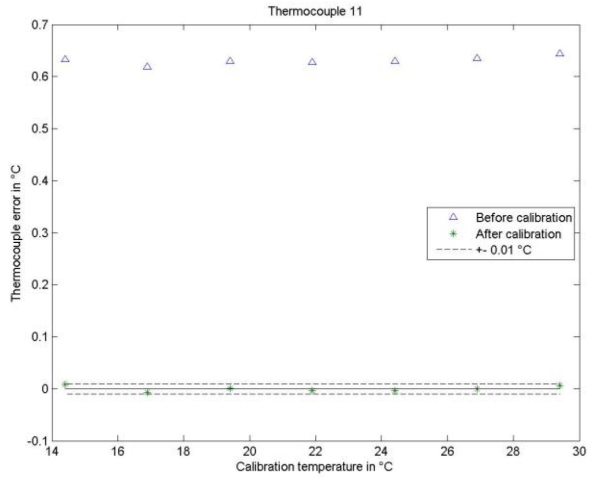
Thermocouple 11

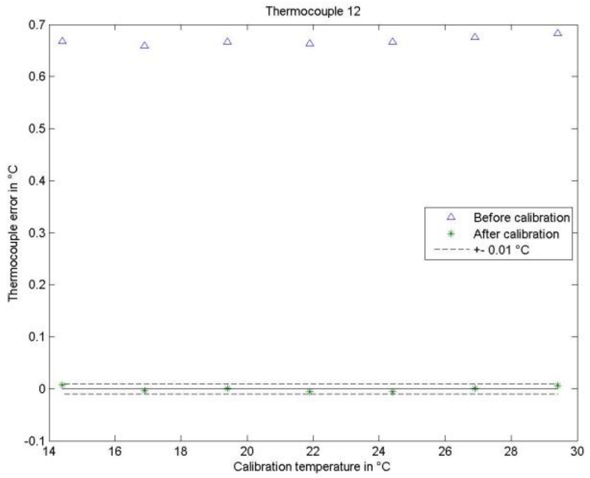
Thermocouple 12

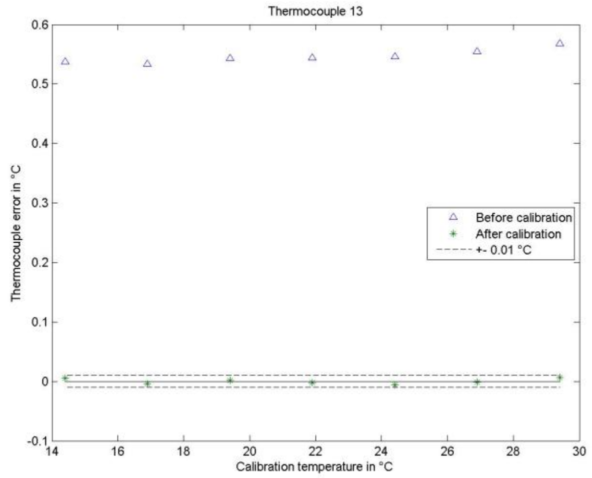
Thermocouple 13

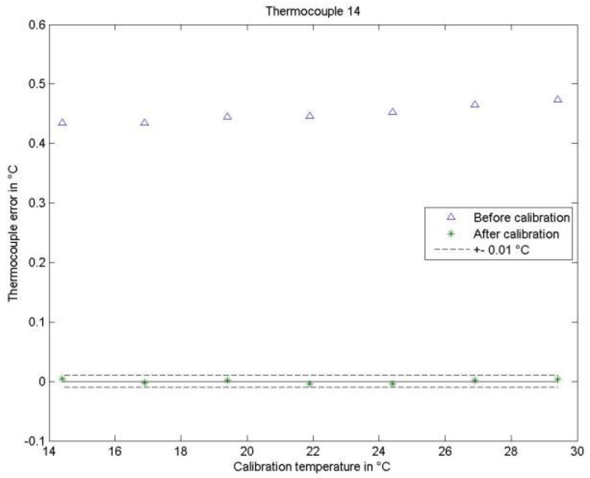
Thermocouple 14

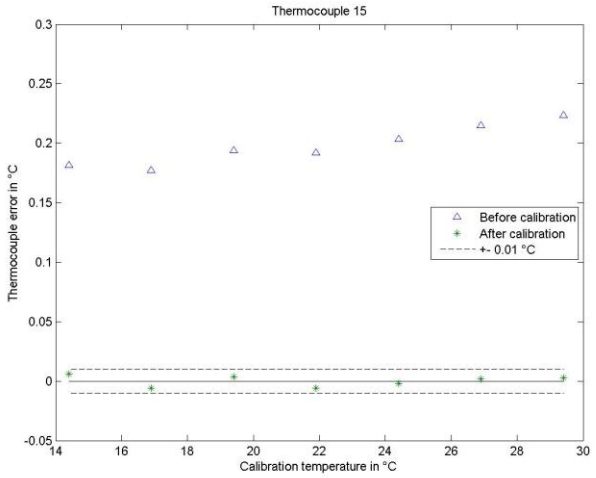
Thermocouple 15

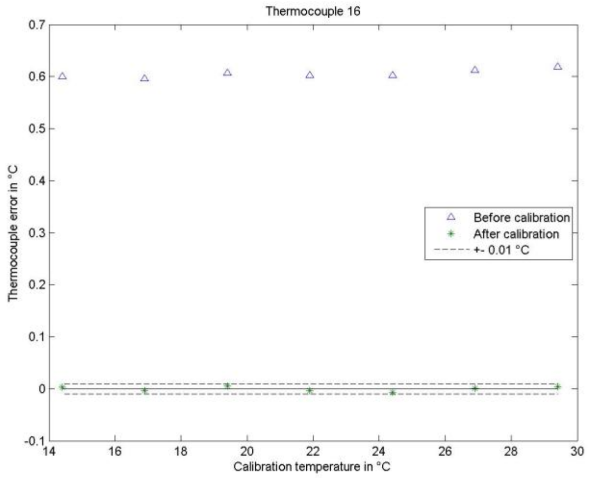
Thermocouple 16

Appendix C. Uncertainty analysis

This appendix covers all aspects regarding uncertainties calculated in this study by the method of Moffat (1988).

Uncertainty theory

Uncertainty refers to errors that a measurement may have. The measurement error is the difference between the true value and the measured value. A variable X_i is best approximated by $X_i\ (measured)$, which will have an associated uncertainty of $\pm\delta X_i$ for a single sample experiment. This is expressed mathematically as follows:

$$X_i = X_i\ (measured) \pm \delta X_i$$

The uncertainty of X_i is chosen so that that the odds are 20 to 1 that the error is smaller than δX_i. In a multi-variable experiment, the result R is computed by a number of independent variables, $X_1, X_2, X_3 \dots X_N$, which takes the following mathematical form:

$$R = f(X_1, X_2, X_3 \dots X_N)$$

The objective of an uncertainty analysis is to express the uncertainty of the result, δR, with the same odds that were assigned to the uncertainty of the independent variables $\delta X_1, \delta X_2, \delta X_3 \dots \delta X_N$. The influence that the uncertainty has on a single sample experiment may be expressed in the following partial derivative form:

$$\delta R_{X_i} = \frac{\partial R}{\partial_{X_i}} \delta_{X_i}$$

For a multiple sample experiment with independent variables $(X_1, X_2, X_3 \dots X_N)$ and result R, the uncertainties may be combined using the root-sum square combination.

$$\delta R = \left\{ \sum_{i=0}^{n} \left(\frac{\partial R}{\partial X_i} \delta X_i \right)^2 \right\}^{0.5}$$

Sample calculation

This section contains a sample calculation to calculate all uncertainties for the case D_3 = 20 mm, Re = 2 000 and x = 5 mm. Constant values for this test case are given in the table below.

Property	Value
D_2	0.042 m
D_1	0.027 m
D_h	0.015 m
L	0.95 m
x	0.015 m
T_{bin}	20.95 ˚C
A	0.084823 m^2
I	132.2 V
V	3.02 A
$\dot{m}$	0.1086 kg/s
$n_{thermocouple}$	8
n_{pixel}	113 400
k	0.60328 W/mK
$R_{adh}(2\ layers)$	0.00988712 ˚C/W

$$Nu = \frac{hD_h}{k}$$

$$\delta Nu = \left\{\left(\frac{\partial Nu}{\partial h}\delta h\right)^2 + \left(\frac{\partial Nu}{\partial D_h}\delta D_h\right)^2 + \left(\frac{\partial Nu}{\partial k}\delta k\right)^2\right\}^{0.5}$$

$$\delta Nu = \left\{\left(\frac{D_h}{k}\delta h\right)^2 + \left(\frac{h}{k}\delta D_h\right)^2 + \left(\frac{-hD_h}{k^2}\delta k\right)^2\right\}^{0.5}$$

$$\delta Nu = \ 10.4756$$

Uncertainty of D_h

$$D_h = D_2 - D_1$$

$$\delta D_h = \left\{\left(\frac{\partial D_h}{\partial D_2}\delta D_2\right)^2 + \left(\frac{\partial D_h}{\partial D_1}\delta D_1\right)^2\right\}^{0.5}$$

$$\delta D_h = \{(\delta D_2)^2 + (-\delta D_1)^2\}^{0.5}$$

$$\delta D_h = 0.00028284\ m$$

Uncertainty of *h*

$$h = \frac{\dot{q}}{T_w - T_b}$$

$$\delta h = \left\{\left(\frac{\partial h}{\partial \dot{q}}\delta \dot{q}\right)^2 + \left(\frac{\partial h}{\partial T_w}\delta T_w\right)^2 + \left(\frac{\partial h}{\partial T_b}\delta T_b\right)^2\right\}^{0.5}$$

$$\delta h = \left\{\left(\frac{1}{T_w - T_b}\delta \dot{q}\right)^2 + \left(-\frac{\dot{q}}{(T_w - T_b)^2}\delta T_w\right)^2 + \left(-\frac{\dot{q}}{(T_w - T_b)^2}\delta T_b\right)^2\right\}^{0.5}$$

$$\delta h = 416.31\ W/m^2℃$$

Uncertainty of $\dot{q}$

$$\dot{q} = \frac{Q}{A}$$

$$A = \pi D_1 L$$

$$\delta A = \left\{\left(\frac{\partial A}{\partial \pi}\delta \pi\right)^2 + \left(\frac{\partial A}{\partial D_1}\delta D_1\right)^2 + \left(\frac{\partial A}{\partial L}\delta L\right)^2\right\}^{0.5}$$

$$\delta A = \{(\pi L \delta D_1)^2 + (\pi D_1 \delta L)^2\}^{0.5}$$

$$\delta A = 0.0006341\ m^2$$

$$\dot{Q} = IV$$

$$\delta \dot{Q} = \left\{\left(\frac{\partial \dot{Q}}{\partial I}\delta I\right)^2 + \left(\frac{\partial \dot{Q}}{\partial V}\delta V\right)^2\right\}^{0.5}$$

$$\delta \dot{Q} = \{(V\delta I)^2 + (I\delta V)^2\}^{0.5}$$

$$\delta \dot{Q} = \{(V\delta I)^2 + (I\delta V)^2\}^{0.5}$$

$$\delta \dot{Q} = 1.129\ W$$

$$\dot{q} = \frac{\dot{Q}}{A}$$

$$\delta \dot{q} = \left\{\left(\frac{\partial \dot{q}}{\partial Q}\delta Q\right)^2 + \left(\frac{\partial \dot{q}}{\partial A}\delta A\right)^2\right\}^{0.5}$$

$$\delta \dot{q} = \left\{ \left(\frac{1}{A} \delta Q \right)^2 + \left(- \frac{\dot{Q}}{A^2} \delta A \right)^2 \right\}^{0.5}$$

$$\delta \dot{q} = 37.09856\ W/m^2$$

Uncertainty of T_w

$$T_w = T_{TLC} - \Delta T_{Dcfix}$$

$$\delta T_{TLC} = \sqrt{\frac{1}{n}} T_{TLC\ pixel}$$

$$\delta T_{TLC} = 0.00148478℃$$

$$\Delta T_{adh} = \dot{Q} R_{adh}$$

$$\delta \Delta T_{adh} = \left\{ \left(\frac{\partial \Delta T_{adh}}{\partial \dot{Q}} \delta \dot{Q} \right)^2 + \left(\frac{\partial \Delta T_{adh}}{\partial R_{adh}} \delta R_{adh} \right)^2 \right\}^{0.5}$$

$$\delta \Delta T_{adh} = \left\{ \left(R_{adh} \delta \dot{Q} \right)^2 + \left(\dot{Q} \delta R_{adh} \right)^2 \right\}^{0.5}$$

δR_{adh} was determined by calculating the precision interval of the true mean, as described by Dunn (2014). In this case, the precision interval may be seen as the uncertainty.

$$\delta R_{adh} = t_{v,P} S_{\bar{x}}$$

The term $t_{v,P}$ refers to a two-sided T-type distribution, where, in this case, $v = N - 1 = 94$ and $p = 90\%$ were chosen. The value of $t_{94,90\%}$ yielded 1.6645. A computer calculated the value of $S_{\bar{x}}$ to be 2.617E-4.

$$\delta R_{adh} = t_{v,P} S_{\bar{x}}$$

$$\delta R_{adh} = 0.0004357℃/W$$

For two layers,

$$\delta R_{adh} = 0.00087143℃/W$$

$$\delta\Delta T_{adh} = \left\{\left(R_{adh}\delta\dot{Q}\right)^2 + \left(\dot{Q}\delta R_{adh}\right)^2\right\}^{0.5}$$

$$\delta\Delta T_{adh} = 0.3481℃$$

Now,

$$T_w = T_{TLC} - \Delta T_{Dcfix}$$

$$\delta T_w = \left\{\left(\frac{\partial T_w}{\partial T_{TLC}}\delta T_{TLC}\right)^2 + \left(\frac{\partial T_w}{\partial \Delta T_{adh}}\delta\Delta T_{adh}\right)^2\right\}^{0.5}$$

$$\delta T_w = \{(\delta T_{TLC})^2 + (-\delta\Delta T_{adh})^2\}^{0.5}$$

$$\delta T_w = 0.348095℃$$

Uncertainty of T_b

$$T_{bx} = T_{bin} + \frac{\dot{Q}}{\dot{m}Cp}\left(\frac{x}{L}\right)$$

$$\delta T_{bin} = \sqrt{\frac{1}{n}}\delta T_{thermocouple}$$

$$\delta T_{bin} = 0.03889℃$$

$$\delta T_{bx} = \left\{\left(\frac{\partial T_{bx}}{\partial T_{bin}}\delta T_{bin}\right)^2 + \left(\frac{\partial T_{bx}}{\partial \dot{Q}}\delta\dot{Q}\right)^2 + \left(\frac{\partial T_{bx}}{\partial \dot{m}}\delta\dot{m}\right)^2 + \left(\frac{\partial T_{bx}}{\partial Cp}\delta Cp\right)^2 + \left(\frac{\partial T_{bx}}{\partial x}\delta x\right)^2 + \left(\frac{\partial T_{bx}}{\partial L}\delta L\right)^2\right\}^{0.5}$$

$$\delta T_{bx} = \left\{(\delta T_{bin})^2 + \left(\frac{x}{\dot{m}CpL}\delta\dot{Q}\right)^2 + \left(\frac{-\dot{Q}x}{\dot{m}^2CpL}\delta\dot{m}\right)^2 + \left(\frac{-\dot{Q}x}{\dot{m}Cp^2L}\delta Cp\right)^2 + \left(\frac{\dot{Q}}{\dot{m}CpL}\delta x\right)^2 + \left(\frac{-\dot{Q}x}{\dot{m}CpL^2}\delta L\right)^2\right\}^{0.5}$$

$$\delta T_{bx} = 0.038891℃$$

Uncertainty of *k*

$$\delta k = 0.01206\ W/mK$$

Calculating U

$$U = \left(\frac{\sum_{i=1}^{12} h_i}{2} + \sum_{i=13}^{27} h_i\right)/27$$

Knowing that $h_i = \frac{\dot{q}}{T_w - T_B} = \frac{\dot{q}}{T_{TLC} - T_{adh} - T_B}$, the statement above may be rewritten as follows:

$$U = \left(\frac{\sum_{i=1}^{12} \frac{\dot{q}}{T_{TLC_i} - T_{adh} - T_{B_i}}}{2} + \sum_{i=13}^{27} \frac{\dot{q}}{T_{TLC_i} - T_{adh} - T_{B_i}}\right)/27$$

Simplifying this equation to $\Delta T = T_{TLC} - T_B, \Delta T' = \Delta T - \Delta T_{adh}$,

$$U = \left(\frac{\sum_{i=1}^{12} \frac{\dot{q}}{\Delta T_i'}}{2} + \sum_{i=13}^{27} \frac{\dot{q}}{\Delta T_i'}\right)/27$$

$$\Delta T = T_{TLC} - T_B$$

$$\delta\Delta T = \left\{\left(\frac{\partial \Delta T}{\partial T_{TLC}}\delta T_{TLC}\right)^2 + \left(\frac{\partial \Delta T}{\partial T_B}\delta T_B\right)^2\right\}^{0.5}$$

$$\delta\Delta T = \{(\delta T_{TLC})^2 + (-\delta T_B)^2\}^{0.5}$$

$$\delta\Delta T = 0.03892℃$$

$$\Delta T' = \Delta T - \Delta T_{adh}$$

$$\delta\Delta T = \left\{\left(\frac{\partial \Delta T'}{\partial \Delta T}\delta \Delta T\right)^2 + \left(\frac{\partial \Delta T}{\partial \Delta T_{adh}}\delta \Delta T_{adh}\right)^2\right\}^{0.5}$$

$$\delta\Delta T = \{(\delta\Delta T)^2 + (-\delta\Delta T_{adh})^2\}^{0.5}$$

$$\delta\Delta T = 0.35026℃$$

$$\delta U = \frac{\left(\frac{\sum_{i=1}^{12}\left\{\left(\frac{\partial U}{\partial \dot{q}}\delta\dot{q}\right)^2 + \left(\frac{\partial U}{\partial \Delta T_i'}\delta\Delta T_i'\right)^2\right\}^{0.5}}{2} + \sum_{i=13}^{27}\left\{\left(\frac{\partial U}{\partial \dot{q}}\delta\dot{q}\right)^2 + \left(\frac{\partial U}{\partial \Delta T_i'}\delta\Delta T_i'\right)^2\right\}^{0.5}\right)}{27}$$

$$\delta U = 75.725\ W/m^2℃$$

Appendix D. Determining the thermal resistance of the protective adhesive layer

A protective layer had to be placed over the TLC coating to protect the crystals from being washed away by the water in the annulus, as they were soluble in water. A protective adhesive layer manufactured from transparent PVC was applied over the TLCs. For the experiments, two layers of this protective coating were applied over the TLCs to ensure that no water could seep into the TLCs.

The temperature readings from the TLCs would not indicate the wall temperature anymore, but rather a temperature higher than the wall temperature. The TLC temperature would be the wall temperature plus a temperature difference that was present over the protective layer, as shown in the equation below. In this equation, T_w refers to the wall temperature, which had to be known, T_{TLC} refers to the temperature, which the TLCs were reading, and ΔT_{adh} refers to the temperature difference over the protective adhesive layer.

$$T_w = T_{TLC} - \Delta T_{adh}$$

This temperature difference ΔT_{adh} could only be determined for a given heat rate $\dot{Q}$ once the thermal resistance of the layer was known. This can be equated mathematically as:

$$\Delta T_{adh} = \dot{Q} R_{adh}$$

The value of R_{adh} was calculated in two different ways to ensure that an accurate value was found. A mathematical approximation was set up in addition to an experimental investigation. Both procedures are discussed below.

Mathematical approximation

The thermal resistance by conduction of a cylinder may be expressed in the form shown below, where r_2 and r_1 refer to the inner and outer radii of the cylinder, L refers to the length of the cylinder and k refers to the thermal conductivity of the material of the cylinder.

$$R_{cyl} = \frac{\ln\left(\frac{r_2}{r_1}\right)}{2\pi L k}$$

The values of r_2 and r_1 were found to be 0.0136 m and 0.01344 m respectively. Please note that these were the inner and outer radii of two protective layers. These were measured by a micrometer with a measuring accuracy of 0.01 mm. For the value of k, it was assumed that the adhesive layer was manufactured from pure PVC with a thermal conductivity of 0.19 W/mK.

This approach yields a value for R_{adh} of 0.004996˚C/W. Please note that this mathematical approach neglects the thermal resistance imposed by the contact region between the TLC and the two layers.

Experimental investigation

For the experimental investigation, the heat exchanger and photography mechanism built for the investigation would be used. The value of R_{adh} would be approximated by evaluating the influence that an additional protective layer has on the temperature readings of the TLCs.

The equation derived below can be used to calculate R_{adh}. Two equations are set up from the equation stated in Equation 42. The equation with the subscripts $1-2$ refers to the case in which two adhesive layers were used, and $1-3$ refers to the case in which the additional adhesive layer was added, which formed a total of three layers.

$$\Delta T_{1-2} = \dot{Q} R_{eq_{1-2}}$$

$$\Delta T_{1-3} = \dot{Q} R_{eq_{1-3}}$$

The temperature difference ΔT refers to the temperature difference between the TLCs and the bulk fluid temperature at the specific location. The resistance R refers to the thermal resistance, which is composed of the conductive thermal resistance by the adhesive layer and convective thermal resistance between the adhesive layer and the bulk fluid. Rewriting these equations yields the following:

$$\Delta T_{1-2} = \dot{Q} R_{eq_{1-2}} = \dot{Q}(R_{1-2} + R_{conv})$$

$$\Delta T_{1-3} = \dot{Q} R_{eq_{1-3}} = \dot{Q}(R_{1-3} + R_{conv}) = \dot{Q}(R_{1-2} + R_{2-3} + R_{conv})$$

For the experiments, the value $\dot{Q}$ was kept the same for both experiments. It was assumed that the value of R_{conv} remains constant for the case of two and three protective layers, as there is only a minor change in diameters, which results in a diameter ratio change of 0.43%. Subtracting these two equations from one another yields the following:

$$\Delta T_{1-3} - \Delta T_{1-2} = \dot{Q} R_{2-3}$$

The derived equation states the following: The temperature difference between the TLC and the bulk fluid temperature for three and two protective adhesive layers is equal to the heat rate multiplied by the thermal resistance of the third layer. The thermal resistance of a single protective adhesive layer may thus be calculated by the formula below.

$$\frac{\Delta T_{1-3} - \Delta T_{1-2}}{\dot{Q}} = R_{2-3}$$

The temperature readings of the TLCs were recorded for flow rates of the Reynolds numbers 2 000, 3 000, 4 000, 5 000 and 6 000 while keeping the heat rate constant at 320 W. The temperature of the TLCs was subtracted from the bulk fluid temperatures that were calculated with Equation 43. Figure D-1 shows the TLC temperatures for two and three protective layers minus the bulk fluid temperature. The value of $T_3 - T_2$ can be determined by subtracting these two temperatures. The value of $T_3 - T_2$ is only considered from 150 mm onwards, as it varies at the inlet region due to boundary layer development. As seen from Figure D-1, the value of $T_3 - T_2$ is relatively stable.

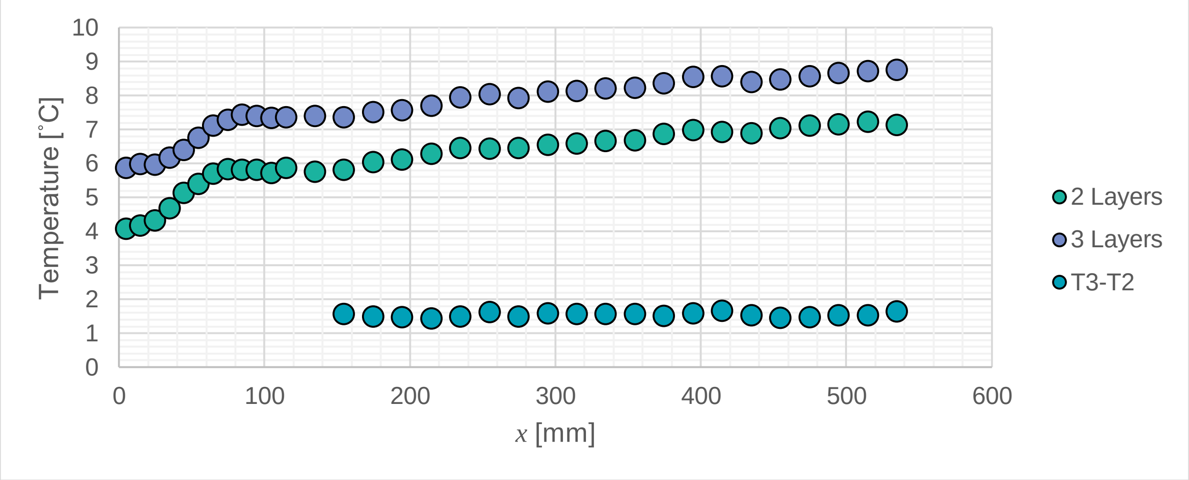

Figure D-1: Temperature variations along the length of the heating rod for Re = 3 000

The average value of $T_3 - T_2$ was calculated for all flow rate states and was found to be 1.6645 ˚C. Substituting this value into the above equation yields a value of $R_{adh} = 0.004944℃/W$.

The approximations by the mathematical model experimental investigation yielded similar estimations for the value of R_{adh}. The mathematical approximation estimated the value to be 0.004996 ˚C/W and the experimental investigation 0.004944 ˚C/W. This equates to a difference in answers of 1.051% with reference to the experimental value.

Appendix E. Local heat transfer coefficients

The local heat transfer coefficients for the different test cases can be found in the tables below.

Table E-1: Local heat transfer coefficient (W/m^{2}K) for test case A

		Reynolds number										
		2 041	2 561	3 079	3 604	4 122	5 129	5 640	6 167	6 681	7 200	7 728
x (mm)	5	2 355	2 696	2 720	3 147	3 319	3 761	3 885	3 699	3 862	3 991	3 994
	15	2 256	2 544	2 628	2 932	3 089	3 376	3 397	3 365	3 403	3 546	3 603
	25	2 050	2 396	2 245	2 719	2 868	3 078	3 164	3 161	3 273	3 373	3 411
	35	1 755	2 059	1 922	2 359	2 449	2 674	2 749	2 830	2 903	3 002	3 034
	45	1 516	1 768	1 706	2 053	2 132	2 264	2 386	2 446	2 529	2 612	2 660
	55	1 346	1 564	1 536	1 799	1 873	2 009	2 089	2 175	2 255	2 317	2 387
	65	1 190	1 356	1 386	1 540	1 651	1 782	1 863	1 939	2 007	2 071	2 115
	75	1 112	1 266	1 313	1 472	1 584	1 748	1 820	1 893	1 964	2 031	2 069
	85	1 078	1 231	1 320	1 423	1 548	1 723	1 784	1 839	1 913	1 994	2 028
	95	1 061	1 204	1 353	1 445	1 560	1 773	1 811	1 887	1 952	2 030	2 076
	105	1 052	1 216	1 374	1 480	1 609	1 797	1 870	1 936	2 019	2 117	2 165
	115	1 056	1 239	1 348	1 488	1 613	1 829	1 879	1 986	2 032	2 140	2 193
	135	988	1 161	1 294	1 457	1 539	1 748	1 788	1 867	1 957	2 067	2 065
	155	988	1 153	1 306	1 418	1 548	1 751	1 819	1 893	1 972	2 050	2 104
	175	945	1 122	1 223	1 335	1 451	1 667	1 696	1 784	1 846	1 917	1 957
	195	897	1 065	1 190	1 316	1 425	1 624	1 687	1 757	1 825	1 891	1 962
	215	876	1 051	1 152	1 256	1 359	1 565	1 630	1 690	1 753	1 837	1 875
	235	830	1 002	1 097	1 198	1 301	1 509	1 561	1 627	1 679	1 756	1 811
	255	790	954	1 061	1 175	1 276	1 481	1 554	1 605	1 661	1 742	1 779
	275	806	952	1 101	1 224	1 317	1 546	1 616	1 693	1 773	1 830	1 888
	295	790	964	1 083	1 197	1 298	1 520	1 591	1 674	1 744	1 804	1 850
	315	769	934	1 063	1 183	1 287	1 491	1 594	1 663	1 735	1 818	1 885
	335	760	912	1 040	1 160	1 260	1 479	1 558	1 633	1 730	1 769	1 829
	355	739	886	1 018	1 144	1 253	1 464	1 544	1 631	1 684	1 792	1 836
	375	717	871	1 009	1 118	1 223	1 442	1 524	1 611	1 669	1 739	1 804
	395	689	840	958	1 076	1 170	1 361	1 441	1 515	1 587	1 651	1 717
	415	666	807	938	1 053	1 162	1 354	1 425	1 503	1 569	1 649	1 707
	435	662	807	958	1 083	1 185	1 396	1 463	1 552	1 629	1 698	1 742
	455	659	808	941	1 053	1 164	1 367	1 435	1 510	1 580	1 657	1 703
	475	633	786	917	1 031	1 140	1 324	1 418	1 478	1 553	1 620	1 673
	495	622	770	898	1 005	1 113	1 297	1 384	1 452	1 527	1 598	1 649
	515	599	759	883	1 002	1105	1 291	1 371	1 446	1 508	1 588	1 645
	535	595	746	881	996	1 100	1 286	1 355	1 432	1 511	1 585	1 640

Table E-2: Local heat transfer coefficient (W/m^{2}K) for test case se B

		Reynolds number										
		2 033	2 543	3 053	3 534	4 042	4 575	5 057	5 594	6 103	7 117	7 624
x [mm]	5	2 417	2 575	2 862	3 155	3 325	3 357	2 852	3 649	3 822	3 833	4 031
	15	2 260	2 439	2 641	2 788	2 863	3 095	2 630	3 270	3 381	3 475	3 566
	25	2 011	2 154	2 401	2 640	2 780	2 776	2 445	2 954	3 065	3 166	3 250
	35	1 768	1 887	2 039	2 338	2 473	2 377	2 168	2 584	2 634	2 776	2 853
	45	1 564	1 657	1 822	2 085	2 209	2 129	1 976	2 269	2 379	2 469	2 517
	55	1 385	1 493	1 636	1 822	1 944	1 910	1 789	2 046	2 146	2 228	2 286
	65	1 251	1 354	1 478	1 598	1 718	1 794	1 662	1 900	1 962	2 086	2 140
	75	1 199	1 302	1 441	1 460	1 557	1 742	1 659	1 861	1 924	2 035	2 105
	85	1 158	1 278	1 424	1 415	1 485	1 739	1 645	1 872	1 926	2 032	2 087
	95	1 162	1 282	1 452	1 410	1 508	1 774	1 665	2 014	1 973	2 126	2 149
	105	1 182	1 314	1 498	1 459	1 554	1 815	1 733	2 029	2 033	2 154	2 211
	115	1 148	1 273	1 443	1 523	1 628	1 787	1 699	1 931	2 011	2 130	2 210
	135	1 111	1 248	1 441	1 444	1 573	1 752	1 656	1 891	1 964	2 101	2 172
	155	1 085	1 222	1 379	1 511	1 625	1 742	1 656	1 900	1 971	2 107	2 180
	175	1 017	1 160	1 303	1 434	1 562	1 631	1 566	1 780	1 851	1 977	2 047
	195	1 013	1 152	1 305	1 403	1 539	1 650	1 576	1 791	1 858	1 975	2 045
	215	960	1 090	1 223	1 334	1 453	1 542	1 486	1 688	1 784	1 876	1 934
	235	905	1 029	1 181	1 268	1 369	1 461	1 395	1 584	1 650	1 771	1 819
	255	887	1 034	1 124	1 237	1 347	1 400	1 391	1 583	1 661	1 773	1 836
	275	897	1 048	1 167	1 292	1 399	1 495	1 449	1 670	1 735	1 866	1 927
	295	869	1 010	1 108	1 243	1 349	1 442	1 410	1 601	1 674	1 812	1 883
	315	844	992	1 112	1 224	1 340	1 437	1 411	1 607	1 689	1 837	1 900
	335	813	955	1 077	1 211	1 327	1 401	1 380	1 586	1 661	1 803	1 867
	355	796	949	1 086	1 212	1 326	1 395	1 380	1 580	1 671	1 789	1 864
	375	775	914	1 062	1 195	1 313	1 369	1 349	1 540	1 628	1 765	1 832
	395	740	876	1 008	1 128	1 247	1 301	1 291	1 471	1 554	1 686	1 749
	415	729	862	995	1 128	1 231	1 288	1 280	1 459	1 541	1 688	1 734
	435	703	879	1 026	1 159	1 293	1 330	1 315	1 503	1 580	1 785	1 802
	455	691	848	996	1 162	1 284	1 294	1 267	1 481	1 543	1 689	1 748
	475	678	836	976	1 135	1 248	1 283	1 250	1 444	1 517	1 685	1 708
	495	660	816	958	1 127	1 245	1 238	1 219	1 412	1 491	1 624	1 679
	515	663	811	939	1 093	1 225	1 217	1 204	1 394	1 446	1 602	1 663
	535	649	809	931	1 090	1 226	1 225	1 214	1 409	1 485	1 633	1 685

Table E-3: Local heat transfer coefficient (W/m^{2}K) for test case C

		Reynolds number								
		2 051	2 562	4 097	4 609	5 121	5 633	6 141	6 653	7 576
x [mm]	5	3 160	3 237	3 916	3 872	4 217	4 210	4 204	4 000	4 146
	15	2 644	2 755	3 117	3 189	3 216	3 285	3 406	3 155	3 369
	25	2 303	2 462	2 849	2 926	2 920	3 036	3 095	2 933	3 124
	35	2 030	2 187	2 577	2 627	2 697	2 767	2 804	2 766	2 943
	45	1 771	1 913	2 272	2 364	2 408	2 488	2 546	2 536	2 637
	55	1 563	1 711	2 036	2 135	2 159	2 238	2 325	2 312	2 421
	65	1 346	1 485	1 782	1 885	1 925	2 010	2 066	2 059	2 166
	75	1 260	1 382	1 674	1 774	1 830	1 907	1 965	1 978	2 073
	85	1 182	1 298	1 622	1 706	1 756	1 814	1 897	1 899	2 001
	95	1 118	1 263	1 587	1 688	1 738	1 805	1 868	1 893	1 992
	105	1 115	1 258	1 612	1 697	1 759	1 839	1 903	1 945	2 038
	115	1 115	1 269	1 667	1 759	1 822	1 899	1 993	2 009	2 120
	135	1 030	1 180	1 540	1 627	1 690	1 768	1 851	1 872	1 977
	155	1 018	1 188	1 583	1 655	1 722	1 809	1 899	1 914	2 025
	175	976	1 145	1 502	1 714	1 668	1 741	1 799	1 843	1 951
	195	930	1 096	1 429	1 530	1 593	1 670	1 748	1 763	1 859
	215	912	1 062	1 384	1 517	1 579	1 649	1 717	1 750	1 859
	235	858	1 014	1 305	1 412	1 506	1 586	1 627	1 669	1 775
	255	829	981	1 281	1 388	1 458	1 525	1 585	1 646	1 723
	275	842	1 012	1 326	1 465	1 519	1 603	1 665	1 696	1 821
	295	824	987	1 309	1 442	1 505	1 587	1 654	1 700	1 798
	315	804	969	1 272	1 438	1 485	1 555	1 642	1 679	1 786
	335	788	941	1 272	1 431	1 473	1 518	1 609	1 667	1 760
	355	775	926	1 268	1 420	1 458	1 542	1 627	1 665	1 691
	375	762	928	1 263	1 431	1 442	1 530	1 612	1 644	1 614
	395	727	875	1 216	1 366	1 372	1 448	1 515	1 580	1 588
	415	717	851	1 189	1 351	1 347	1 428	1 491	1 555	1 616
	435	724	854	1 205	1 406	1 377	1 462	1 525	1 587	1 522
	455	718	868	1 213	1 401	1 394	1 467	1 551	1 602	1 496
	475	684	834	1 175	1 346	1 330	1 410	1 478	1 555	1 541
	495	666	812	1 156	1 341	1 311	1 377	1 470	1 534	1 547
	515	656	809	1 142	1 328	1 292	1 367	1 446	1 510	1 493
	535	651	798	1 136	1 329	1 298	1 373	1 440	1 514	1 465

Table E-4: Local heat transfer coefficient (W/m^{2}K) for test case D

		Reynolds number										
		2 041	2 570	3 085	3 596	4 109	4 624	5 651	6 161	6 676	7 188	7 602
x [mm]	5	2 851	2 537	2 708	3 017	2 900	3 014	3 744	3 157	3 797	3 727	4 379
	15	2 319	2 194	2 246	2 588	2 432	2 512	3 003	2 645	3 119	3 011	3 033
	25	1 986	1 969	2 029	2 316	2 210	2 240	2 711	2 426	2 767	2 753	2 782
	35	1 753	1 738	1 808	2 101	1 960	2 046	2 470	2 246	2 567	2 534	2 592
	45	1 548	1 560	1 634	1 865	1 789	1 888	2 264	2 026	2 336	2 322	2 396
	55	1 394	1 437	1 518	1 721	1 662	1 732	2 041	1 876	2 130	2 178	2 221
	65	1 225	1 290	1 390	1 580	1 549	1 573	1 852	1770	1 992	1 977	2 013
	75	1 143	1 209	1 326	1 515	1 500	1 535	1 807	1 727	1 933	1 916	1 958
	85	1 086	1 151	1 265	1 476	1 458	1 530	1 776	1 694	1 899	1 890	1 922
	95	1 068	1 137	1262	1 459	1 442	1 558	1 787	1 693	1 904	1 894	1 947
	105	1 054	1 152	1 287	1 487	1 479	1 624	1 834	1 733	1 957	1 965	1 987
	115	1 064	1 198	1 329	1 559	1 538	1 486	1 913	1 812	2 056	2 064	2 095
	135	1 003	1 112	1 272	1 439	1 413	1 533	1 764	1 733	1 903	1 906	1 933
	155	1 002	1 118	1 247	1 463	1 437	1 461	1 799	1 718	1 945	1 966	1 989
	175	968	1 073	1 196	1 394	1 380	1 371	1 754	1 648	1 844	1 885	1 925
	195	903	1 020	1 137	1 311	1 296	1 330	1 633	1 564	1 757	1 769	1 820
	215	871	1 001	1 105	1 278	1 258	1 251	1 598	1 515	1 723	1 734	1 794
	235	818	944	1 044	1 206	1 189	1 207	1 501	1 424	1 604	1 655	1 678
	255	786	903	1 005	1 163	1 142	1 231	1 442	1 361	1 541	1 577	1 614
	275	803	922	1 025	1 187	1 164	1 214	1 488	1 416	1 602	1 646	1 675
	295	788	899	999	1 158	1 145	1 178	1 458	1 380	1 558	1 611	1 636
	315	762	866	979	1 122	1 109	1 154	1 409	1 359	1 522	1 555	1 589
	335	744	853	947	1 098	1 089	1 137	1 379	1 313	1 484	1 523	1 547
	355	726	847	937	1 080	1 062	1 116	1 345	1 272	1 459	1 493	1 541
	375	714	824	923	1 059	1 033	1 054	1 309	1 245	1 359	1 488	1 515
	395	677	779	869	999	986	1 026	1 232	1 181	1 317	1 396	1 426
	415	655	764	846	962	954	1 038	1 195	1 149	1 333	1 367	1 401
	435	664	773	846	970	959	1 046	1 210	1 164	1 351	1 394	1 446
	455	652	768	851	957	954	999	1 208	1 160	1 307	1 417	1 455
	475	618	730	813	909	906	976	1 164	1 128	1287	1 372	1 399
	495	598	724	795	896	888	950	1 148	1 118	1 269	1 333	1 380
	515	575	700	772	861	861	952	1 125	1 101	1 268	1 326	1 358
	535	556	691	755	851	854	954	1 114	1101	1 272	1 353	1 376

Table E-5: Local heat transfer coefficient (W/m^{2}K) for test case E

		Reynolds Number																		
		205	410	610	1 022	1 221	1 423	1 624	2 026	2 041	2 561	3 079	3 604	4 122	5 129	5 640	6 167	6 681	7 200	7 728
x [mm]	5	914	1 253	1 691	4 236	4 627	4 653	4 644	3 271	2 355	2 696	2 720	3 147	3 319	3 761	3 885	3 699	3 862	3 991	3 994
	15	894	1 212	1 602	3 700	4 112	4 082	4 281	3 063	2 256	2 544	2 628	2 932	3 089	3 376	3 397	3 365	3 403	3 546	3 603
	25	866	1 133	1 492	2 820	3 121	3 355	3 632	2 556	2 050	2 396	2 245	2 719	2 868	3 078	3 164	3 161	3 273	3 373	3 411
	35	816	1 070	1 373	2 232	2 426	2 620	2 794	2 094	1 755	2 059	1 922	2 359	2 449	2 674	2 749	2 830	2 903	3 002	3 034
	45	745	977	1 252	1 762	1 930	2 107	2 312	1 663	1 516	1 768	1 706	2 053	2 132	2 264	2 386	2 446	2 529	2 612	2 660
	55	674	922	1 140	1 459	1 626	1 785	1 956	1 478	1 346	1 564	1 536	1 799	1 873	2 009	2 089	2 175	2 255	2 317	2 387
	65	608	854	1 043	1 256	1 380	1 526	1 635	1 292	1 190	1 356	1 386	1 540	1 651	1 782	1 863	1 939	2 007	2 071	2 115
	75	581	818	974	1 104	1 286	1 431	1 569	1 226	1 112	1 266	1 313	1 472	1 584	1 748	1 820	1 893	1 964	2 031	2 069
	85	557	780	928	1 056	1 237	1 407	1 488	1 194	1 078	1 231	1 320	1 423	1 548	1 723	1 784	1 839	1 913	1 994	2 028
	95	534	742	878	991	1 177	1 390	1 496	1 211	1 061	1 204	1 353	1 445	1 560	1 773	1 811	1 887	1 952	2 030	2 076
	105	537	729	862	996	1 150	1 408	1 542	1 223	1 052	1 216	1 374	1 480	1 609	1 797	1 870	1 936	2 019	2 117	2 165
	115	524	663	786	888	1 046	1 273	1 439	1 146	1 056	1 239	1 348	1 488	1 613	1 829	1 879	1 986	2 032	2 140	2 193
	135	545	651	767	843	1 009	1 201	1 579	1 158	988	1 161	1 294	1 457	1 539	1 748	1 788	1 867	1 957	2 067	2 065
	155	511	626	752	799	949	1 211	1 344	1 127	988	1 153	1 306	1 418	1 548	1 751	1 819	1 893	1 972	2 050	2 104
	175	473	579	678	725	836	990	1 198	1 067	945	1 122	1 223	1 335	1 451	1 667	1 696	1 784	1 846	1 917	1 957
	195	463	565	650	696	802	977	1 131	1 047	897	1 065	1 190	1 316	1 425	1 624	1 687	1 757	1 825	1 891	1 962
	215	451	547	621	652	746	891	1 069	985	876	1 051	1 152	1 256	1 359	1 565	1 630	1 690	1 753	1 837	1 875
	235	432	521	564	625	708	821	977	945	830	1 002	1 097	1 198	1 301	1 509	1 561	1 627	1 679	1 756	1 811
	255	436	517	565	612	689	789	965	952	790	954	1 061	1 175	1 276	1 481	1 554	1 605	1 661	1 742	1 779
	275	441	508	544	593	683	777	937	947	806	952	1 101	1 224	1 317	1 546	1 616	1 693	1 773	1 830	1 888
	295	438	505	520	577	657	724	893	920	790	964	1 083	1 197	1 298	1 520	1 591	1 674	1 744	1 804	1 850
	315	444	491	511	560	638	713	865	909	769	934	1 063	1 183	1 287	1 491	1 594	1 663	1 735	1 818	1 885
	335	431	473	478	542	609	680	808	880	760	912	1 040	1 160	1 260	1 479	1 558	1 633	1 730	1 769	1 829
	355	433	467	472	528	601	671	768	881	739	886	1 018	1 144	1 253	1 464	1 544	1 631	1 684	1 792	1 836
	375	429	459	456	511	568	638	726	829	717	871	1 009	1 118	1 223	1 442	1 524	1 611	1 669	1 739	1 804
	395	431	454	447	499	551	613	700	795	689	840	9 58	1 076	1 170	1 361	1 441	1 515	1 587	1 651	1 717
	415	439	468	449	497	545	605	698	797	666	807	938	1 053	1 162	1 354	1 425	1 503	1 569	1 649	1 707
	435	454	475	454	498	539	605	697	804	662	807	958	1 083	1 185	1 396	1 463	1 552	1 629	1 698	1 742
	455	465	480	454	482	529	588	677	775	659	808	941	1 053	1 164	1 367	1 435	1 510	1 580	1 657	1 703
	475	456	480	445	469	517	574	667	754	633	786	917	1 031	1 140	1 324	1 418	1 478	1 553	1 620	1 673
	495	457	481	445	464	510	559	640	733	622	770	898	1 005	1 113	1 297	1 384	1 452	1 527	1 598	1 649
	515	461	484	444	459	503	548	633	726	599	759	883	1 002	1 105	1 291	1 371	1 446	1 508	1 588	1 645
	535	493	521	466	465	508	551	645	735	595	746	881	996	1 100	1 286	1 355	1 432	1 511	1 585	1 640